USCIPI Report 930

CHARACTERIZATION OF LIQUID CRYSTAL LIGHT VALVES AND THEIR APPLICATIONS TO REAL-TIME NONLINEAR OPTICAL PROCESSING

by

Jerry Dean Michaelson

October 1979

Department of Electrical Engineering
Image Processing Institute
University of Southern California
Los Angeles, California 90007

Research sponsored by the
Air Force Office of Scientific Research
Electronics and Solid State Sciences Division
under Grant No. AFOSR-77-3285

UNCLASSIFIED

SECURITY CLASSIFICATION OF THIS PAGE *(When Data Entered)*

REPORT DOCUMENTATION PAGE		READ INSTRUCTIONS BEFORE COMPLETING FORM
1. REPORT NUMBER USCIPI Report 930	2. GOVT ACCESSION NO.	3. RECIPIENT'S CATALOG NUMBER
4. TITLE *(and Subtitle)* CHARACTERIZATION OF LIQUID CRYSTAL LIGHT VALVES AND THEIR APPLICATION TO REAL-TIME NONLINEAR OPTICAL PROCESSING		5. TYPE OF REPORT & PERIOD COVERED Technical Report October 1979 6. PERFORMING ORG. REPORT NUMBER USCIPI Report 930
7. AUTHOR(s) Jerry Dean Michaelson		8. CONTRACT OR GRANT NUMBER(s) AFOSR-77-3285
9. PERFORMING ORGANIZATION NAME AND ADDRESS Department of Electrical Engineering Image Processing Inst., Univ. of So. Cal. University Park, L.A., Calif. 90007		10. PROGRAM ELEMENT, PROJECT, TASK AREA & WORK UNIT NUMBERS
11. CONTROLLING OFFICE NAME AND ADDRESS Air Force Office of Scientific Research Bldg. 410, Bolling AFB Washington, D.C. 20332		12. REPORT DATE October 1979 13. NUMBER OF PAGES 158
14. MONITORING AGENCY NAME & ADDRESS *(if different from Controlling Office)* AS ABOVE		15. SECURITY CLASS. *(of this report)* UNCLASSIFIED 15a. DECLASSIFICATION/DOWNGRADING SCHEDULE

16. DISTRIBUTION STATEMENT *(of this Report)*

Approved for release: distribution unlimited

The United States Government is authorized to reproduce and distribute reprints for Governmental purposes notwithstanding any copyright notation hereon.

17. DISTRIBUTION STATEMENT *(of the abstract entered in Block 20, if different from Report)*

18. SUPPLEMENTARY NOTES

19. KEY WORDS *(Continue on reverse side if necessary and identify by block number)*

Optical information processing, nonlinear optical processing, real-time optical processing, liquid crystal devices, liquid crystal light valves, real-time optical transducers.

20. ABSTRACT *(Continue on reverse side if necessary and identify by block number)*

The use of optical processors to perform linear operations such as Fourier transforming, convolution, and correlation on large bandwidth signals and images has been of great interest and has been investigated for some time. Extension of the processing capability to include nonlinear operations has been the subject of more recent interest and investigation. In this dissertation a method is presented to realize real-time nonlinear operations on

DD FORM 1 JAN 73 1473

UNCLASSIFIED

SECURITY CLASSIFICATION OF THIS PAGE *(When Data Entered)*

two dimensional images through the use of multiple liquid crystal light valves.

A review is given of the theory associated with the light valves. Consideration is given both to electrically controlled cells and photoactivated devices. Special characteristics of the light valves pertinent to the nonlinear processing system are considered in detail. Actual light valve measurements are compared to theoretical predictions to verify the validity of the theoretical device models.

A hardware implementation of the nonlinear processing system is presented using multiple light valves. Experimental system results are given which include level slice, logarithm, exponentiation, and A/D conversion operations. Consideration is given to both one- and two-dimensional input signals.

The limitations of the light valves as they apply to the processing system are discussed, and methods of optimizing the system performance are considered. The methods include optical feedback as a means of improving the response characteristics of the light valves.

ACKNOWLEDGEMENTS

I would like to sincerely thank Dr. A.A. Sawchuk and Dr. T.C. Strand of the Image Processing Institute for their invaluable guidance and assistance during the course of this research. A note of thanks is also extended to the third member of my dissertation committee, Dr. T. Harris.

The efforts of Mr. B. Soffer, Mr. D. Boswell, Dr. L. Miller, and Dr. J. Grinberg of the Hughes Research Laboratories in providing timely information on liquid crystal light valves is greatly appreciated.

A special note of thanks goes to Mr. H.J. Wintroub of The Aerospace Corporation for his unlimited encouragement.

Finally to Judy and the other members of my family for whom this paper was written I would like to express my deepest gratitude. Only their encouragement through many years of sacrifice made this report possible.

TABLE OF CONTENTS

LIST OF FIGURES

ABSTRACT

The use of optical processors to perform linear operations such as Fourier transforming, convolution, and correlation on large bandwidth signals and images has been of great interest and has been investigated for some time. Extension of the processing capability to include nonlinear operations has been the subject of more recent interest and investigation. In this dissertation a method is presented to realize real-time nonlinear operations on two dimensional images through the use of multiple liquid crystal light valves.

A review is given of the theory associated with the light valves. Consideration is given both to electrically controlled cells and photoactivated devices. Special characteristics of the light valves pertinent to the nonlinear processing system are considered in detail. Actual light valve measurements are compared to theoretical predictions to verify the validity of the theoretical device models.

A hardware implementation of the nonlinear processing system is presented using multiple light valves.

Experimental system results are given which include level slice, logarithm, exponentiation, and A/D conversion operations. Consideration is given to both one- and two-dimensional input signals.

The limitations of the light valves as they apply to the processing system are discussed, and methods of optimizing the system performance are considered. The methods include optical feedback as a means of improving the response characteristics of the light valves.

CHAPTER 1

INTRODUCTION

In recent years a number of methods have been described for realizing nonlinear optical transformations on two dimensional input images. The various methods include the use of saturable absorbers [1], coherent optical feedback [2], hybrid optical-electronic systems [3,4], and halftone screen processing [5-8]. More recent innovations have taken advantage of the unique characteristics of optical elements to directly obtain specific nonlinear transformations. In particular, the liquid crystal light valve discussed in depth in this thesis is suitable for the specific operation of parallel analog-to-digital conversion of input images [9]. In general the above implementations suffer from one or more disadvantages. They either require large amounts of optical power as with saturable absorbers, do not offer versatility in the types of transformations that may be performed, require critical optical alignment, or do not offer real time operation. It is the purpose of this paper to describe a system which is not only capable of real time

operation but also provides versatility in the number and types of operations which can be performed. As will be shown, the system takes advantage of the polarization properties of liquid crystal light valves and as such the characteristics of the light valves will be explored in detail. Not only will the results show the utility of the devices in implementing the proposed real time system but also it will be shown that under certain conditions the device can be used as a film substitute in other implementations to achieve real time operation. In particular, the halftone screen process requires as one of its steps the use of an optical thresholding element to achieve the nonlinear effect. As will be shown in subsequent chapters, the liquid crystal light valve can be configured to produce the desired thresholding characteristic.

1.1 Liquid Crystal Light Valve

The optical and electrical properties of liquid crystals have been investigated for many years and their characteristics widely reported in the literature [10-26]. The particular characteristics of liquid crystals of interest for this research are their birefringent properties and their characteristic of becoming aligned in an orderly fashion with externally applied electric fields. It has been demonstrated many times under a variety of

conditions that these two properties can be used to implement devices capable of electrically controlling the transmission of both coherent and incoherent light [20-22]. The general method of construction is to sandwich a layer of liquid crystal material between two transparent conductive electrodes, place the structure between a pair of crossed or parallel polarizers, and pass the light to be controlled through the entire system. On passing through the first polarizer, the light becomes polarized in a single direction. As the polarized light passes through the liquid crystal layer, the birefringent nature of the molecules splits the light into two components, i.e. an ordinary wave and an extraordinary wave. As the two waves traverse the liquid crystal layer they undergo a differential phase shift whose magnitude is determined both by the difference in the index of refraction along each axis of the molecules and the orientation of the molecules with respect to the incident light. Emerging from the liquid crystal material, the two waves recombine to form elliptically polarized light. The magnitude of the light components along each axis of the ellipse is determined by the relative phase retardation of the two waves passing through the liquid crystal material. By controlling the field applied to the liquid crystal layer via the transparent electrodes, the orientation of the molecules relative to the incident light can be varied. Since the

phase retardation is a function of molecular orientation, the strength of the field will determine the magnitude of each axial component of the elliptically polarized light. If the final polarizer is oriented to select only the component along a single axis of the ellipse, electrical control of the light transmission is achieved. This basic system constitutes an electrically controlled liquid crystal light valve.

A number of variations of the light valve have been reported, most involving the use of different liquid crystal materials and different preferred initial alignment of the molecules in the cell [20-26]. In general, three distinct liquid crystal mesophases have been discussed: (a) nematic, (b) cholesteric, and (c) smectic. The nematic mesophase is characterized by parallel alignment of the principal molecular axis of the liquid crystals throughout the cell. The cholesteric mesophase is characterized by a helical orientation of the molecules from one end of the cell to the other. The smectic mesophase is a combination of both nematic and cholesteric mesophases in which the liquid crystals divide into layers throughout the cell. Within each layer nematic type orientation exists but layer-to-layer orientation need not be orderly.

A second class of light valves is photoactivated, and these valves have a photoactive layer in the liquid crystal

sandwich structure [27-30]. By so doing, the field present across the liquid crystal cell may be controlled not only by the overall voltage applied to the structure but also by the amount of light allowed to impinge on the photosensitive layer. In general the structure is divided into an input and output section by an opaque light blocking layer incorporated in the sandwich structure. The output section includes an internal dielectric mirror so that the read illumination (the light source to be controlled) passes through the liquid crystal layer, is reflected off the dielectric mirror, and again passes back through the liquid crystal cell before emerging from the device. The control or write illumination enters the input section of the device and impinges on the photosensitive layer. The photosensitive layer responds to intensity variations in the write illumination by switching the voltage applied across the device onto the liquid crystal layer. In this manner, optical control of the output illumination is achieved in the photoactivated liquid crystal light valve. This type of light valve is the key element in the processing system to be presented and will be considered in detail in the following chapters.

1.2 Organization Of The Dissertation

In Chapter 2 a detailed theory is presented on the liquid crystal light valve described in the previous

section. The theory is presented both for the basic electrically controlled light valve and the photoactivated device. Attention is given to the various possible molecular orientations in the basic cell and electrical and optical properties of the light valves pertinent to the operation of the nonlinear image processing system are detailed.

In Chapter 3 the nonlinear image processor is presented. The general theory governing the operation of the system is first developed. Implementation of special functions using liquid crystal light valves is demonstrated followed by a presentation of hardware implementation of the overall system.

In Chapter 4 the light valve theory developed in Chapter 2 is applied to the actual light valves used in the processing system. Experimental light valve data is presented and compared to theoretical predictions.

Chapter 5 describes the actual experimental processing system. Results are shown for level slice, logarithm, exponentiation, and A/D operations. Operations are shown on both discrete intensity patterns and continuous tone input images.

In Chapter 6 a method is presented for improving the response characteristics of the light valves as required

not only by certain functions in the processing system but also by other light valve applications such as halftone screen processing. Optical feedback is shown both to provide improvement in the thresholding characteristics of the device and to increase the effective gamma of the light valve transfer function.

Finally, in Chapter 7 conclusions are drawn about the presented results. System limitations are discussed and requirements for improved performance are presented.

CHAPTER 2

LIQUID CRYSTAL LIGHT VALVE THEORY

To understand the behavior of the liquid crystal light valve, it is necessary to develop models and theory for the two distinct parts of the light valve, i.e. the liquid crystal layer and the photosensitive layer. The interaction of these two parts must then be determined to predict the light valve performance. Of the three liquid crystal mesophases previously mentioned, only the nematic type liquid crystal will be considered here. Within the class of nematics, consideration will be given to cells in which the principal molecular axis is: a) perpendicular to the substrate surface and uniformly aligned throughout the cell, b) parallel to the substrate surface and uniformly aligned throughout the cell, and c) parallel to the substrate surface but exhibiting a uniform twist through an arbitrary angle over the extent of the cell. The principal factor to be determined for each of these configurations is the phase retardation vs. applied voltage. Second, the cell capacitance as a function of applied voltage must also be determined to understand the interaction of the liquid

crystal layer with the photoconductor.

Although a number of possible photoconductors exist which could be used in the LCLV, only the CdS/CdTe heterojunction type photosensor will be considered here. This is motivated by the fact that all of the photosensitive light valves used in the experimental nonlinear processing system were provided with this type photosensor. Models of the photosensor will be presented and the results of analysis of these models will be applied to the liquid crystal cell analysis to predict overall light valve behavior.

2.1 Liquid Crystal Continuum Theory

The best first order predictions of the behavior of nematic liquid crystals has been through the use of a continuum theory developed by Oseen [10], Zocker [11], and Frank [12]. The basis of the theory is the minimization of the free energy in the liquid crystal layer while under the influence of an applied external field. The distortion free energy density of the liquid crystals is given by [13]

$$F = \frac{1}{2}[K_{11}(\mathrm{div}\bar{n})^2+K_{22}(\bar{n}\cdot\mathrm{curl}\bar{n}+\bar{q}_0)^2+K_{33}(\bar{n}\times\mathrm{curl}\bar{n})^2] \qquad (2.1)$$

where $\bar{n}$ is the unit vector parallel to the local molecular axis, $\bar{q}_0$ is the periodicity of molecular rotation in the liquid crystal layer ($\bar{q}_0=0$ for a nematic system), and the K_{ii} are the Frank elastic constants for the liquid crystal

material. The three terms in Eq. (2.1) correspond to the distortions of splay, twist, and bend shown diagramatically in Fig. 2-1. When an external field is applied to the liquid crystal layer, a fourth term must be added to the free energy equation (2.1). This term is given by

$$F_E = -\frac{1}{2}\epsilon_a(\bar{n}\cdot\bar{E})^2 \tag{2.2}$$

where $\bar{E}$ is the applied electric field vector and $\epsilon_a = \epsilon_{11} - \epsilon_1$ is the dielectric anisotropy.

2.2 Uniform Perpendicular Liquid Crystal Alignment

When the liquid crystal molecular axis is initially aligned perpendicularly to the substrate surfaces, the free energy per unit wall area given by Eqs. (2.1) and (2.2) becomes

$$F = \frac{1}{2}\int_{-d/2}^{d/2}[K(\frac{\partial\phi}{\partial z})^2 - \epsilon_a E^2\sin^2\phi]dz \tag{2.3}$$

where ϕ is the angle between the axis of the applied field and the molecular axis of the liquid crystals and the simplification $K_{11}=K_{33}=K$ has been made. The geometry used for Eq. (2.3) is shown in Fig. 2-2. Minimizing F with respect to ϕ, one obtains for the Euler equation

$$G = K\phi'^2 - \epsilon_a E^2\sin^2\phi \tag{2.4}$$

$$d/dz(\frac{\partial G}{\partial \phi'}) - \frac{\partial G}{\partial \phi} = \frac{d}{dz}[2K\phi'] + 2\epsilon_a E^2\cos\phi\sin\phi = 0 \tag{2.5}$$

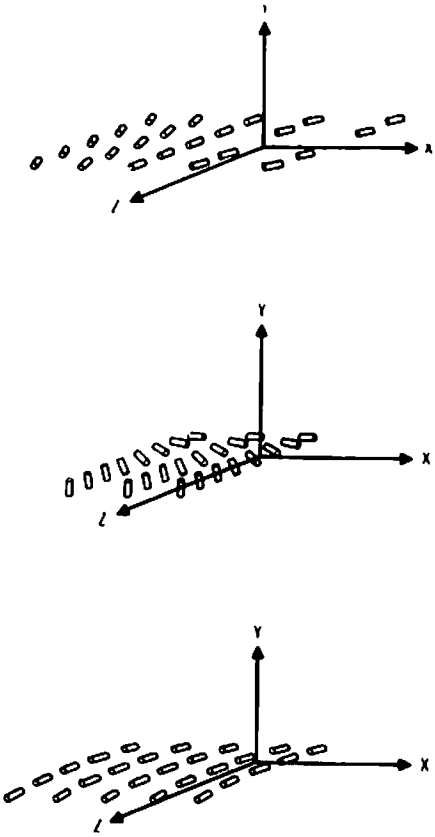

Figure 2-1 Geometric representation of liquid crystal molecular distortions
(a) Splay
(b) Twist
(c) Bend

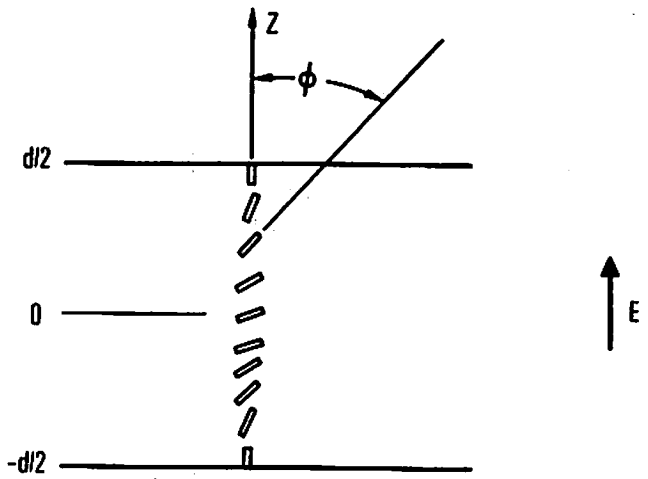

Figure 2-2 Geometry of uniform perpendicular aligned cell

$$2K\phi''+2\varepsilon_a E^2\cos\phi\sin\phi = 0 \qquad (2.6)$$

or

$$\xi^2 \frac{d^2\phi}{dz^2} + \sin\phi\cos\phi = 0 \qquad (2.7)$$

where

$$\xi = (\frac{K}{\varepsilon_a})^{\frac{1}{2}} E^{-1} \quad . \qquad (2.8)$$

Integrating once gives

$$\xi\frac{d\phi}{dz} = (1-k^2\sin^2\phi)^{\frac{1}{2}}/k \quad . \qquad (2.9)$$

Since the structure is symmetric about the midplane, this requires that $\frac{d\phi}{dz}=0$ at Z=0. From this one obtains

$$k = \frac{1}{\sin\phi_m} \qquad (2.10)$$

where ϕ_m is the maximum value ϕ obtains at Z=0. Taking note of the symmetry of the structure and the boundary condition that $\phi=0$ at Z=d/2, further integration of Eq. (2.9) yields

$$F(k,\phi) = (k\xi)^{-1}[\frac{d}{2} - z] \qquad z > 0 \qquad (2.11)$$

where $F(k,\phi)$ is an elliptic integral of the first kind. Equation (2.11) together with

$$F(k,\phi_m) = (k\xi)^{-1} d/2 \qquad (2.12)$$

provides the relationship between the distance through the

cell Z and the optic axis tilt ϕ of the liquid crystal as a function of the applied field E. Equation (2.12) has a solution (other than $\phi_m=0$) only for $d > \pi\xi$. This implies that a critical voltage

$$V_c = Ed = \pi\left(\frac{k}{\varepsilon_a}\right)^{\frac{1}{2}} \tag{2.13}$$

exists below which ϕ remains zero throughout the structure. With the change of variables

$$z = z' \cdot d/2 \qquad 0 \leq z' \leq 1 \tag{2.14}$$

Eq. (2.11) becomes

$$F(k,\phi) = (k\xi)^{-1}(d/2)(1-z') \tag{2.15}$$

and using Eq. (2.8) we obtain

$$F(k,\phi) = V(1-z')/2k\left(\frac{K}{\varepsilon_a}\right)^{\frac{1}{2}} \tag{2.16}$$

$$F(k,\phi) = \frac{V}{V_c}\frac{\pi}{2k}(1-z') \ . \tag{2.17}$$

Similarly Eq. (2.12) becomes

$$F(k,\phi_m) = \frac{V}{V_c}\frac{\pi}{2k} \ . \tag{2.18}$$

A plot of ϕ_m vs $\frac{V}{V_c}$ is shown in Fig. 2-3. A typical plot of ϕ vs Z' for $\frac{V}{V_c}=2$ is shown in Fig. 2-4. It has been shown[23] that for normally incident monochromatic light of wavelength λ, the total phase retardation through the cell is given by

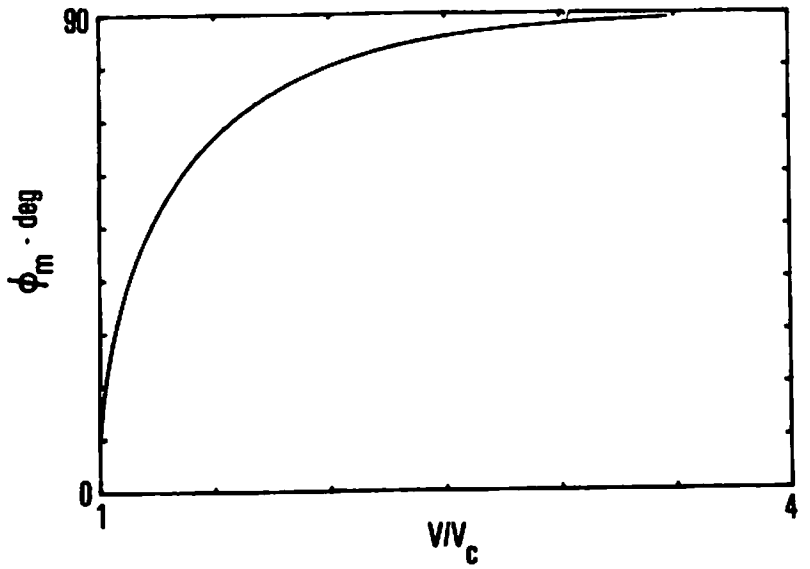

Figure 2-3 Maximum tilt angle vs. normalized applied voltage for uniform perpendicular cell

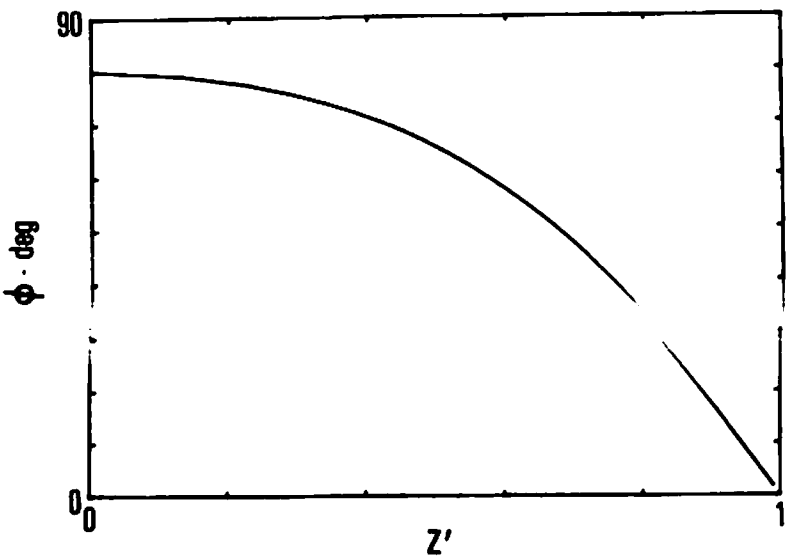

Figure 2-4 Tilt angle vs. distance through uniform perpendicular cell with V/Vc=2

$$\delta = \frac{4\pi\Delta n}{\lambda} \int_0^{d/2} \sin^2\phi(z)dz \qquad (2.19)$$

where Δn is the difference between the ordinary and extraordinary refractive indices for the liquid crystal. Defining

$$\delta_0 = \frac{2\pi\Delta nd}{\lambda} \qquad (2.20)$$

then Eq. (2.19) becomes

$$\delta/\delta_0 = \frac{2}{d} \int_0^{d/2} \sin^2\phi(z)dz \qquad (2.21)$$

and with the change of variables as in Eq. (2.14)

$$\delta/\delta_0 = \int_0^1 \sin^2\phi(z')dz' \quad . \qquad (2.22)$$

Equations (2.10), (2.17), (2.18), and (2.22) were used to evaluate δ/δ_0 vs $\frac{V_c}{V}$ for $1 \leq \frac{V}{V_c} \leq 6$. The results are shown in Fig. 2-5 fitted to a fifth order polynomial with coefficients

$$\begin{aligned} c_0 &= 0.991479 \\ c_1 &= -0.498746 \\ c_2 &= -0.721406 \\ c_3 &= 2.26344 \\ c_4 &= -3.31683 \\ c_5 &= 1.29646 \end{aligned} \qquad (2.23)$$

2.3 Uniform Parallel Liquid Crystal Alignment

When the liquid crystal molecular axis lies parallel with the substrate surfaces, minimization of the free energy equation leads to a closed form solution. The

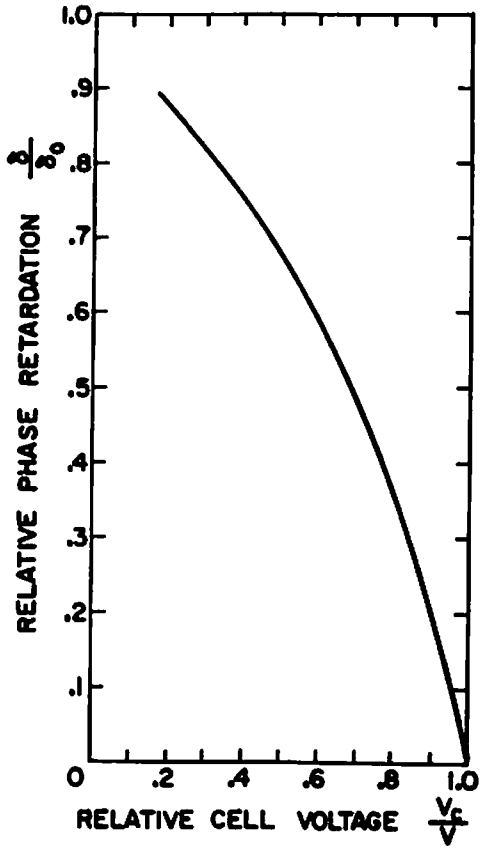

Figure 2-5 Normalized phase retardation vs. inverse normalized voltage for uniform perpendicular cell

geometry is shown in Fig. 2-6. Taking note of the symmetry of the structure, the free energy equation for this case is given by

$$F = \int_0^{d/2} [K(\frac{\partial\phi}{\partial z})^2 - \varepsilon_a E^2 \cos^2\phi] dz. \qquad (2.24)$$

Again minimizing F with respect to ϕ, the free energy is minimized by satisfying

$$\xi^2 \frac{d^2\phi}{dz^2} = \frac{\sin 2\phi}{2} \qquad (2.25)$$

where again

$$\xi = (\frac{K}{\varepsilon_a})^{\frac{1}{2}} E^{-1} \quad . \qquad (2.26)$$

Multiplying both sides of Eq. (2.25) by $\frac{d\phi}{dz}$ and integrating over Z we obtain

$$\xi^2 \int \frac{d\phi}{dz} \frac{d^2\phi}{dz^2} dz = \frac{1}{2} \int \sin 2\phi \frac{d\phi}{dz} dz \qquad (2.27)$$

$$\frac{\xi^2}{2} (\frac{d\phi}{dz})^2 = -\frac{1}{4} \cos 2\phi + K_1 \quad . \qquad (2.28)$$

From Fig. 2-6 it is seen that ϕ is maximum at the ends of the cell and reaches a minimum value at midplane. Thus for the limiting condition when $\phi=0$ at $z=d/2$, $\frac{d\phi}{dz}$ is necessarily zero implying that $K_1=1/4$ in Eq. (2.28). Thus

$$\xi^2 (\frac{d\phi}{dz})^2 = \frac{1}{2} - \frac{1}{2} \cos 2\phi \qquad (2.29)$$

$$\xi^2 (\frac{d\phi}{dz})^2 = \sin^2\phi \qquad (2.30)$$

$$\int \frac{d\phi}{\sin\phi} = \pm \frac{1}{\xi} \int dz \qquad (2.31)$$

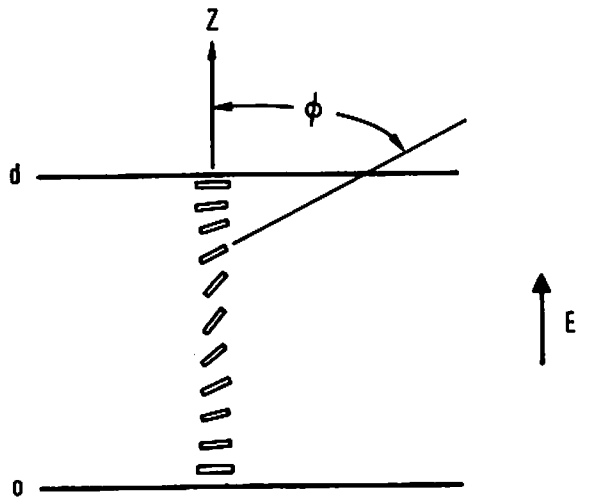

Figure 2-6 Geometry of uniform parallel cell

$$\ell n \tan\frac{\phi}{2} = \pm z/\xi \qquad (2.32)$$

$$\tan\frac{\phi}{2} = e^{\pm z/\xi} \quad . \qquad (2.33)$$

From the conditions that $\phi=\pi/2$ at $Z=0$ and ϕ decreases as Z is increased from 0 to d/2, Eq. (2.33) becomes

$$\tan\frac{\phi}{2} = e^{-z/\xi} \quad . \qquad (2.34)$$

The total phase retardation through the cell of thickness d is given as in Eq. (2.19)

$$\delta = \frac{4\pi\Delta n}{\lambda} \int_0^{d/2} \sin^2\phi(z)\,dz \qquad (2.35)$$

where $\phi(z)$ is as given by Eq. (2.34). Again defining δ_0 as in Eq. (2.20), then eq. (2.35) becomes

$$\delta/\delta_0 = \frac{2}{d}\int_0^{d/2} \sin^2\phi(z)\,dz \qquad (2.36)$$

$$\delta/\delta_0 = \frac{2}{d}\int_0^{d/2} [1-\cos^2\phi(z)]\,dz \qquad (2.37)$$

$$\delta/\delta_0 = 1-\frac{2}{d}\int_0^{d/2} [\cos^2\frac{\phi}{2} - \sin^2\frac{\phi}{2}]^2 dz \qquad (2.38)$$

$$\delta/\delta_0 = 1-\frac{2}{d}\int_0^{d/2} \left[\frac{\cos^2\phi/2-\sin^2\phi/2}{\cos^2\phi/2+\sin^2\phi/2}\right]^2 dz \qquad (2.39)$$

$$\delta/\delta_0 = 1-\frac{2}{d}\int_0^{d/2} \left[\frac{1-\tan^2\phi/2}{1+\tan^2\phi/2}\right]^2 dz \quad . \qquad (2.40)$$

Using Eq. (2.34)

$$\delta/\delta_0 = 1-\frac{2}{d}\int_0^{d/2} \left[\frac{1-e^{-2z/\xi}}{1+e^{-2z/\xi}}\right]^2 dz \qquad (2.41)$$

$$\delta/\delta_0 = 1-\frac{2}{d}\int_0^{d/2} \tanh^2(z/\xi)\,dz \qquad (2.42)$$

$$\delta/\delta_0 = \frac{2\xi}{d}\tanh\frac{d}{2\xi} \quad . \qquad (2.43)$$

With V=Ed, $V_c=2(\frac{K}{\varepsilon_a})^{\frac{1}{2}}$ and the aid of Eq. (2.26), Eq. (2.43) becomes

$$\delta/\delta_0 = \frac{V_c}{V}\tanh\frac{V}{V_c} \quad . \qquad (2.44)$$

The normalized phase retardation vs. $\frac{V_c}{V}$ is shown in Fig. 2-7. As seen in the figure, for $\frac{V_c}{V} << 1$ the normalized phase retardation simply goes as 1/V.

2.4 Twisted Nematic Cell

When the liquid crystal molecules rotate through an arbitrary angle over the distance through the cell, the system is somewhat more difficult to analyze. The approach used here is that of Leslie [31] and in effect produces the molecular tilt and twist angles as a function of distance through the cell and applied field. From this angular information the phase retardation across the cell is then calculated. The geometry for the twist cell is shown in Fig. 2-8.

The Leslie equations for the tilt and twist angles (θ , ϕ) are given by

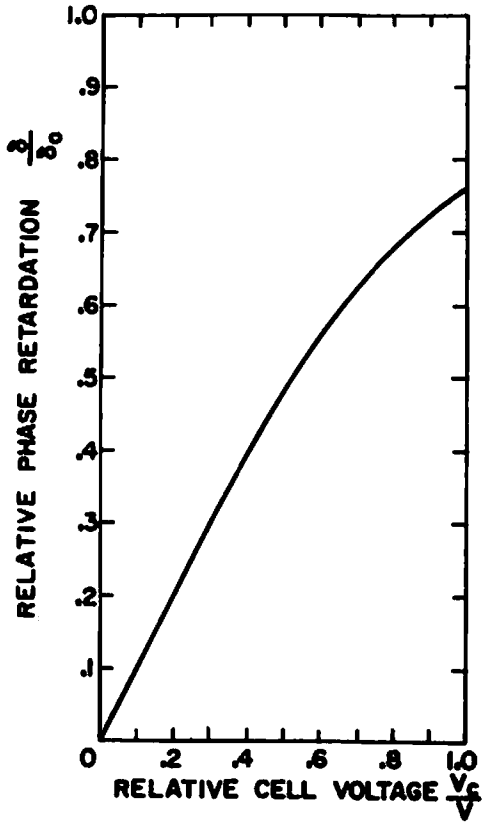

Figure 2-7 Normalized phase retardation vs. inverse normalized voltage for uniform parallel cell

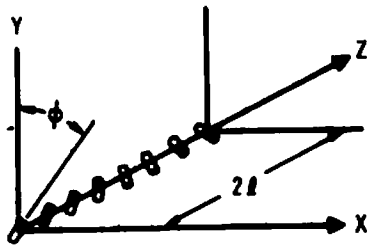

(a)

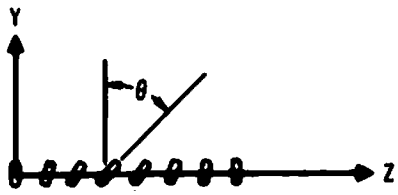

(b)

Figure 2-8 Geometry of twisted nematic cell
(a) Twist
(b) Tilt

$$z = \int_0^{\theta} \left[\frac{f(\psi)}{\varepsilon_a E^2 (\sin^2\theta_m - \sin^2\psi) + k^2 \left(\frac{1}{g(\theta_m)} - \frac{1}{g(\psi)} \right)} \right]^{\frac{1}{2}} d\psi \quad 0 \leq z \leq L \tag{2.45}$$

$$\phi = -\phi_0 + \int_0^{\theta} \left[\frac{f(\psi)}{\varepsilon_a E^2 (\sin^2\theta_m - \sin^2\psi) + k^2 \left(\frac{1}{g(\theta_m)} - \frac{1}{g(\psi)} \right)} \right]^{\frac{1}{2}} \frac{k}{g(\psi)} d\psi \quad 0 \leq z \leq L \tag{2.46}$$

where Z is the dimension through the liquid crystal layer of thickness d=2L, E is the applied field, ε_a is the dielectric anisotropy, θ_m is the maximum tilt angle at Z=L, and k and ϕ_0 are constants. The functions $f(\theta)$ and $g(\theta)$ are given by

$$f(\theta) = K_{11}\cos^2\theta + K_{33}\sin^2\theta \tag{2.47}$$

$$g(\theta) = (K_{22}\cos^2\theta + K_{33}\sin^2\theta)\cos^2\theta \tag{2.48}$$

where K_{11}, K_{22}, and K_{33} are again the Frank elastic constants for splay twist, and bend. The boundary conditions for the system are $\theta(0) = 0$, $\theta(2L) = 0$, $\theta(L) = \theta_m$, $\phi(0) = -\phi_0$, $\phi(2L) = \phi_0$, $\phi(L) = 0$.

From the boundary conditions, θ_m and k must satisfy

$$L = \int_0^{\theta_m} \left[\frac{f(\theta)}{\varepsilon_a E^2 (\sin^2\theta_m - \sin^2\theta) + k^2 \left(\frac{1}{g(\theta_m)} - \frac{1}{g(\theta)} \right)} \right]^{\frac{1}{2}} d\theta \tag{2.49}$$

$$\phi_0 = \int_0^{\theta_m} \left[\frac{f(\theta)}{\varepsilon_a E^2 (\sin^2\theta_m - \sin^2\theta) + k^2 \left(\frac{1}{g(\theta_m)} - \frac{1}{g(\theta)} \right)} \right]^{\frac{1}{2}} \frac{k d\theta}{g(\theta)} \quad . \tag{2.50}$$

Through minimization of the free energy equation, the critical field is given by

$$\varepsilon_a L^2 E_c^2 = K_{11}(\pi/2)^2 + (K_{33}-2K_{22})\phi_0^2 \quad . \tag{2.51}$$

Rewriting Eq. (2.51) by letting

$$K = \frac{K_{11}}{K_{33}}(\pi/2)^2 + (1-2\frac{K_{22}}{K_{33}})\phi_0^2 \tag{2.52}$$

then

$$\varepsilon_a = \frac{K_{33}K}{L^2 E_c^2} \quad . \tag{2.53}$$

From Eqs. (2.47) and (2.48)

$$f(\theta) = K_{33}(\frac{K_{11}}{K_{33}}\cos^2\theta + \sin^2\theta) \tag{2.54}$$

$$f(\theta) = K_{33}f'(\theta) \tag{2.55}$$

$$g(\theta) = K_{33}(\frac{K_{22}}{K_{33}}\cos^2\theta + \sin^2\theta)\cos^2\theta \tag{2.56}$$

$$g(\theta) = K_{33}g'(\theta) \quad . \tag{2.57}$$

Defining

$$k = \frac{K_{33}C}{L} \tag{2.58}$$

where C is a constant, then using Eqs. (2.53)-(2.58) and letting $E/E_c = E_R$, Eq. (2.50) becomes

$$\phi_0 = \int_0^{\theta_m} \left[\frac{f'(\theta)}{KE_R^2(\sin^2\theta_m - \sin^2\theta) + C^2(\frac{1}{g'(\theta_m)} - \frac{1}{g'(\theta)})}\right]^{\frac{1}{2}} \frac{c\,d\theta}{g'(\theta)}. \tag{2.59}$$

Letting

$$B = \frac{E_R^2}{c^2} \tag{2.60}$$

then Eq. (2.59) becomes

$$\phi_0 = \int_0^{\theta_m} \left[\frac{f'(\theta)}{KB(\sin^2\theta_m - \sin^2\theta) + \frac{1}{g'(\theta_m)} - \frac{1}{g'(\theta)}} \right]^{\frac{1}{2}} \frac{d\theta}{g'(\theta)} \quad . \qquad (2.61)$$

A similar reduction of Eq. (2.49) yields

$$E_R = \int_0^{\theta_m} \left[\frac{f'(\theta)}{K(\sin^2\theta_m - \sin^2\theta) + \frac{1}{B}\left(\frac{1}{g'(\theta_m)} - \frac{1}{g'(\theta)}\right)} \right]^{\frac{1}{2}} d\theta \quad . \qquad (2.62)$$

Equation (2.45) is then given by

$$\frac{Z}{L} = \frac{1}{E_R} \int_0^{\theta} \left[\frac{f'(\psi)}{K(\sin^2\theta_m - \sin^2\psi) + \frac{1}{B}\left(\frac{1}{g'(\theta_m)} - \frac{1}{g'(\psi)}\right)} \right]^{\frac{1}{2}} d\psi \qquad (2.63)$$

and Eq. (2.46) becomes

$$\phi = -\phi_0 + \int_0^{\theta} \left[\frac{f'(\psi)}{KB(\sin^2\theta_m - \sin^2\psi) + \frac{1}{g'(\theta_m)} - \frac{1}{g'(\psi)}} \right]^{\frac{1}{2}} \frac{d\psi}{g'(\psi)} \quad . \qquad (2.64)$$

The preceding equations were solved numerically by determining B for a given θ_m $0 \leq \theta_m \leq \pi/2$ from Eq. (2.61) and then using the value of B to determine E_R from Eq. (2.62). Given θ_m, E_R, and B, θ vs. Z and ϕ vs. Z were then determined using Eqs. (2.63) and (2.64). To facilitate computation and reduce computational errors, the following substitutions were made

$$\frac{1}{g'(\theta_m)} - \frac{1}{g'(\theta)} = \frac{[A_2\cos^2\theta + \sin^2\theta]\cos^2\theta - [A_2\cos^2\theta_m + \sin^2\theta_m]\cos^2\theta_m}{g'(\theta_m)g'(\theta)} \qquad (2.65)$$

where

$$A_2 = \frac{K_{22}}{K_{33}} \quad . \qquad (2.66)$$

Through further trigonometric reduction,

$$\frac{1}{g'(\theta_m)} - \frac{1}{g'(\theta)} = \frac{\sin(\theta_m+\theta)\sin(\theta_m-\theta)\,[A_2+(A_2-1)\cos(\theta_m+\theta)\cos(\theta m-\theta)\,]}{g'(\theta_m)g'(\theta)} \qquad (2.67)$$

Further

$$\sin^2\theta_m - \sin^2\theta = \sin(\theta_m+\theta)\sin(\theta_m-\theta) \qquad (2.68)$$

Thus for example, Eq. (2.62) becomes

$$E_R = \int_0^{\theta_m} \left[\frac{f'(\theta)}{\sin(\theta_m+\theta)\sin(\theta_m-\theta)\left\{K+\dfrac{A_2+(A_2-1)\cos(\theta_m+\theta)\cos(\theta_m-\theta)}{Bg'(\theta_m)g'(\theta)}\right\}}\right]^{1/2} d\theta \,. \qquad (2.69)$$

Using the typical values for the Frank elastic constants [24]

$$A_1 = \frac{K_{11}}{K_{33}} = 0.79$$

$$A_2 = \frac{K_{22}}{K_{33}} = 0.48 \qquad (2.70)$$

Eqs. (2.61)-(2.64) were used together with the computational aids given by Eqs. (2.67) and (2.68) to compute the tilt and twist angles of the liquid crystal optical axis as a function of distance through the cell. Figures 2-9 and 2-10 show the tilt angle θ and twist angle ϕ for transmission type twist cells with overall twist angles of 90° and 45° respectively. The curves are plotted as a function of applied field. The curves shown are in good agreement with the results given by Berreman [24] for a 90° twist cell.

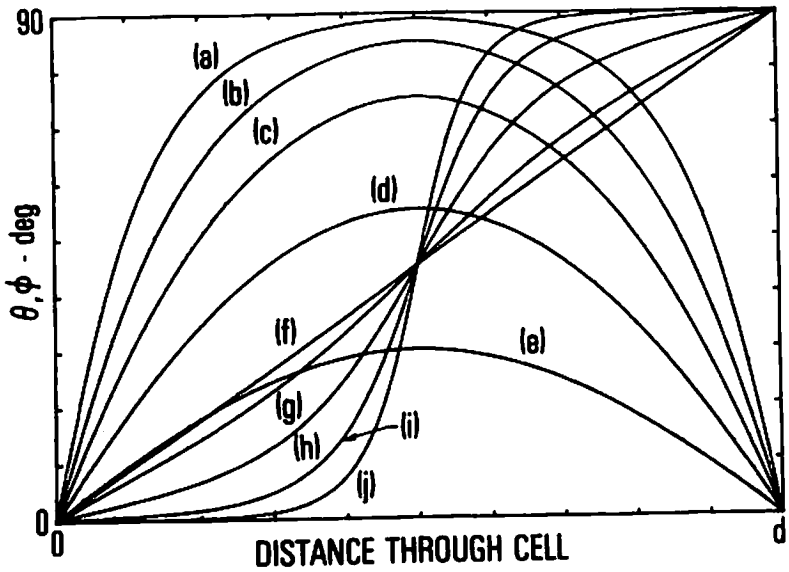

Figure 2-9 Twist and tilt angles vs. distance through 90 degree twisted nematic cell
(a-e) Tilt angle for E/Ec=3.45;2.38;1.69; 1.25;1.05
(f-j) Twist angle for E/Ec=1.05;1.25;1.69; 2.38;3.45

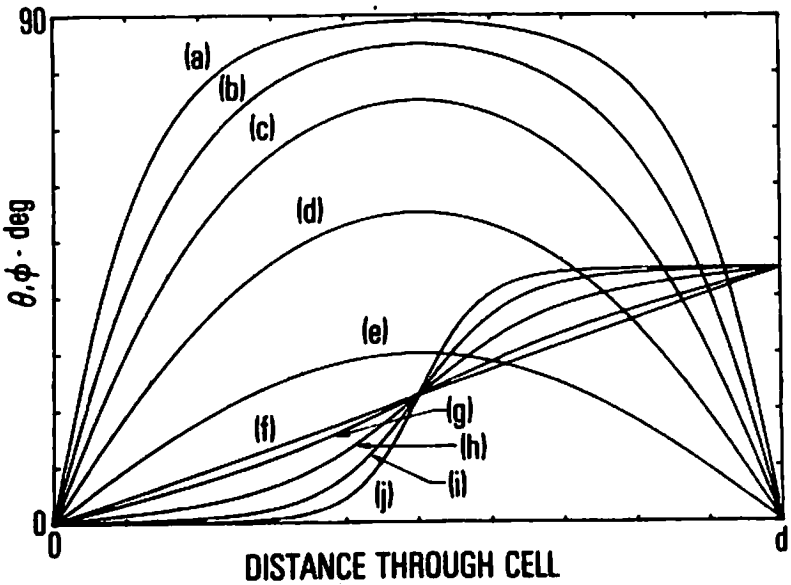

Figure 2-10 Twist and tilt angles vs. distance through 45 degree twisted nematic cell
(a-e) Tilt angle for E/Ec=3.68;2.58;1.84; 1.33;1.08
(f-j) Twist angle for E/Ec=1.08;1.33;1.84; 2.58;3.68

To find the transmission characteristics of the cell, the formalism developed by Jones [32] may be employed. Using the notation

$$\bar{E} = \underline{A}\,\underline{P}\,\bar{V} \tag{2.71}$$

where $\bar{V}$ is the two element vector $\bar{V}=\begin{bmatrix} u_x \\ u_y \end{bmatrix}$ representing the polarization components of the incoming wave, $\underline{P}$ is a complex polarization matrix representing the effects of the liquid crystal cell, and $\underline{A}$ is a matrix representing the effects of a polarization analyzer placed at the output of the cell, then the intensity transmission of the cell is given by

$$T = \bar{E}\,\bar{E}^* \tag{2.72}$$

where * denotes complex conjugate. The matrix $\underline{P}$ is found by dividing the cell up into a large number of subintervals and treating the optical parameters of the liquid crystal layer within each subinterval as being spatially invariant. Each subinterval i can then be represented by a polarization matrix $\underline{P_i}$. The polarization matrix $\underline{P}$ for the entire cell is then simply given by the product

$$\underline{P} = \prod_{i=N}^{1} \underline{P_i} \tag{2.73}$$

with the $\underline{P_i}$'s taken in the proper sequence. $\underline{P_i}$ in Eq. (2.73) is given by the product of a phase delay matrix $\underline{D_i}$ defined by the phase retardation between the ordinary

and exraordinary waves after passing through the ith layer, and a rotation matrix $\underline{R_i}$ used to derive the polarization components of the incoming wave parallel and orthogonal to the optical axis of the ith layer. Thus

$$\underline{P_i} = \underline{D_i}\,\underline{R_i} \tag{2.74}$$

Using the Jones notation

$$\underline{R_i} = \begin{bmatrix} \cos\Delta\phi_i & \sin\Delta\phi_i \\ -\sin\Delta\phi_i & \cos\Delta\phi_i \end{bmatrix} \tag{2.75}$$

where $\Delta\phi_i$ is the incremental twist angle from the (i-1)st to the ith layer, i.e. $\Delta\phi_i = \phi_i - \phi_{i-1}$. The delay matrix is given by

$$D_i = \begin{bmatrix} e^{j(\delta_i/2)} & 0 \\ 0 & e^{-j(\delta_i/2)} \end{bmatrix} \tag{2.76}$$

where δ_i is the phase retardation due to the ith layer. δ_i is given by [23]

$$\delta_i = \frac{2\pi\Delta n d_i}{\lambda} \sin^2\nu \tag{2.77}$$

where Δn is the birefringence $(n_0 - n_e)$ of the liquid crystals, d_i is the layer thickness, λ the wavelength of the incident light and ν the angle between the optical axis of the liquid crystal and the direction of propagation of the light wave. Using the geometry of Fig. 2-8,

$$\nu = \pi/2 - \theta \tag{2.78}$$

Using Eqs. (2.71)-(2.78) and angular data obtained from Eqs. (2.61)-(2.70), the transmission characteristics of 10 micron thick and 2 micron thick transmission type cells are shown in Fig. 2-11. The assumed data was $\Delta n=0.25$, $\lambda=514.5$ nm, total twist=90^{o}, and the polarizer and analyzer axes parallel to the liquid crystal optical axis at the input of the device. Both curves are plotted as a function of the applied electric field normalized to the critical field E_c. In computing the curves of Fig. 2-11, the number of subintervals used to guarantee convergence was numerically determined through an iterative computational procedure.

The preceding theory may be extended to include the reflection mode twisted nematic liquid crystal devices. In these devices the incident light passes through the liquid crystal layer where it is operated on by the polarization matrix. The light is then reflected off of an internal dielectric mirror and passes a second time through the layer, finally exiting through the entrance plane where it is directed toward a polarization analyzer. The matrix equation for this structure is given by

$$\bar{E} = \underline{A}\,\underline{P'}\,\bar{V} \tag{2.79}$$

where $\bar{E}$, $\underline{A}$, and $\bar{V}$ are as previously defined. $\underline{P'}$ may be considered as the product of two matrices

$$\underline{P}' = \underline{P}''\,\underline{P} \tag{2.80}$$

where $\underline{P}$ is the polarization matrix describing the effects of the liquid crystal layer on the propagating wave during its first pass through the cell. $\underline{P}$ is as given in Eqs. (2.73)-(2.76). Using the subinterval approach, the elements of $\underline{P}''$ are simply the elements of $\underline{P}$ taken in reverse order. The phase retardation through a given layer is invariant with the direction of propagation thus

$$\underline{D}_i' = \underline{D}_i \tag{2.81}$$

The incremental twist angle $\Delta\phi_i'$ will be in the opposite sense of $\Delta\phi$ thus

$$\Delta\phi_i' = -\Delta\phi_i \tag{2.82}$$

and

$$R_i' = \begin{bmatrix} \cos\Delta\phi_i' & \sin\Delta\phi_i' \\ -\sin\Delta\phi_i' & \cos\Delta\phi_i' \end{bmatrix} = \begin{bmatrix} \cos(-\Delta\phi) & \sin(-\Delta\phi) \\ -\sin(-\Delta\phi) & \cos(-\Delta\phi) \end{bmatrix} = R_i^T. \tag{2.83}$$

Inspection of Eq. (2.76) shows $D_i = D_i^T$. Thus the overall matrix equation for the transmission characteristics of the reflection mode device is given by

$$\overline{E} = \underline{A}\,\underline{P}''\underline{P}\,\overline{V} \tag{2.84}$$

$$\overline{E} = \underline{A}\,\underline{R}_1'\,\underline{D}_1'\cdots\underline{R}_N'\,\underline{D}_N'\,\underline{D}_N\,\underline{R}_N\cdots\underline{D}_2\,\underline{R}_2\,\underline{D}_1\,\underline{R}_1\,\overline{V} \tag{2.85}$$

$$\overline{E} = \underline{A}\,\underline{R}_1^T\,\underline{D}_1^T\cdots\underline{R}_N^T\,\underline{D}_N^T\,\underline{D}_N\,\underline{R}_N\cdots\underline{D}_2\,\underline{R}_2\,\underline{D}_1\,\underline{R}_1\,\overline{V} \tag{2.86}$$

$$\bar{E} = \underline{A}_{\perp} P_{\perp}^{T} P \bar{V} \quad . \tag{2.87}$$

The twisted nematic device used in the experimental procedure in this paper utilizes reflection mode, 45^{o} twist angle and operates between a crossed polarizer/analyzer pair. Further, the polarization of the incident light is parallel to the optical axis of the liquid crystals at the entrance plane of the device. Using these constraints together with $\Delta n=0.25$, $\lambda=514.5$ nm, and a liquid crystal cell thickness of 2 microns, then Eqs. (2.87), (2.61)-(2.68), and (2.72)-(2.78) give the computed transmission vs. normalized field strength shown in Fig. 2-12.

2.5 Liquid Crystal Cell Impedance

As noted earlier, some types of liquid crystal devices are activated by a light sensitive photosensor. With this type of device, the load impedance of the liquid crystal cell is of importance in determining theoretical device performance. The impedance of the liquid crystal may be modeled as the parallel combination of a resistive component R_{LC} defined by the bulk resistivity of the liquid crystals ($\sim 10^{8}$ $\Omega \cdot$cm) and a capacitive element C_{LC} defined by the physical dimensions of the cell and the dielectric constant of the liquid crystals. Since the bulk resistivity is not a function of liquid crystal

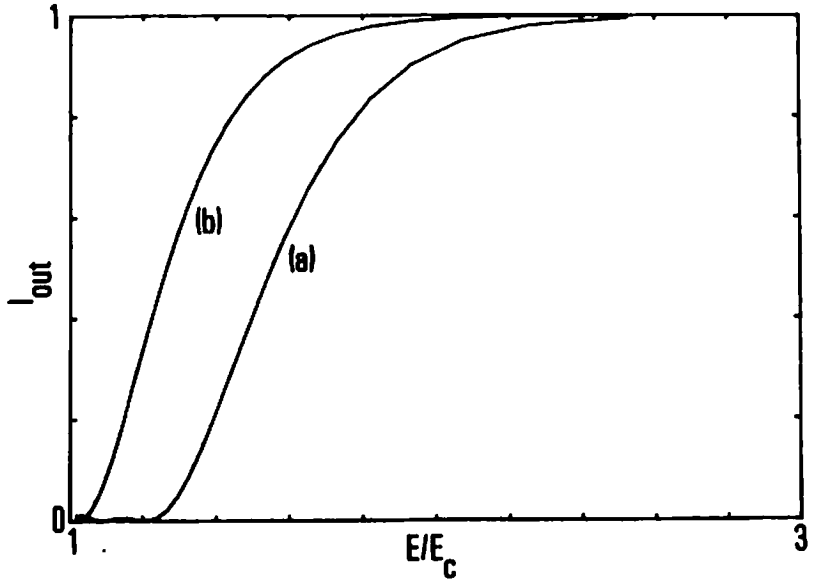

Figure 2-11 Transmission vs. normalized voltage for transmission mode 90 degree twisted nematic cell
(a) 10 micron cell
(b) 2 micron cell

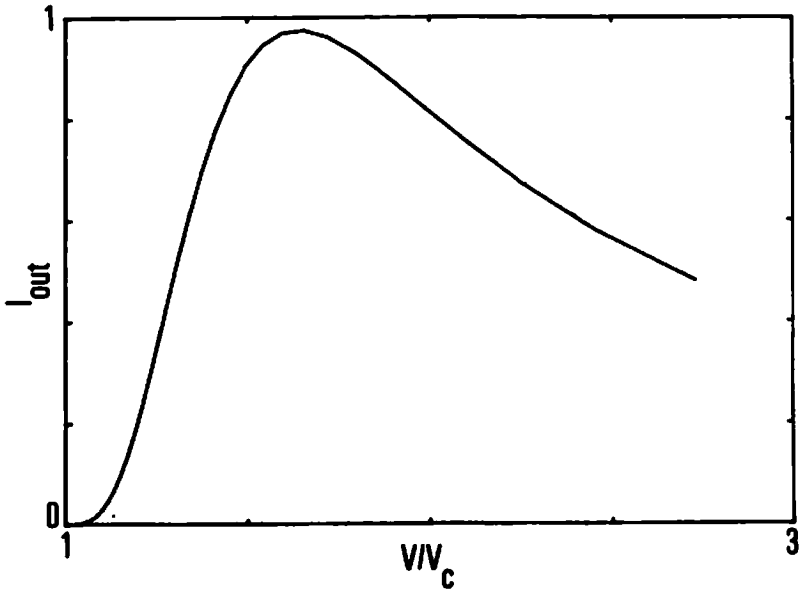

Figure 2-12 Transmission vs. normalized voltage for reflection mode 45 degree twisted nematic cell

orientation, then R_{LC} will be independent of the voltage applied across the cell. However, due to the anisotropy of the liquid crystals, the dielectric constant and therefore C_{LC} is a function of liquid crystal orientation. Thus the impedance of the cell is dependent on the applied voltage. To determine this dependence, if ε_{11} and ε_1 represent the principal dielectric constants of the liquid crystal parallel to and normal to the long molecular axis respectively, then from the geometry of Fig. 2-8 for the twisted nematic device, the effective dielectric constant along the Z axis is given by

$$\varepsilon_e = \varepsilon_{11}\sin^2\theta + \varepsilon_1\cos^2\theta \quad . \tag{2.88}$$

If the cell is again divided into N layers, then the total cell capacitance is given by the series combination of the capacitance of each layer, i.e.,

$$C_{Total} = \frac{1}{\sum_{i=1}^{N} \frac{1}{C_i}} \tag{2.89}$$

If each layer is assumed small enough such that the effective dielectric constant becomes spatially invariant, then the capacitance of an individual layer is given by

$$C_i = \frac{\varepsilon_0 \varepsilon_e(i) A}{d_i} \tag{2.90}$$

Substituting Eq. (2.90) into Eq. (2.89), then the total capacitance per unit area is given by

$$\frac{CT}{A} = \frac{\varepsilon_0}{\sum_{i=1}^{N} \frac{d_i}{\varepsilon_e(i)}} \tag{2.91}$$

where $\varepsilon_e(i)$ is given by Eq. (2.88) with $\theta = \theta_i$. Using the data of Fig. 2-10 to determine θ_i and d_i, with ε_{11}=16 and ε_l=5, then Fig. 2-13 shows the total capacitance per unit area vs. normalized voltage for a 4 micron thick liquid crystal layer. This data will subsequently be used for predicting device performance when the liquid crystal cell is mated to a CdS/CdTe photosensor.

A similar numerical approach must be used for determining the cell impedance for the perpendicularly aligned uniform device. Taking note of the geometry in Fig. 2-2 and using the notation developed in section 2.2, the effective dielectric constant is given by

$$\varepsilon_e = \varepsilon_{11}\cos^2\phi + \varepsilon_l\sin^2\phi \quad . \qquad (2.92)$$

The required cell capacitance per unit area is found by substituting Eq. (2.92) into Eq. (2.91) and performing the necessary summation. Angular data for each subinterval is provided by solution of Eqs. (2.15) and (2.16) for a given normalized applied cell voltage (V/V_c). With ε_{11}=4.92 and ε_l=5.27 [23] then Fig. 2-14 shows the total cell capacitance per unit area vs. normalized voltage for an 11 micron thick perpendicularly aligned cell.

As is the case for the phase retardation, the cell impedance for the parallel aligned uniform cell has a closed form solution. From the geometry shown in Fig. 2-6,

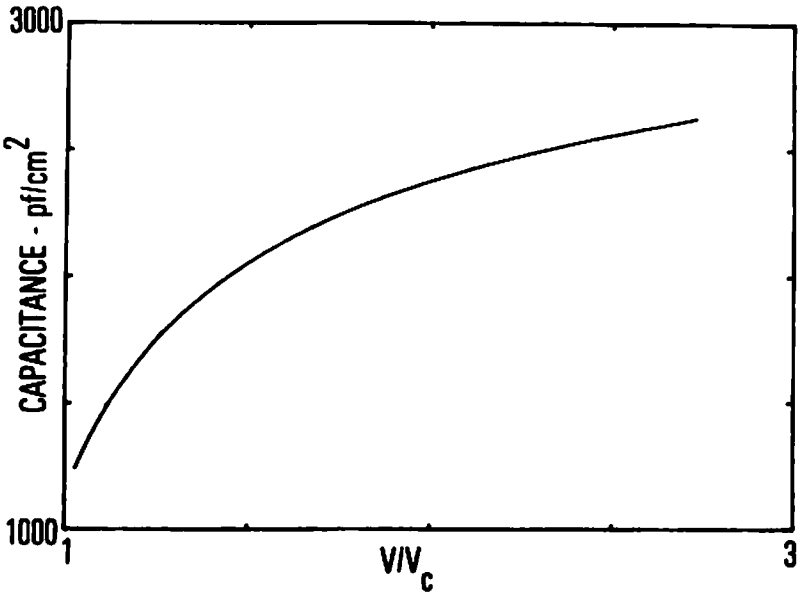

Figure 2-13 Cell capacitance vs. normalized voltage for a 4 micron, 45 degree twisted nematic cell

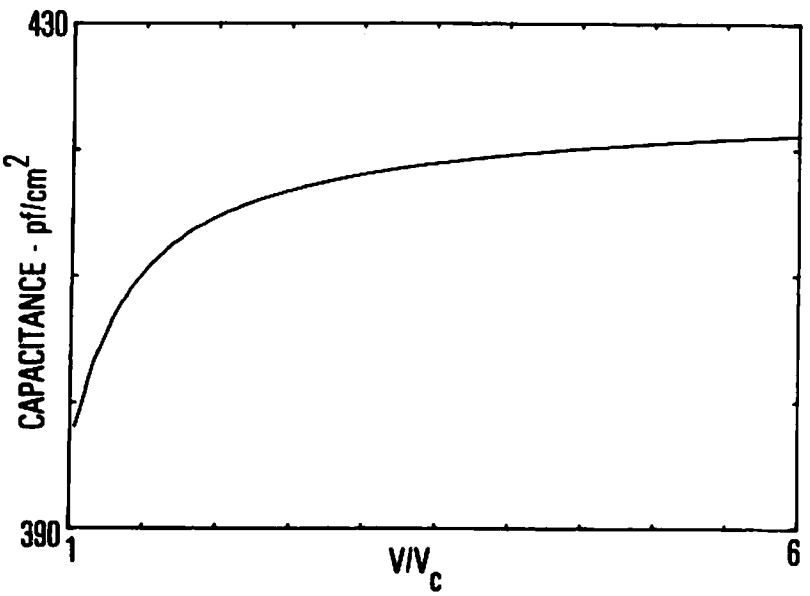

Figure 2-14 Cell capacitance vs. normalized voltage for an 11 micron uniform perpendicular cell

it is seen that the effective dielectric constant is the same as that given in Eq. (2.92). Repeating Eq. (2.34) which relates the tilt angle ϕ with location in the cell and applied field,

$$\tan\frac{\phi}{2} = e^{-z/\xi} \quad . \tag{2.93}$$

From this is obtained

$$\sin^2\phi = e^{-2z/\xi}(1+2\cos\phi+\cos^2\phi) \quad . \tag{2.94}$$

Through further trigonometric reduction,

$$\cos^2\phi = \tanh^2(z/\xi) \quad , \tag{2.95}$$

and from Eq. (2.92), we obtain

$$\varepsilon_e = \varepsilon_1+(\varepsilon_{11}-\varepsilon_1)\cos^2\phi \quad . \tag{2.96}$$

Combining Eqs. (2.95) and (2.96), then

$$\varepsilon_e = \varepsilon_1+(\varepsilon_{11}-\varepsilon_1)\tanh^2(z/\xi) \quad . \tag{2.97}$$

Thus the capacitance of any layer at position Z in the cell is given by

$$C(z) = \frac{\varepsilon_0\varepsilon_e(z)A}{dz} \tag{2.98}$$

From the symmetry of the structure, the total cell capacitance is then given by

$$C_T = \frac{1}{2} \; \frac{1}{\int_0^{d/2}\frac{dz}{\varepsilon_0 A\varepsilon_e(z)}} \tag{2.99}$$

from which

$$\frac{C_T}{A} = \frac{\varepsilon_0/2}{\int_0^{d/2} \frac{dz}{\varepsilon_1+(\varepsilon_{11}-\varepsilon_1)\tanh^2(z/\xi)}} \qquad (2.100)$$

Equation (2.100) reduces to

$$\frac{C_T}{A} = \frac{\varepsilon_0}{d/\varepsilon_{11}+\frac{2\xi\sqrt{\varepsilon_1(\varepsilon_{11}-\varepsilon_1)}}{\varepsilon_{11}\varepsilon_1}\text{arctg}\left[\frac{\sqrt{\varepsilon_1}(\varepsilon_{11}-\varepsilon_1)}{\varepsilon_1}\tanh(d/2\xi)\right]} \qquad (2.101)$$

With $V=Ed$ and $V_c = 2(K/\varepsilon_a)^{\frac{1}{2}}$, and using the definition of ξ given in Eq. (2.26), Eq. (2.100) becomes

$$\frac{C_T}{A} = \frac{\varepsilon_0}{d/\varepsilon_{11}\left\{1+\frac{V_c}{V}\sqrt{\frac{\varepsilon_{11}-\varepsilon_1}{\varepsilon_1}}\,\text{arctg}\left[\sqrt{\frac{\varepsilon_{11}-\varepsilon_1}{\varepsilon_1}}\tanh\left(\frac{V}{V_c}\right)\right]\right\}} \qquad (2.102)$$

For $\varepsilon_{11}=16$ and $\varepsilon_1=5$ [33], Fig. 2-15 shows the cell capacitance per unit area vs. normalized voltage for an 11 micron thick parallel aligned cell.

2.6 Photoactivated Liquid Crystal Light Valves

To characterize the theoretical performance of the light activated liquid crystal light valves reguires not only the results of the preceding sections but also a theoretical model for the photosensor response and interaction with the liquid crystal cell. In the most general terms, the photosensor acts as a light dependent impedance which locally switches the applied bias voltage onto the liquid crystal cell as a function of input light

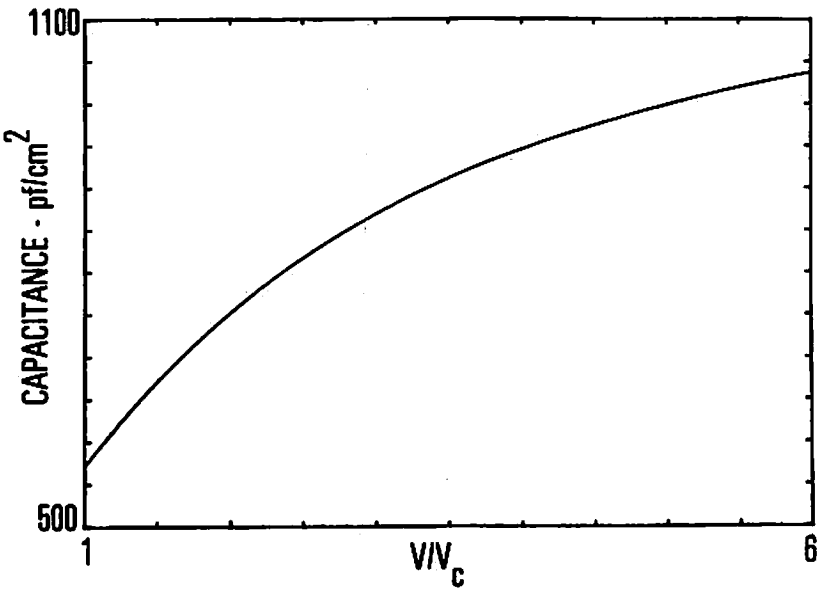

Figure 2-15 Cell capacitance vs. normalized voltage for an 11 micron uniform parallel cell

intensity. The operation of the CdS/CdTe heterojunction photosensor to be considered here is significantly more complex than a simple impedance change as a function of light intensity. The amount of bias voltage switched onto the liquid crystal layer depends not only on the light intensity but also on bias voltage amplitude and frequency, photosensor temperature, and load impedance. While a precise description of the photosensor operation has not yet been formulated and is beyond the scope of this paper to attempt, a number of simplifying assumptions may be made to obtain at least a first order approximation of the actual photosensor response. Experimental verification has shown these approximations sufficiently accurate to obtain reasonable predictions of light valve behavior under varying input intensity and bias voltage conditions [29-30].

An equivalent circuit for the photoactivated light valve is shown in Fig. 2-16a. From the figure, Z_{PC} is the impedance represented by the photosensor layer, Z_M is the series impedance of the dielectric mirror and inert insulating layers, and Z_{LC} is the impedance of the liquid crystal cell. If V_S is the rms value of the applied bias voltage, then from the figure the voltage V_{LC} developed across the liquid crystal cell is given by

$$V_{LC} = \frac{Z_{LC}\, V_S}{Z_T + Z_{LC}} \qquad (2.103)$$

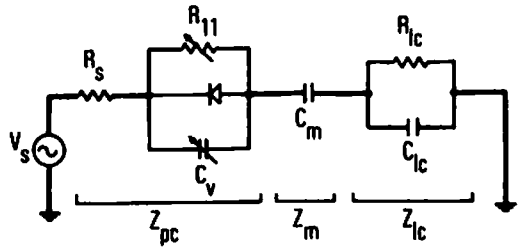

(a)

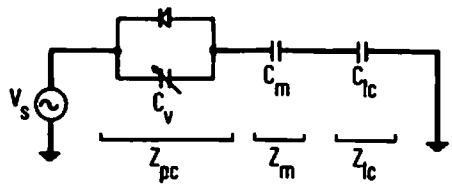

(b)

Figure 2-16 Equivalent circuit of photoactivated light valve resolution element
(a) Complete circuit
(b) Simplified circuit

where Z_T is simply the sum of the impedances Z_{PS} and Z_M. The impedance Z_{LC} was derived in section 2.5 and is in general a function of V_{LC}. The impedance Z_M may be represented by a pure capacitance as the mirror and insulating layers are simply stacked dielectric films. The impedance is readily calculated from the dielectric constants and known thicknesses of each of the layers. The impedance of any layer is given by

$$Z = \frac{1}{\omega C} \tag{2.104}$$

where ω is the frequency of V_S in radians per second and C is the capacitance of the thin film. C is given by

$$C = \frac{A\varepsilon}{d} \tag{2.105}$$

with A the area of the film, d its thickness, and ε the dielectric constant of the film material.

The impedance Z_{PS} of the photosensor is somewhat more complicated and the model to be developed is that of Fraas et al [29-30] for a CdS/CdTe heterojunction photosensor. Referring to Fig. 2-16a, R_S is the series resistivity of the nondepleted region of the photosensor diode, R_{11} is the residual resistivity of the depleted region, and C_V is the light dependent capacitance of the back biased photosensor diode. A simplification arises by assuming

$$R_S << \frac{1}{\omega C_V} \tag{2.106}$$

$$R_{11} >> \frac{1}{\omega C_V} \tag{2.107}$$

The validity of these assumptions has been shown reasonable for first order approximations by experimental comparison [29-30]. Z_{PS} then represents the impedance of the charge storage diode shown in the simplified diagram of Fig. 2-16b. If Q represents the total charge on the diode, then the characteristic Q vs. V curves for the structure are represented by [29-30]

$$V = \frac{Q^2}{2\varepsilon\bar{n}} \qquad Q \leq Q_\delta \tag{2.108}$$

$$V = \frac{\bar{n}\delta^2}{2\varepsilon} + \frac{(Q-\bar{n}\delta)D}{\varepsilon} \qquad Q \geq Q_\delta \tag{2.109}$$

where V is the instantaneous back bias voltage across the diode, ε is the CdS dielectric constant, D is the thickness of the CdS layer, and δ is the thickness of the high shallow trap density, high absorptive CdS region. The parameter $\bar{n}$ is the light intensity dependent electron population density in the high absorptive δ region and for low light levels is given by

$$\bar{n} = K\sqrt{I} \tag{2.110}$$

where I is the incident light intensity and K is a sensitivity coefficient whose value depends on temperature, frequency, and the physical constants of the CdS film. The threshold parameter Q_δ is the total charge in donor states

and is given by

$$Q_\delta = \bar{n}\delta \qquad (2.111)$$

The model described by Eqs. (2.108)-(2.110) assumes that all of the incident light is absorbed in the highly absorptive δ region. This assumption is reasonable for first order approximations but does lead to slight discontinuities in photosensor response predictions. The effect of this discontinuity will be pointed out where applicable both in the photosensor response prediction as well as in the predictions for overall light valve behavior. Using Eqs. (2.108) and (2.109), representative Q vs. V curves for a 16 micron thick CdS layer are shown in Fig. 2-17 as a function of $\bar{n}$. The effect of the δ region total absorption assumption is readily seen in the figure where the quadratic portion of the curves join the linear section. In reality the absorption extends beyond the δ region. If this were considered, it would give rise to a smoother transition of the two sections of the curves in Fig. 2-17.

For a sinusoidally varying input bias voltage, if $2V_p$ equals the maximum inverse voltage across the diode, then the instantaneous back bias voltage will be given by

$$V = V_p(1+\cos\omega t) \ . \qquad (2.112)$$

The threshold voltage governing selection of either

Eq. (2.108) or Eq. (2.109) is given by setting $Q=Q_\delta$ in either equation. Thus from Eq. (2.108)

$$V_T = \frac{Q_\delta^2}{2\varepsilon\bar{n}} = \frac{\bar{n}\delta^2}{2\varepsilon} \quad . \tag{2.113}$$

For $V \leq V_T$, the instantaneous current in the photosensor is given by

$$i_1 = \frac{dQ}{dt} = \frac{d}{dt}\sqrt{2\varepsilon\bar{n}V} + \sqrt{2\varepsilon\bar{n}V_p}\,\frac{d}{dt}(1+\cos\omega t)^{\frac{1}{2}} \tag{2.114}$$

$$i_1 = -\omega\sqrt{\varepsilon\bar{n}V_p}\,\sin\frac{\omega t}{2} \quad . \tag{2.115}$$

For $V \geq V_T$, then from Eq. (2.116)

$$Q = \frac{\varepsilon V}{D} - \frac{\bar{n}\delta^2}{2D} + \bar{n}\delta \tag{2.109}$$

$$i_2 = \frac{dQ}{dt} = \frac{\varepsilon V_p}{D}\,\frac{d}{dt}(1+\cos\omega t) \tag{2.117}$$

$$i_2 = \frac{-\omega\varepsilon V_p}{D}\,\sin\omega t \quad . \tag{2.118}$$

The rms current I through the photosensor is given by

$$I^2 = \frac{1}{T}\int_0^T i^2 dt \tag{2.119}$$

where T is the period of one cycle, i.e., $T=\frac{2\pi}{\omega}$. Now if $2V_p \leq V_T$, i.e.,

$$V_p \leq \frac{\bar{n}\delta^2}{4\varepsilon} \tag{2.120}$$

then Eq. (2.115) alone specifies the instantaneous current. Thus the rms current is given by

$$I_1^2 = \frac{\omega}{2\pi}\int_0^{2\pi/\omega} \omega^2 \varepsilon \bar{n} V_p \sin^2 \frac{\omega t}{2} dt \qquad (2.121)$$

$$I_1^2 = \frac{\omega^2 \varepsilon \bar{n} V_p}{2} \qquad (2.122)$$

$$I_1 = \frac{\omega}{\sqrt{2}}\sqrt{\varepsilon \bar{n} V_p} \qquad (2.123)$$

If $2V_p > V_T$ the situation is somewhat more complicated with the instantaneous current being given by Eq. (2.115) for $V \leq V_T$ and then by Eq. (2.118) for $V > V_T$. From Eq. (2.120), the point in time during a single cycle at which threshold is reached is given by

$$V_T = \frac{\bar{n}\delta^2}{2\varepsilon} = V_p(1+\cos\omega t_c) \qquad (2.124)$$

from which

$$t_c = \frac{1}{\omega}\cos^{-1}\left(\frac{\bar{n}\delta^2}{2\varepsilon V_p} - 1\right) \quad . \qquad (2.125)$$

From Fig. 2-18, which is a plot of back bias voltage vs. time for one period, it is seen that for $0 \leq t \leq t_c$ and $\frac{2\pi}{\omega} - t_c \leq t \leq \frac{2\pi}{\omega}$, Eq. (2.118) will specify the instantaneous current. Otherwise for $t_c \leq t \leq \frac{2\pi}{\omega} - t_c$, Eq. (2.115) will specify the instantaneous current. Thus the rms current will be given by

$$I_2^2 = \frac{\omega}{2\pi}\left[\int_0^{t_c} i_2^2 dt + \int_{t_c}^{\frac{2\pi}{\omega}-t_c} i_1^2 dt + \int_{\frac{2\pi}{\omega}-t_c}^{\frac{2\pi}{\omega}} i_2^2 dt\right] \qquad (2.126)$$

$$I_2^2 = \frac{\omega}{2\pi}\left[2\int_0^{t_c} i_2^2 dt + 2\int_0^{\pi/\omega} i_1^2 dt\right] \quad . \qquad (2.127)$$

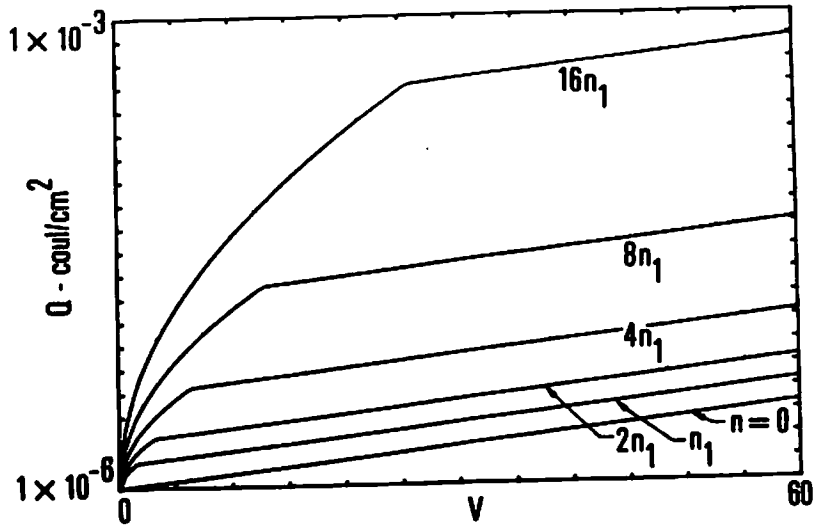

Figure 2-17 Q vs. V curves for a 16 micron CdS/CdTe photosensor

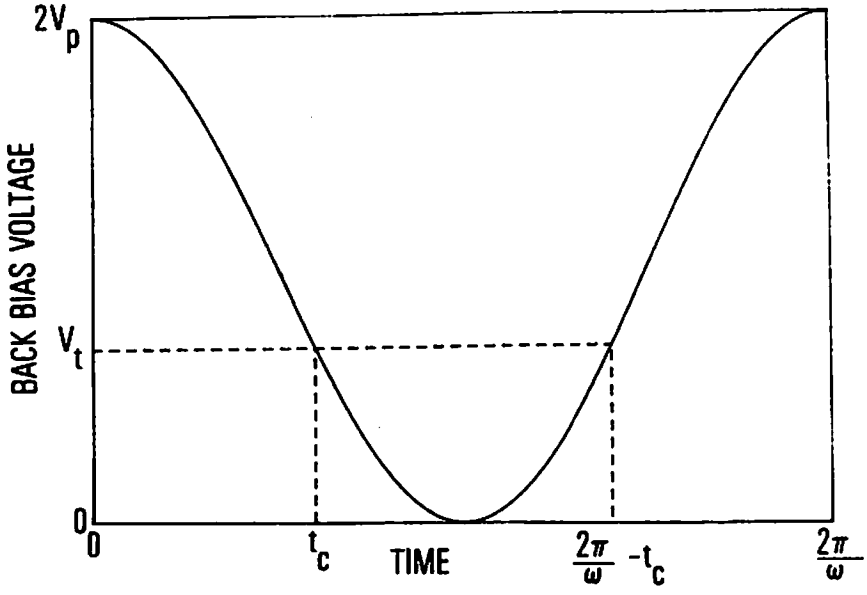

Figure 2-18 Photodiode back bias voltage during one complete cycle

Letting $\beta=\frac{\bar{n}\delta^2}{2\varepsilon V_p} - 1$, then $t_c = \frac{1}{\omega}\cos^{-1}\beta$ and Eq. (2.127) becomes

$$I_2^2 = \frac{\omega}{2\pi}\left\{2\int_0^{\frac{1}{\omega}\cos^{-1}\beta} \frac{\omega^2\varepsilon^2 V_p^2}{D^2}\sin^2\omega t\,dt + 2\int_{\frac{1}{\omega}\cos^{-1}\beta}^{\pi/\omega} \omega^2\varepsilon\bar{n}V_p\sin^2\frac{\omega t}{2}dt\right\} \quad (2.128)$$

$$I_2^2 = \frac{\omega}{\pi}\left\{\frac{\omega\varepsilon^2 V_p^2}{D^2}\left[\frac{\cos^{-1}\beta}{2} - \frac{1}{4}\sin(2\cos^{-1}\beta)\right] + \omega\varepsilon\bar{n}V_p\left[\frac{\pi}{2} - \frac{\cos^{-1}\beta}{2} + \frac{1}{2}\sin(\cos^{-1}\beta)\right]\right\}. \quad (2.129)$$

Since $\sin(\cos^{-1}\beta) = (1-\beta^2)^{\frac{1}{2}}$, then Eq. (2.129) becomes

$$I_2^2 = \frac{\omega}{\pi}\left\{\frac{\omega\varepsilon^2 V_p^2}{D^2}\left[\frac{\cos^{-1}\beta}{2} - \frac{1}{2}(1-\beta^2)^{\frac{1}{2}}\beta\right] + \omega\varepsilon\bar{n}V_p\left[\frac{\pi}{2} - \frac{\cos^{-1}\beta}{2} + \frac{1}{2}(1-\beta^2)^{\frac{1}{2}}\right]\right\} \quad (2.130)$$

$$I_2^2 = \frac{\omega^2\varepsilon^2 V_p^2}{2D^2\pi}\left\{\cos^{-1}\beta - \beta(1-\beta^2)^{\frac{1}{2}} + \frac{\bar{n}D^2}{\varepsilon V_p}\left[\pi - \cos^{-1}\beta + (1-\beta^2)^{\frac{1}{2}}\right]\right\} \quad (2.131)$$

or

$$I_2 = \frac{\omega\varepsilon V_p}{D\sqrt{2\pi}}\left\{\cos^{-1}\beta - \beta(1-\beta^2)^{\frac{1}{2}} + \frac{\bar{n}D^2}{\varepsilon V_p}\left[\pi - \cos^{-1}\beta + (1-\beta^2)^{\frac{1}{2}}\right]\right\}^{\frac{1}{2}} . \quad (2.132)$$

Equations (2.123) and (2.132) then relate the rms photosensor current to the incident light intensity and back bias photosensor voltage. Figure 2-19 shows a typical plot of I/ω vs. photosensor voltage. Further, with $Z_{PS}=V_{PS}/I$, then Fig. 2-20 relates ωZ_{PS} to photosensor voltage as a function of $\bar{n}$ for a typical CdS/CdTe structure. The combination of this data and the cell impedance data found in section 2.5 uniquely relates the

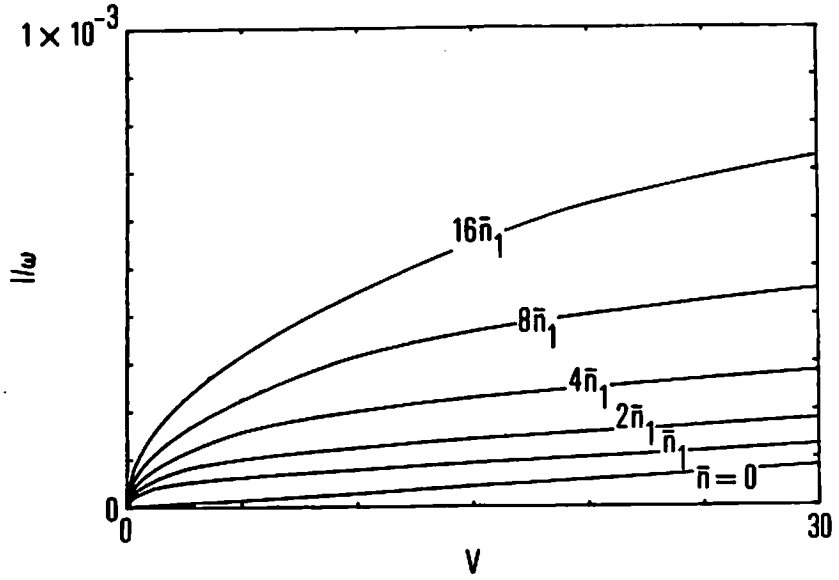

Figure 2-19 Normalized photosensor current vs. applied voltage

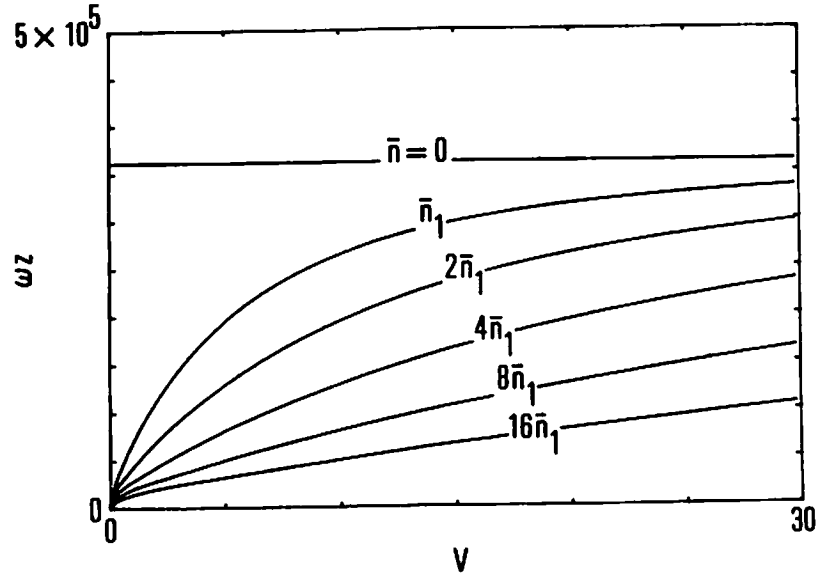

Figure 2-20 Photosensor impedance vs. applied voltage

bias voltage and incident intensity to the voltage across the liquid crystal layer. Combined with the retardation information found in sections 2.2 to 2.4, the overall photoactivated light valve performance may be determined. Using the theory developed in this chapter, performance predictions on specific devices will be made in Chapter 4.

CHAPTER 3

NONLINEAR IMAGE PROCESSOR

This chapter will present a generalized method of obtaining nonlinear transformations on two dimensional images. The chapter will begin with a general description and theory of obtaining such transformations using polarization sensitive optical elements. An idealized transforming system will be considered first to provide optimal performance criteria. A method will then be presented for realizing the ideal system using real optical elements and multiple liquid crystal light valves. The theoretical light valve performance models developed in Chapter 2 will be utilized to obtain predicted nonlinear transformation system performance. Actual system performance predictions using real light valve data will be deferred to Chapter 5.

3.1 Generalized Nonlinear Transformation System

The nonlinear transformation system described here essentially performs a mapping of intensity variations of a two dimensional input image into two dimensional constant

magnitude but temporally separated light impulses. This constitutes a scanned level slice operation. The constant magnitude impulses are then weighted as a function of time with a temporal weighting function formulated to give the desired nonlinear transformation. The weighted impulses are then integrated over an appropriate time interval resulting in a two dimensional nonlinear transformed output image. The operation is shown schematically in Fig. 3-1 for a simple three intensity level, two dimensional input image. The intensity to time converter maps input intensities over the range of 0 to I_{MAX} into the time interval [0,T]. Thus for a linear mapping the output plane for the intensity to time converter will remain dark during the time interval $0 < t < t_1$ since there exists no intensity components in the input image with values between I=0 and $I=I_1$. At time t_1 corresponding to the input intensity I_1, the output plane will have a constant intensity response over all portions of the plane corresponding to that part of the input image for which $I=I_1$. Similar output responses occur at times t_2 and t_3 as shown in the figure. For all other times $0 < t < T$; $t \neq t_1, t_2, t_3$ the output intensity remains at zero. Representing the idealized light impulses by the Dirac delta function $\delta(x,y,t)$, then at the output plane of the intensity-to-time converter the intensity distribution is given by

$$I_T(x,y,t) = I_{MAX}\delta\left(t-\frac{I(x,y)}{I_{MAX}}T\right) \qquad (3.1)$$

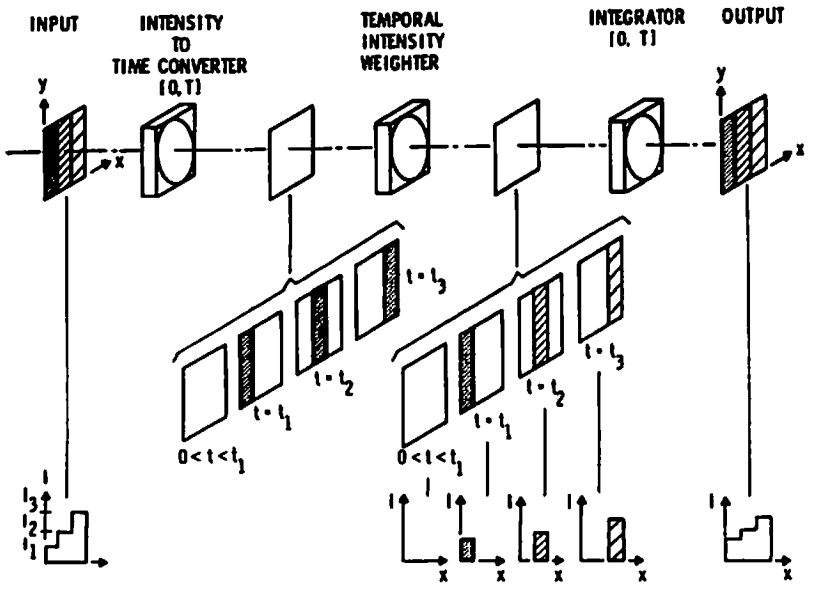

Figure 3-1 Operation of nonlinear image processor

where $0 \leq t \leq T$ and $0 \leq I(x,y) \leq I_{MAX}$.

Referring again to Fig. 3-1, the temporal intensity weighter is simply an electrooptic attenuator which weights the constant intensity, time sequential impulses emerging from the intensity-to-time converter in the desired nonlinear manner. The nonlinearity is introduced by applying a nonlinearly shaped voltage waveform to the temporal intensity weighter during the time interval [0,T]. Thus if f(t) represents the desired time dependent nonlinear attenuation function present in the intensity weighter during the interval [0,T], then the intensity distribution at the output of the weighter is given by

$$I_W(x,y,t) = f(t) I_T(x,y,t) \quad . \tag{3.2}$$

The final operation depicted in Fig. 3-1 is that performed by the temporal integrator. The time sequential weighted impulses $I_W(x,y,t)$ are summed over the time interval [0,T] thus removing the time dependence. The result is that at time t=T a nonlinearly transformed input image will be present at the output of the integrator, i.e.,

$$I_0(x,y) = \int_0^T f(t) I_{MAX} \delta\left(t - \frac{I(x,y)}{I_{MAX}} T\right) dt \tag{3.3}$$

$$I_0(x,y) = I_{MAX} f\left[\frac{I(x,y)T}{I_{MAX}}\right] \quad . \tag{3.4}$$

Equation (3.4) defines the system transfer function. Thus

for the simple case of

$$f(t) = \frac{t}{T} \tag{3.5}$$

then

$$I_0(x,y) = I_{MAX}\left[\frac{I(x,y)}{I_{MAX}}\right] = I(x,y) \tag{3.6}$$

which is simply a one-to-one linear transformation from input to output. It should be noted that one of the key features of this type of system is the ability to arbitrarily and in real time change the form of the nonlinear transformation. The nonlinearity introduced through f(t) above is in general related to the voltage applied to the temporal intensity weighter by the attenuation transfer function ϕ_A of the electrooptic attenuator, i.e.,

$$f(t) = \phi_A V(t) \quad . \tag{3.7}$$

As will be shown in the following section, a real time implementation of this system using multiple liquid crystal light valves provides for real time control of v(t) via a microprocessor or minicomputer.

3.2 Liquid Crystal Implementation

The ideal nonlinear processing system described in the previous section can be approximated using the polarizing properties of liquid crystal light valves. To demonstrate

this, the system will be divided into five distinct functional areas, four of which are implemented with liquid crystal light valves. The functions to be considered are 1) an intensity notch function, 2) a contrast inverter, 3) an intensity threshold operation, 4) an intensity weighter, and 5) the integration function. The first three of these functions comprise the intensity-to-time converter. Together they perform the mapping of the input intensity variations into the time sequential constant amplitude light impulses. For reasons that will become apparent, the operation is implemented by mapping the two dimensional input variations into time sequential intensity notches (function one), contrast inverting the notch responses to obtain time sequential intensity level slices (function two), and then thresholding the relatively broad level slices to obtain the desired narrow range constant magnitude light impulses. Functions four and five directly implement the temporal weighter and integration operations described in the previous section.

3.2.1 Intensity Notch Function

To demonstrate implementation of the notch function using light valves, consider the reflection mode light valve system shown in Fig. 3-2. The read illumination enters from the right where it is polarized by polarizer P_1. The angle of polarization is set such that it subtends

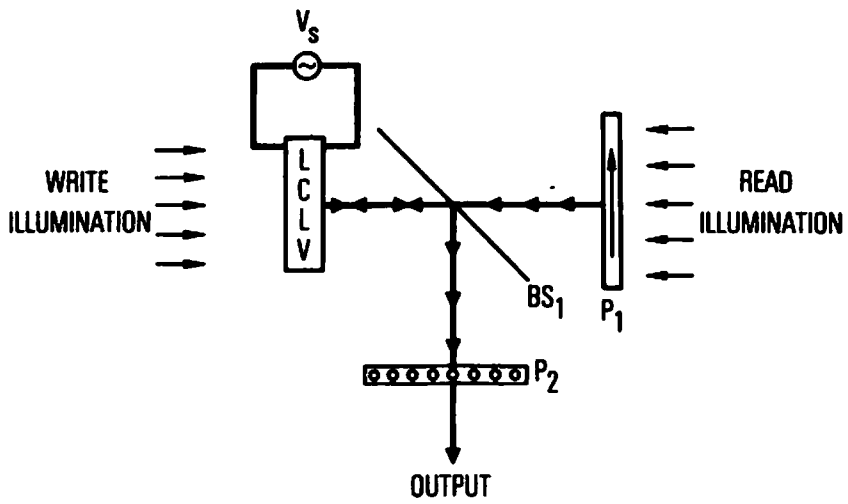

Figure 3-2 Intensity notch generating subsystem

an angle of 45 degrees to the liquid crystal molecular axis. The light passes through P_1 directly through beam splitter BS_1 and enters the light valve structure. The light then passes through the liquid crystal layer, is reflected from the internal dielectric mirror in the device and passes again through the liquid crystal layer before emerging toward BS_1. As the light traverses the liquid crystal layer, the two components of the incident light in the X and Y directions undergo a differential phase change determined by the phase retardation of the liquid crystal cell. From the light valve, the light is then reflected off of beamsplitter BS_1 where it then passes through polarization analyzer P_2 whose polarization angle is set at 90 degrees to polarizer P_1. The resultant intensity of the light emerging from P_2 can be related to the phase retardation imposed by the liquid crystal device through the use of the Jones formalism.

If the read light is a plane monochromatic wave with intensity I_0, then with P_1 oriented at 45 degrees to the X-Y axis of the liquid crystal molecules, the light incident on the input face of the light valve is described by the Jones vector

$$\bar{E}_i = \frac{E_0}{\sqrt{2}} \begin{bmatrix} 1 \\ 1 \end{bmatrix} \tag{3.8}$$

signifying equal amplitude X and Y field components. $E_0=\sqrt{I_0}$ is the magnitude of the light incident on P_1. The

liquid crystal cell imposes a phase retardation on the two components and can be described by a matrix operator

$$\underline{L} = \begin{bmatrix} e^{j(\delta/2)} & 0 \\ 0 & e^{-j(\delta/2)} \end{bmatrix} \tag{3.9}$$

where δ is the phase retardation after a single pass through the liquid crystal cell. Since the device is being operated in reflection mode, the light passes through the liquid crystal layer twice giving an overall phase retardation of 2δ. Thus to describe the reflection mode device, Eq. (3.9) becomes

$$\underline{L'} = \begin{bmatrix} e^{j\delta} & 0 \\ 0 & e^{-j\delta} \end{bmatrix} . \tag{3.10}$$

From Eqs. (3.8) and (3.10) the light emerging from the light valve toward BS is then described by

$$\bar{E}_{OUT} = \underline{L'}\bar{E}_i = \frac{E_0}{\sqrt{2}} \begin{bmatrix} e^{j\delta} & 0 \\ 0 & e^{-j\delta} \end{bmatrix} \begin{bmatrix} 1 \\ 1 \end{bmatrix} \tag{3.11}$$

$$\bar{E}_{OUT} = \frac{E_0}{\sqrt{2}} \begin{bmatrix} e^{j\delta} \\ e^{-j\delta} \end{bmatrix} . \tag{3.12}$$

The operator matrix for a polarization analyzer P_2 oriented at an angle α to the X axis is given by

$$\underline{P}(\alpha) = \begin{bmatrix} \cos^2\alpha & \sin\alpha\cos\alpha \\ \sin\alpha\cos\alpha & \sin^2\alpha \end{bmatrix} . \tag{3.13}$$

For the present system α is $3\pi/4$ radians (90 degrees from polarizer P_1). Thus the operator is given by

$$\underline{\underline{P}} = \frac{1}{2}\begin{bmatrix} 1 & -1 \\ -1 & 1 \end{bmatrix} . \qquad (3.14)$$

Applying Eq. (3.14) to Eq. (3.12) yields the resultant field at the output of polarizer P_2.

$$\bar{E}_R = \underline{\underline{P}}\,\bar{E}_{OUT} \qquad (3.15)$$

$$\bar{E}_R = \frac{E_0}{2\sqrt{2}}\begin{bmatrix} e^{j\delta}-e^{-j\delta} \\ -e^{j\delta}+e^{-j\delta} \end{bmatrix} \qquad (3.16)$$

$$\bar{E}_R = \frac{jE_0}{\sqrt{2}}\begin{bmatrix} \sin\delta \\ -\sin\delta \end{bmatrix} . \qquad (3.17)$$

Finally, the resultant intensity is given by

$$I_R = \bar{E}_R\bar{E}_R^* = I_0\sin^2\delta \qquad (3.18)$$

where $I_0=E_0^2$.

For a specific example of relationship (3.18), consider the phase retardation vs. cell voltage of a perpendicularly aligned cell as given in Fig. 2-5. For a 2 micron cell with λ=514.5 nm, and critical voltage V_c=1.5, then with the cell aligned as in Fig. 3-2 the resultant log intensity vs. cell voltage is shown in Figs. 3-3a and 3-3b. As shown in Fig. 3-3b, a sharp null occurs at a cell voltage of 4.09 volts. If the liquid crystal cell is mated to a photoconductor, the cell voltage then becomes a function both of the incident write intensity on the photoconductor and the bias voltage applied to the overall

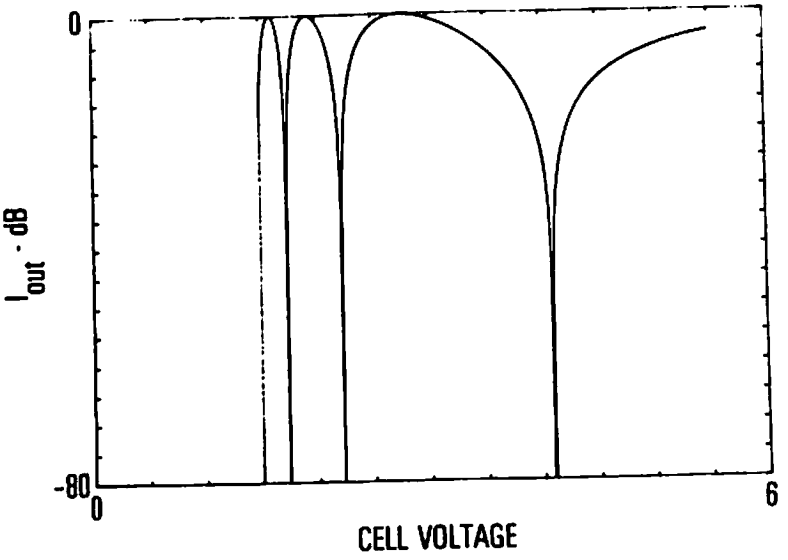

(a)

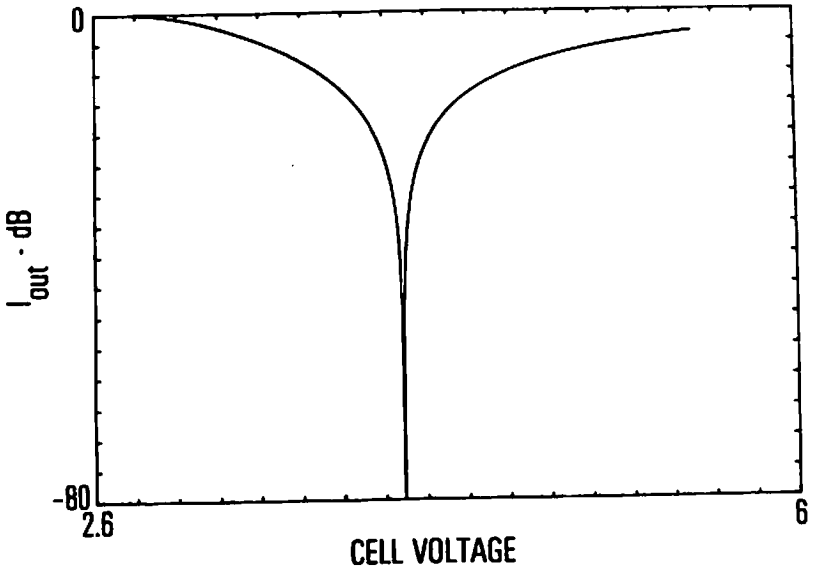

(b)

Figure 3-3 Notch generator output intensity vs. applied cell voltage
(a) Full sweep
(b) Limited sweep

structure. For a given write intensity, the photoconductor will switch a fixed ratio of the bias voltage onto the liquid crystal layer. Thus if the bias voltage is swept over appropriate limits, the fraction of the bias voltage switched to the liquid crystal layer will become equal to the null voltage of Fig. 3-3b at some bias voltage V_1. This will result in minimal intensity transmission of the output read light. For any other input write intensity, a unique fraction of the bias voltage is transferred to the liquid crystal layer. Thus the critical null voltage of Fig. 3-3b will be reached at different points during the sweep of the bias voltage. If the bias voltage is swept linearly with time, this then establishes a one-to-one mapping of intensity notch with time.

To illustrate the process, consider the above 2 micron perpendicularly aligned liquid crystal cell mated to a 16 micron thick CdS/CdTe photosensor. Using typical photosensor parameters [29-30], δ=2.67 microns, $\epsilon=4.43\times10^{-11}$, then Fig. 3-4 shows the theoretical light valve response as a function of bias voltage for three input intensities separated by 3 db. As seen in the figure, for a given input intensity multiple nulls are obtained if the bias voltage is swept over the full range of 0 to 20 volts. Since a one-to-one mapping of intensity null vs. bias voltage is desired, this requires that the bias voltage be swept only over a range sufficient to

ensure a single intensity null. In Fig. 3-4 an appropriate range would be from 6 to 20 volts which would include only the third null of the liquid crystal response. It should be noted at this point that the multiple nulls restrict the dynamic range of the intensity notch function. As the input intensity increases, the voltage at which the third null in the response occurs decreases toward zero volts. At some particular input intensity level the third null voltage will coincide with the voltage required to obtain the second null in the response for zero input intensity. The requirement for a one-to-one mapping then dictates input intensities less than this maximum value. For the theoretical device of Fig. 3-4 and also for actual devices, the dynamic range available while maintaining a one-to-one mapping is in excess of 30 db. Figure 3-5 shows the device responses of Fig. 3-4 with the sweep voltage constrained to 6 to 20 volts.

3.2.2 Contrast Inverter

The intensity-to-time converter in the overall processing system requires constant magnitude light impulses as its output rather than the intensity nulls given by the intensity notch generator. Through contrast inversion the nulls obtained from the notch generator can be converted into the desired impulses or light peaks. Contrast inversion is easily implemented using the

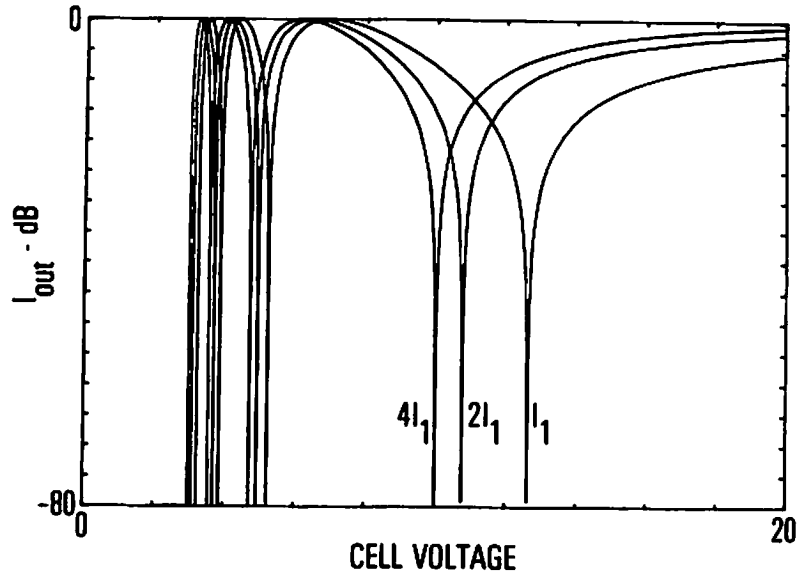

Figure 3-4 Notch generator output intensity vs. swept bias voltage for three separate input intensities

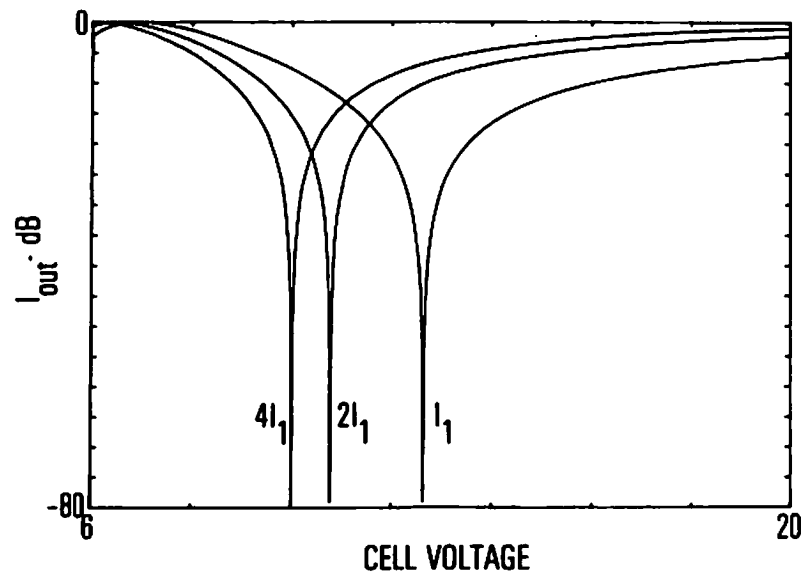

Figure 3-5 Figure 3-4 responses for constrained bias sweep voltage

polarization properties of liquid crystal cells. The function is best implemented with the reflection mode twisted nematic type light valve with the polarizer/analyzer pair oriented in the same direction. It has been shown [28] that a cell with an overall molecular twist of 45 degrees provides the maximum on-off transmission ratio. For this reason the 45 degree twist cell will be used both for the contrast inverter and the threshold device to be considered in the next section.

In section 2.4 the theory was developed for the transmission characteristics of a twisted nematic cell. The results of applying the theory to a reflection mode, 2 micron, 45 degree twist cell between crossed polarizer/analyzer were shown in Fig. 2-11. Applying the theory to a 4 micron, 45 degree cell placed between a polarizer and analyzer oriented in the same direction, the transmission vs. normalized cell voltage is shown in Fig. 3-6. If this cell is mated to a CdS/CdTe photosensor, the data of Fig. 3-6 together with the results of sections 2.5 and 2.6 can be used to determine the input/output intensity transfer characteristics of the light valve. The assumptions to be made for the photosensor are the same as those made for the intensity notch generator, i.e. CdS thickness equal to 16 microns, δ=2.6667 microns, and $\varepsilon=4.4275\times10^{-11}$. If it is further assumed that the total capacitance per unit area represented by the internal

dielectric mirror is 2530 pf/cm^2 and that the liquid crystals have dielectric constants parallel to and perpendicular to the molecular axis of 16 and 5 respectively, then Fig. 3-7 shows the intensity transfer function of the device for an applied bias voltage of 10 volts rms. The liquid crystal threshold voltage was assumed to be 1.05 volts rms, a value typical for the liquid crystal mixture commonly used in twist cells. In the figure, the ordinate is normalized intensity transmission for 514.5 nm read illumination. The abscissa is in relative db of input intensity, the absolute value of which is dependent on the sensitivity coefficient K in Eq. (2.110). As seen in Fig. 3-7 the transfer function has the necessary slope to provide contrast inversion, i.e. smaller input intensity results in greater intensity transmission at the output of the device.

If one of the notch responses shown in Fig. 3-4 is used as the input to the above light valve, the effects of the contrast inversion can be seen in Fig. 3-8. To obtain the results shown in the figure, the input to the contrast inverter, while following on a db basis the transmission characteristic of the notch generator, was adjusted such that the -30 db point on the null curve corresponded to the -46 db input point on the contrast inverter transfer curve. Such scaling is readily accomplished in an actual system by adjusting the intensity of the read illumination to the

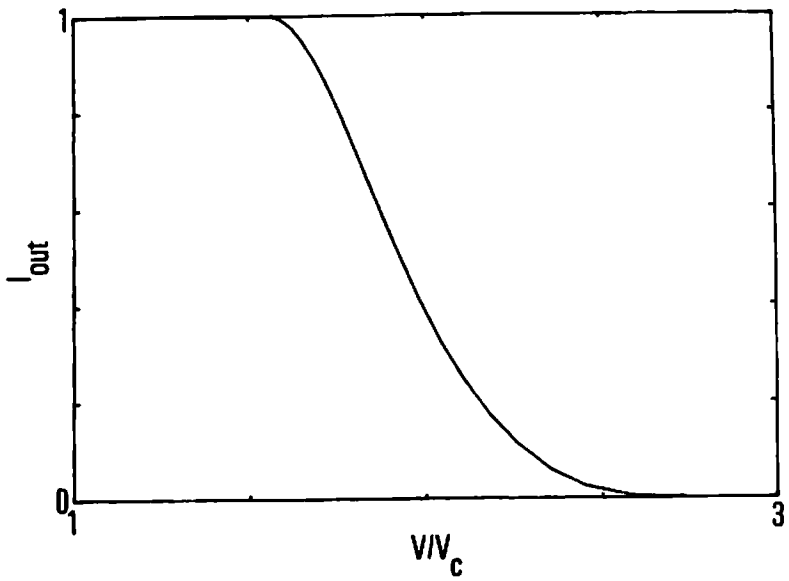

Figure 3-6 Transmission vs. normalized cell voltage for a 4 micron, 45 degree twisted nematic cell with parallel polarizer/analyzer

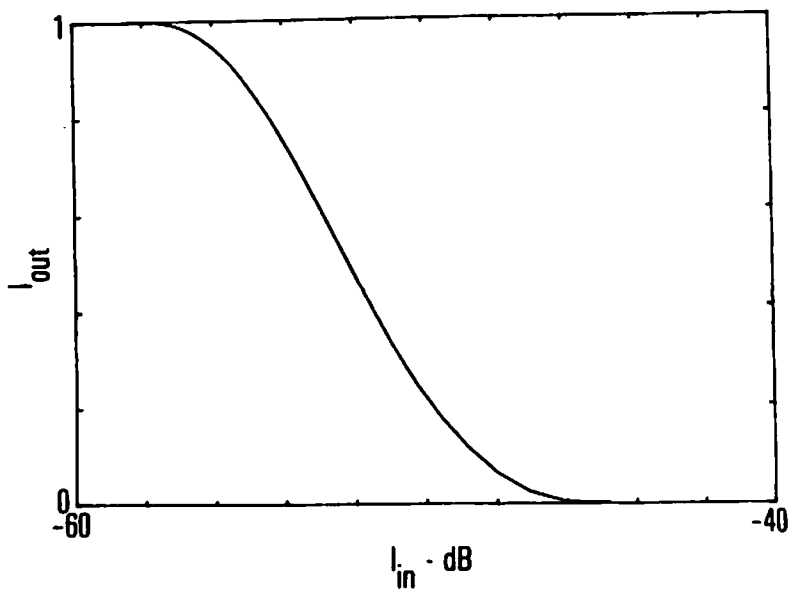

Figure 3-7 Intensity transfer function of contrast inverter

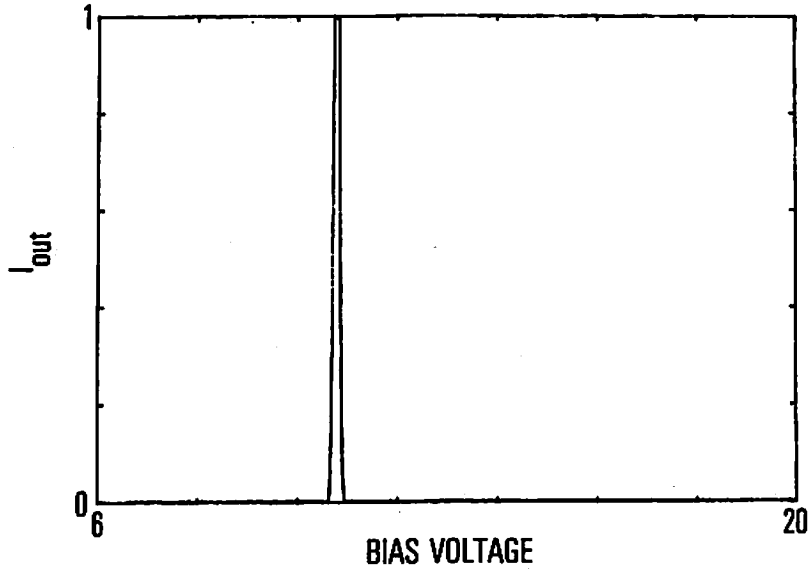

Figure 3-8 Contrast inverter response to intensity notch input

notch generator. In the present discussion, this illumination modified by the transfer characteristics of the notch generator becomes the input write illumination to the contrast inverter. Figure 3-8 points out an added benefit of using the light valve for contrast inversion. Due to the limiting characteristics of the inverter transfer curve, the device also performs a thresholding operation on the input intensity response. Thus the relatively broad input null response results in a significantly more narrow output response as a function of notch generator bias sweep voltage. The output then more closely resembles the ideal delta function type response desired for the nonlinear processing system's intensity to time converter. Clearly, the more narrow the light impulses, the greater will be the resolution of the processing system. Achieving higher resolution through a further thresholding operation is the subject of the next section.

3.2.3 Threshold Function

As mentioned in the previous section, in order to obtain the highest processing system resolution, the intensity-to-time converter should map input intensities into temporally separated delta function-like light impulses. While the thresholding characteristics of the contrast inverter significantly reduces the width of the

intensity nulls from the notch generator, further narrowing of the light impulses can be attained through subsequent thresholding. The same type of light valve used for contrast inversion, i.e. a 45 degree twisted nematic, can be used for the thresholding operation. However, to use the device in a threshold mode it is placed between a crossed polarizer/analyzer pair. In this configuration, the device will not transmit any read illumination to the remainder of the processing system with low input illumination. As the input illumination is increased, a critical point is reached where the device is "switched on" and a portion of the read illumination is allowed to pass on to the remainder of the system. The percentage of read illumination transferred through the device as a function of input intensity level is again determined by the light valve transfer function.

To calculate the transfer function, identical device parameters as used in section 3.2.2 were used in conjunction with the theory developed in Chapter 2. Figure 3-9 shows the transmission characteristic of the 4 micron liquid crystal cell placed between a crossed polarizer/analyzer as a function of normalized voltage. Figure 3-10 is the overall transfer function of the photoactivated light valve. As seen in the figure, a reasonably sharp toe is available for the threshold operation.

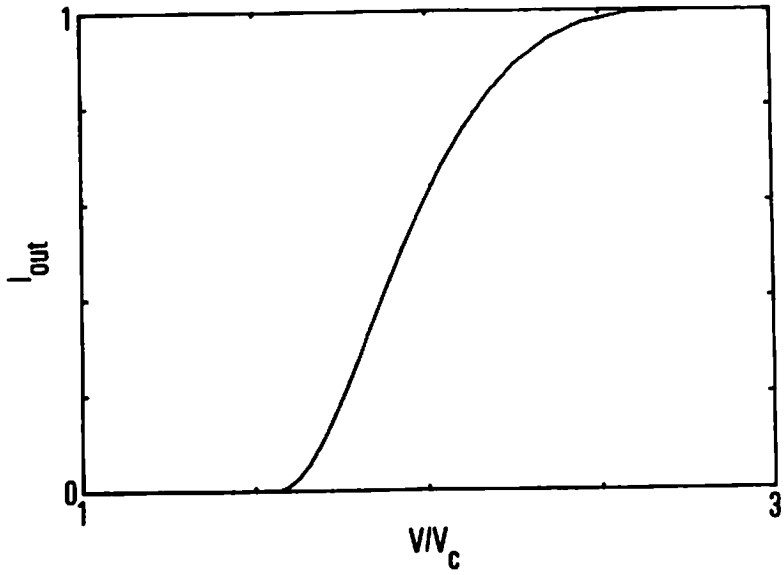

Figure 3-9 Transmission vs. normalized cell voltage for a 4 micron, 45 degree twisted nematic cell with crossed polarizer/analyzer

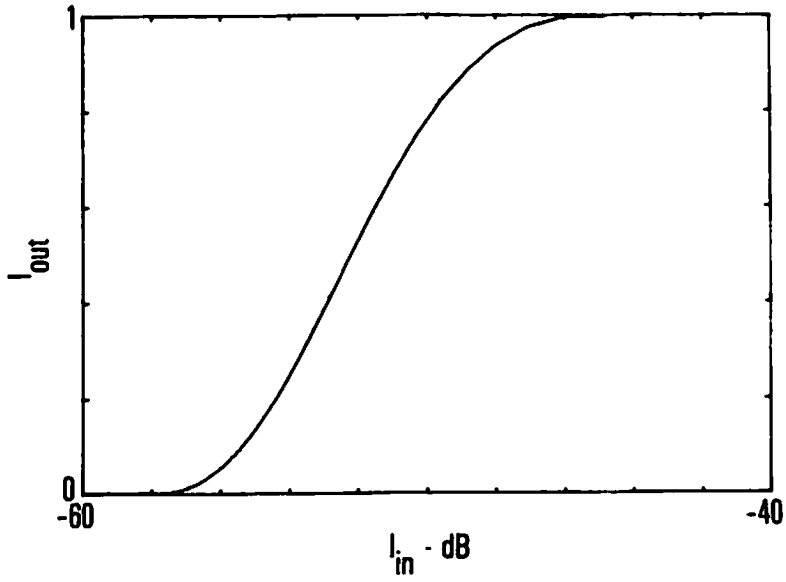

Figure 3-10 Intensity transfer function of threshold system

If the response from the contrast inverter shown in Fig. 3-8 is used as the input to the threshold device, then Fig. 3-11 shows the effect of the threshold operation in providing a narrower response as a function of swept bias voltage. As before, the input intensity to the threshold device was appropriately scaled by adjusting the magnitude of the read illumination to the contrast inverter.

The combination of the notch generator, contrast inverter, and thresholder comprise the intensity-to-time conversion operation of the nonlinear processing system. The overall response to the three input intensities used to generate Fig. 3-4 is shown in Fig. 3-12.

3.2.4 Temporal Weighter

The second major operation in the nonlinear processing system depicted in Fig. 3-1 is the weighting of the light impulses emanating from the intensity-to-time converter by the temporal intensity weighter. As described at the beginning of this chapter, the temporal intensity weighter is the element in the processing system used to introduce the desired nonlinear operation on the system's input intensity distribution. The weighter is in effect an electrooptic attenuator with sufficient dynamic range to accomplish the desired nonlinear transformation.

A transmission type liquid crystal cell operating

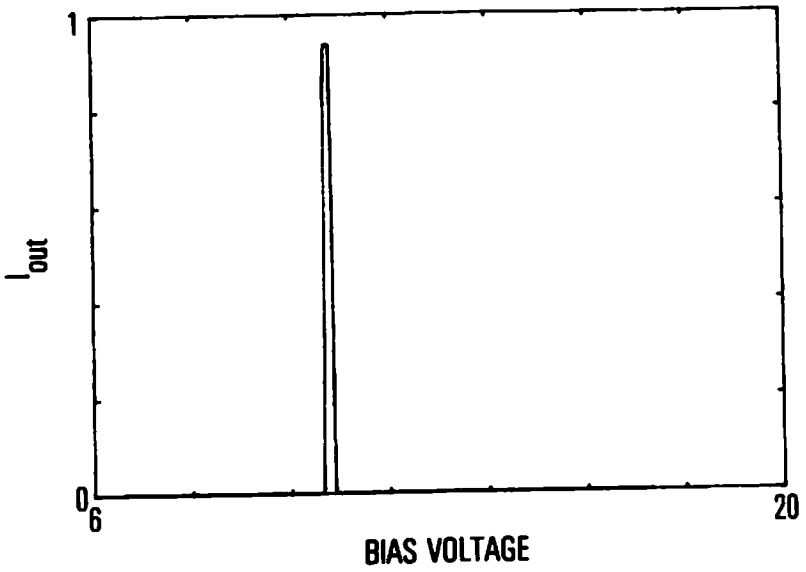

Figure 3-11 Threshold system response to input of Figure 3-8

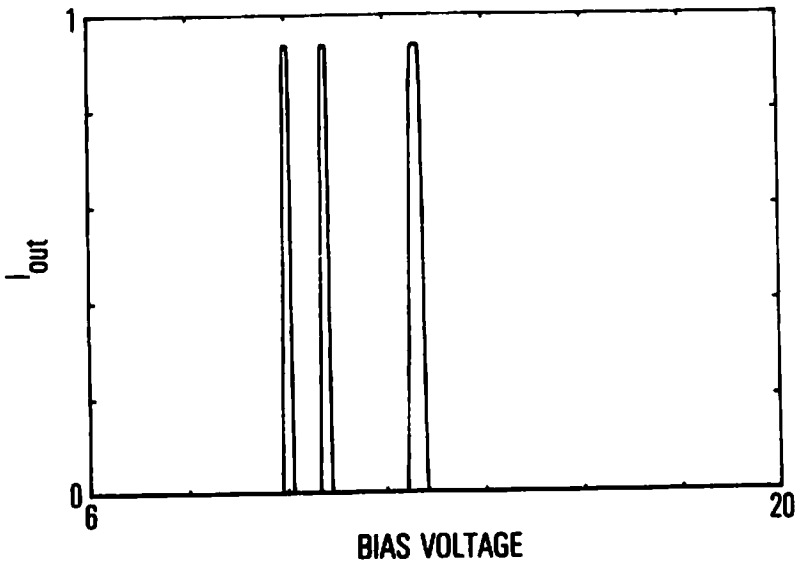

Figure 3-12 Overall response of intensity to time converter for three distinct input intensities

between a crossed polarizer/analyzer can conveniently be used for the electrooptic attenuator. To illustrate, consider a perpendicularly aligned uniform cell of thickness 8 microns. Figure 2-5 gives the normalized phase retardation vs. normalized inverse voltage for such a cell. Assuming $\Delta n=0.25$ for the liquid crystal material and incident light of wavelength 514.5 nm, then the maximum retardation is given by

$$\delta_0 = \frac{2\pi\Delta nd}{\lambda} = \frac{2\pi(.25)(8\times10^{-6})}{514.5\times10^{-9}} = 24.42 \text{ radians.} \quad (3.19)$$

If a critical voltage V_c=5 V rms is assumed, then Fig. 3-13 shows the phase retardation vs. applied voltage for the cell. If the liquid crystal molecules are defined to lie in an X-Y coordinate system with the long axis of the molecules aligned along the Y axis under high field conditions, then with the input polarizer aligned at an angle of 45 degrees to the X axis the transmission characteristics of the cell may be determined using the Jones formalism. With an input intensity $I_0 = E_0^2$, then the components of the incident wave along the X-Y axes are given by

$$\begin{bmatrix} U_x \\ U_y \end{bmatrix} = \frac{E_0}{\sqrt{2}} \begin{bmatrix} 1 \\ 1 \end{bmatrix} . \quad (3.20)$$

For a phase retardation of δ radians, the field at the output of the device is given by

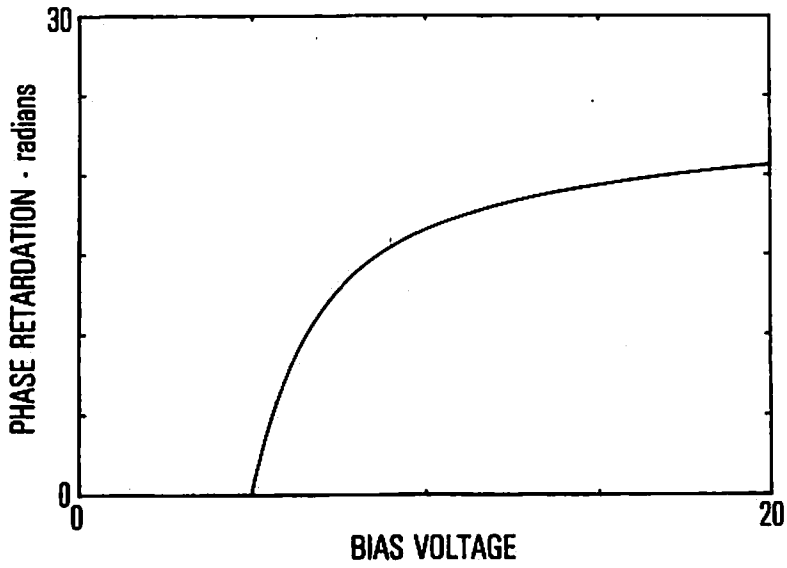

Figure 3-13 Phase retardation vs. applied cell voltage for transmission mode temporal weighter cell

$$\begin{bmatrix} U'_x \\ U'_y \end{bmatrix} = \begin{bmatrix} e^{j(\delta/2)} & 0 \\ 0 & e^{-j(\delta/2)} \end{bmatrix} \begin{bmatrix} U_x \\ U_y \end{bmatrix} \quad (3.21)$$

$$\begin{bmatrix} U'_x \\ U'_y \end{bmatrix} = \frac{E_0}{\sqrt{2}} \begin{bmatrix} e^{j(\delta/2)} \\ e^{-j(\delta/2)} \end{bmatrix} . \quad (3.22)$$

From Goodman [32], the matrix representation of a polarization analyzer oriented at an angle α to the X axis is given by

$$\underline{L}(\alpha) = \begin{bmatrix} \cos^2\alpha & \sin\alpha\cos\alpha \\ \sin\alpha\cos\alpha & \sin^2\alpha \end{bmatrix} . \quad (3.23)$$

Thus the X-Y components of the field at the output of the analyzer are given by

$$\begin{bmatrix} U_{0x} \\ U_{0y} \end{bmatrix} = \underline{L}(\alpha) \begin{bmatrix} U'_x \\ U'_y \end{bmatrix} . \quad (3.24)$$

$$\begin{bmatrix} U_{0x} \\ U_{0y} \end{bmatrix} = \frac{E_0}{\sqrt{2}} \begin{bmatrix} \cos^2\alpha e^{j(\delta/2)} + \sin\alpha\cos\alpha e^{-j\delta/2} \\ \sin\alpha\cos\alpha e^{j\delta/2} + \sin^2\alpha e^{-j\delta/2} \end{bmatrix} . \quad (3.25)$$

For the present case with the analyzer oriented perpendicular to the input polarizer, then $\alpha = 3\pi/4$ radians. Thus

$$\begin{bmatrix} U_{0x} \\ U_{0y} \end{bmatrix} = \frac{E_0}{\sqrt{2}} \begin{bmatrix} (e^{j\delta/2} - e^{-j\delta/2})/2 \\ (e^{-j\delta/2} - e^{j\delta/2})/2 \end{bmatrix} \quad (3.26)$$

$$\begin{bmatrix} U_{0x} \\ U_{0y} \end{bmatrix} = \frac{jE_0}{\sqrt{2}} \begin{bmatrix} \sin\delta/2 \\ -\sin\delta/2 \end{bmatrix} . \quad (3.27)$$

The output intensity is then given by

$$I_{OUT} = \begin{bmatrix} U_{0x} \\ U_{0y} \end{bmatrix} \begin{bmatrix} U_{0x} \\ U_{0y} \end{bmatrix}^{*} \qquad (3.28)$$

$$I_{OUT} = E_0^2 \sin^2 \delta/2 \quad . \qquad (3.29)$$

Applying Eq. (3.29) to the retardation data of Fig. 3-13, then for a unit magnitude input intensity Fig. 3-14 shows the transmission characteristics of the cell as a function of applied voltage. If the applied voltage is constrained to an interval such that the corresponding device transmission changes from a minimum to a maximum, then the desired electrooptic attenuator characteristic is obtained. The transmission characteristics for one such interval are shown in Fig. 3-15.

3.2.5 Temporal Integrator

The final function in the nonlinear optical processor depicted in Fig. 3-1 is that of temporal integration. The nonlinearly weighted impulses emerging from the temporal weighter are distributed sequentially over the time interval [0,T] corresponding to the sweep period of the bias voltage on the intensity notch generator. The purpose of the integrator then is to accumulate the weighted light impulses over this time interval and present them in parallel form at the end of the sweep period. This effectively removes the time element from the processing operation.

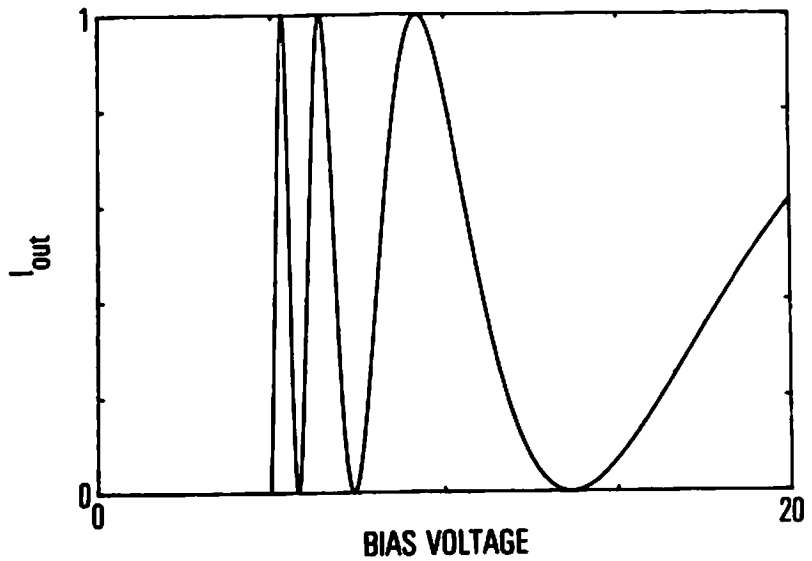

Figure 3-14 Temporal weighter transmission vs. bias voltage

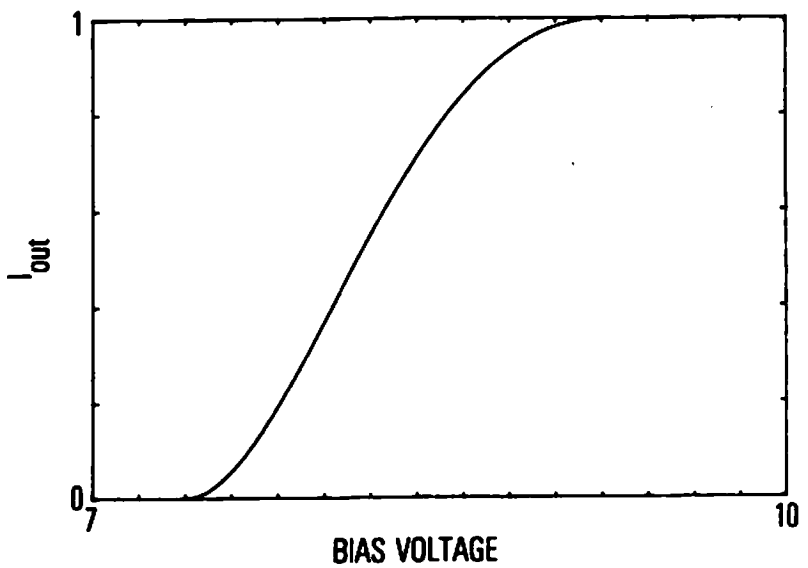

Figure 3-15 Selected bias interval of Fig. 3-14 used for temporal weighting function

Although some secondary storage effects in the liquid crystal light valves were observed during this study, the light valve is basically not a storage device and therefore cannot be used for the integration function. A number of devices do exist, however, that can suitably perform the integration. Two such devices used in this study are the silicon vidicon TV camera tube and photographic film. Using a vidicon, real time operation of the processing system is achievable. The manner in which the vidicon is used for the integration process is to halt the scanning on the vidicon surface during the bias sweep interval [0,T]. This allows the light from the temporal weighter to be accumulated and stored as a charge distribution on the photosensitive surface of the vidicon. At the end of the sweep period, the vidicon scan is resumed thus reading out the integrated charge for presentation on a suitable monitor or transmission over a communication link as desired.

The light integrating properties of photographic film are well known and offer a simple means of performing the integration task. While the use of photographic film precludes real time operation for many applications its use as the final integrator is tolerable and even desirable. This is particularly true if the nonlinear processor represents the final operation in a more complex image processing system where the final processed image is to be

retained for observation or further analysis. A vidicon system was used extensively during this study to observe the operation of the processing system. However, the results presented in this thesis were all obtained using photographic film as the temporal integration medium.

A third candidate for the temporal integration function is the class of optical and electrooptical devices capable of real time parallel image storage. Of particular interest is the PROM (Pockels Readout Optical Modulator) device [34]. While its use in the processing system was not investigated to any length during this study, it does offer significant potential as the final element in the nonlinear processor. The primary advantage of using such a memory device is that at the end of the integration period the final image is instantaneously available in coherent form for use in further optical processing operations. This is particularly advantageous if the nonlinear processor is simply one of several operations being performed on the original input image. A specific example of such an operation is in homomorphic image filtering. This and other conceptual applications will be considered in more detail in Chapter 7.

3.3 Nonlinear Processing System

In section 3.2 methods for implementing each of the five basic functions of the nonlinear processor were

described. Cascading each function as described, Fig. 3-16 shows one possible hardware configuration for realizing the overall processor. Lens L_1 images the input scene, image, or data onto the face of light valve $LCLV_1$. $LCLV_1$ is the notch generator described in section 3.2.1. Its bias voltage is derived from a programmable voltage source VS_1, in this case being controlled by a microprocessor system to produce the desired sweep voltage. The read illumination I_1 for $LCLV_1$ is polarized by P_1, passes through the light valve by reflection off of beamsplitter BS_1, and then is transmitted through BS_1 to the crossed analyzer P_2. From P_2 the light is focused by lens L_2 onto the contrast inverter implemented by light valve $LCLV_2$. The input intensity to $LCLV_2$ is appropriately scaled by adjusting the read illumination source I_1. The contrast inversion is completed as illumination I_2 passes through polarizer P_3, beamsplitter BS_2, the light valve $LCLV_2$, and finally out through parallel analyzer P_4. From P_4 the light is imaged onto the thresholder implemented with $LCLV_3$, again appropriately scaled by adjusting source I_2. $LCLV_3$ together with crossed polarizers P_5 and P_6 and beamsplitter BS_3 provide the thresholding operation with the final read illumination being supplied by source I_3. The fixed bias voltages for the contrast inverter and thresholder are supplied by voltage sources VS_2 and VS_3 respectively. The polarized light from P_6 is imaged by the system of lenses

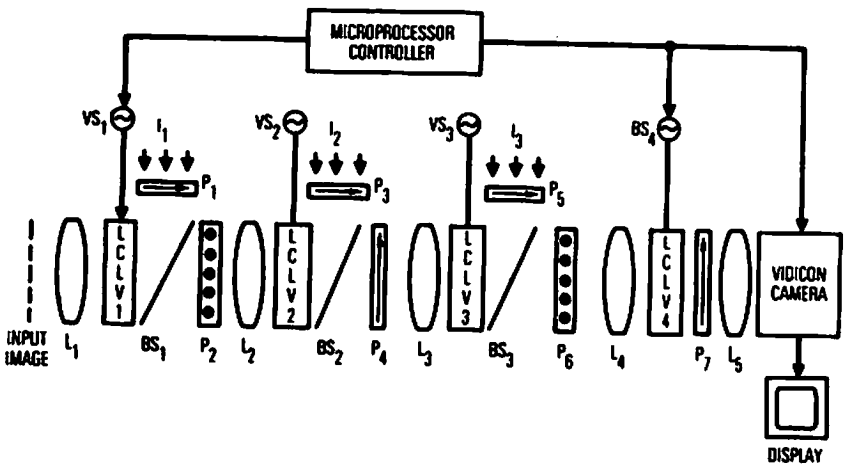

Figure 3-16 Light valve implementation of nonlinear image processing system

L_4 and L_5 through the temporal weighter implemented with $LCLV_4$, crossed analyzer P_7, and finally onto the vidicon integrator. The bias voltage for temporal weighter $LCLV_4$ is derived from programmable source VS_4, and is controlled in conjunction with source VS_1 by the microprocessor control system. The microprocessor further controls the scan time of the vidicon integrator, providing a command at the appropriate time to scan the vidicon's photosensitive surface and send the processed image to the display unit.

As mentioned above, Fig. 3-16 shows only one of many possible configurations for realizing the processor system. While it does serve to illustrate the theoretical processing system, the actual configuration used in this study to obtain the experimental results was slightly less elaborate and will be outlined in more detail in Chapter 5.

The maximum data throughput achievable with the nonlinear processing system can be estimated by using device parameters of presently available liquid crystal light valves[35]. For devices incorporating a thin (2-3 micron) liquid crystal layer and a CdS/CdTe photosensor, resolution on the order of 50 line pairs/mm and response times of 30 msec are achievable. Light valves with clear apertures of 46 mm diameter have been constructed implying a possible 4.15×10^6 resolution elements for the device. Thus for a 30 msec frame processing rate, the maximum

throughput achievable with the processing system would be on the order of 1.4×10^8 data points per second.

CHAPTER 4

EXPERIMENTAL VERIFICATION OF LIGHT VALVE THEORY

This chapter will present measured data and responses of three actual light valves used in the experimental processing system. The intent is not only to characterize the light valves for use in predicting the experimental results but also to verify that the theoretical performance characteristics developed in Chapter 2 are applicable to real devices. The three devices to be considered are representative of the functional types presented in Chapter 3 as needed to implement the temporal weighter, the notch generator, and the contrast inversion and threshold operations. In order of presentation, they are: 1) a transmission type voltage cell characterized by uniform perpendicular alignment; 2) a reflection mode photoactivated light valve characterized by uniform parallel alignment and a CdS/CdTe photosensor; and 3) a reflection mode twisted nematic device characterized by a 45 degree twist and a CdS/CdTe photosensor.

The light valves used in the processing system were all experimental devices obtained from the Hughes Research

Laboratories in Malibu,California. In general they were constructed for test purposes unrelated to this study. As a result, they were in many respects suboptimal for the processing system application in which they were used. Moreover, many of the device parameters required in the theory developed in Chapter 2, both for the liquid crystal cell and the photosensor, were not required for the original test purposes of the devices and as such were either not measured or not well documented. To circumvent this lack of information, the approach taken in relating the measured data to the theory was to obtain a best least squares fit of the theoretical responses to the measured responses. Significant unknown device parameters were varied in the theoretical responses to obtain the fit. In all cases the parameters were constrained to fall within reasonable limits supplied by individual researchers at the Hughes laboratories. Where individual device parameters were known and available, they were held constant in the curve fitting process.

4.1 Transmission Cell

The construction of the transmission cell used for the temporal weighter in the processing system is shown in Fig. 4-1. The device was fabricated such that under zero field conditions the liquid crystal molecules were uniformly aligned throughout the cell with their long axis

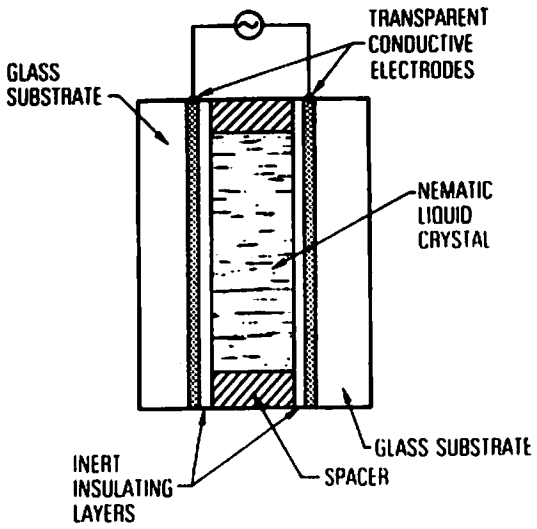

Figure 4-1 Cross section of transmission type liquid crystal cell

perpendicular to the substrates. The liquid crystals were separated from the transparent conductive electrodes by a thin insulating layer of S_iO_x. The liquid crystal material used was Shiff base MBBA with $\Delta n=0.25 \pm .02$. The thickness of the cell was estimated to be between 10 and 14 microns. The S_iO_x layers were known to be between 0.02 and 0.04 microns thick. Due to the dielectric properties of the S_iO_x layers, the voltage present across the liquid crystal layer will not be equal to the bias voltage applied to the conductive electrodes. Rather, it will be related to the applied bias through the ratio of the impedances represented by the liquid crystal and insulating layers, the exact relationship being

$$V_{LC} = \frac{Z_{LC}}{Z_{LC}+Z_{IL}} V_{BIAS} \tag{4.1}$$

Where Z_{LC} is the impedance of the liquid crystal layer and Z_{IL} is the combined impedance of the two insulating layers. If both the liquid crystal material and the S_iO_x layers are assumed to be pure dielectrics, then the impedances of Eq. (4.1) are given by

$$Z_{LC} = \frac{d_{LC}}{\omega A \varepsilon_0 \varepsilon_{LC}} \tag{4.2}$$

$$Z_{IL} = \frac{2d_{IL}}{\omega A \varepsilon_0 \varepsilon_{IL}} \tag{4.3}$$

where ω is the frequency of the applied bias, d_{LC} and d_{IL} are the thicknesses of the liquid crystal layer and a single insulating layer respectively, A is the area of the

structure, and ϵ_{LC} and ϵ_{IL} are the dielectric constants for the liquid crystals and S_iO_x respectively. Substituting Eqs. (4.2) and (4.3) into Eq. (4.1), we obtain

$$V_{LC} = \frac{V_{BIAS}}{1 + \frac{2d_{IL}\epsilon_{LC}}{d_{LC}\epsilon_{IL}}} \tag{4.4}$$

For the particular liquid crystal mixture used, the effective dielectric constant ϵ_{LC} is approximately equal to 5. The dielectric constant for S_iO_x is equal to 6. Thus, assuming worst case dimensions of 0.04 microns and 10 microns for the thicknesses of the insulating layers and liquid crystal layer respectively, Eq. (4.4) yields

$$V_{LC} = \frac{V_{BIAS}}{1+2\left(\frac{4\times10^{-8}}{1\times10^{-5}}\right)\left(\frac{5}{6}\right)} = 0.9934\ V_{BIAS}\ . \tag{4.5}$$

As seen from the results of Eq. (4.5), the insulating layers have little effect on the relationship between the applied bias and the actual voltage appearing across the liquid crystal layer. Thus within experimental tolerances, the effects may be neglected and it will be assumed that the full bias voltage applied across the cell represents the voltage appearing across the liquid crystal layer.

The response of interest in comparing experimental data with theory is the phase retardation vs. inverse applied voltage. The response is shown in normalized form for the theoretical uniform perpendicular cell in Fig. 2-5. The parameters necessary for comparing experiment to theory

are the critical voltage V_c and the maximum phase retardation δ_0 given by

$$\delta_0 = \frac{2\pi\Delta nd}{\lambda} \tag{4.6}$$

The critical voltage for the cell was unknown. However, from the results of other researchers [22] the critical voltage is in the range of 5 to 8 volts rms. The unknown parameter in determining the maximum phase retardation was the cell thickness d in Eq. (4.6) which could only be approximated at between 10 and 14 microns. Within the above constraints, d and V_c were both varied to obtain a best least squares fit of the experimental data to the theoretical response.

The configuration used to determine the device response is shown in Fig. 4-2. The incident light of wavelength 632.8 nm was passed through a polarizer oriented at 45 degrees to the axis of the liquid crystal molecules. A photomultiplier was placed at the output of the crossed analyzer to detect the cell response to changes in the bias voltage. As the bias voltage was varied from 0 to 20 volts, the voltages at which relative intensity maxima and minima occurred at the output were recorded. From relationship (3.26), starting at 0 radians phase retardation for the zero field state, it is seen that the relative maxima and minima occur at integer multiples of π radians of phase retardation.

It was well known from observations of the light valve that the response near the critical voltage would not exhibit the sharp threshold characteristic predicted by the theoretical models. This is the result of simplification of complex molecular forces and field conditions in the models near the transition region. As a result of this a priori knowledge, the experimental data obtained as described above was best fit to the theoretical curves in a region removed from the transitional critical voltage region. The experimental data is plotted together with the best fit theoretical curve in Fig. 4-3. The parameters V_c and d required to give the best fit were 5.9 volts and 13.8 microns respectively. From Eq. (4.6) this gives a maximum phase retardation δ_0 of 34.2 radians. As seen in the figure, good agreement is obtained except in the critical voltage region. Figure 4-4 shows the actual device response over the voltage interval where the phase retardation changed from 8π radians to 9π radians. This was the portion of the response used for the temporal weighter application in the processing system.

4.2 Photoactivated Uniformly Aligned Cell

The construction of the device used to implement the intensity notch generator is shown in Fig. 4-5. It is a photoactivated reflection mode device characterized by uniform parallel liquid crystal molecular alignment under

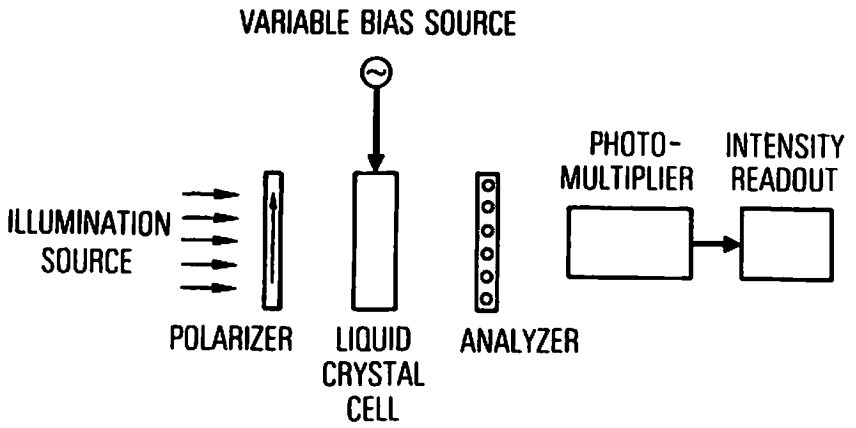

Figure 4-2 Test configuration for determining the characteristics of the transmission cell

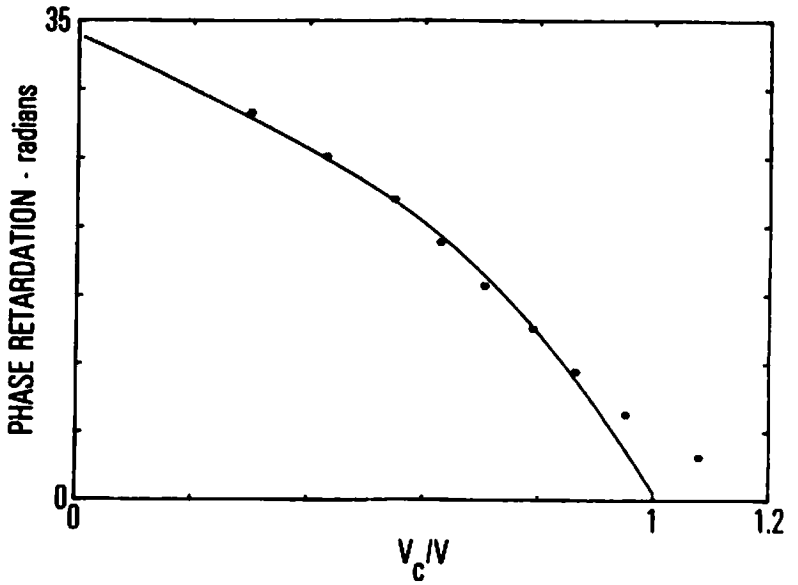

Figure 4-3 Experimental transmission cell phase retardation data

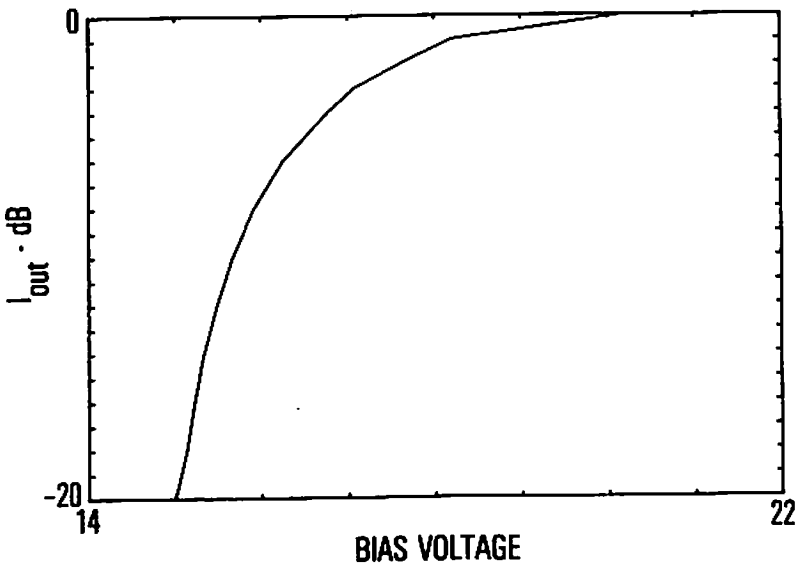

Figure 4-4 Measured transmission cell response vs. bias voltage

zero field conditions. The device was constructed with a broad band internal dielectric mirror and an 11 micron thick CdS/CdTe photosensor. The thickness of the liquid crystal layer was known to be between 3 and 4 microns.

Using the test configuration shown in Fig. 4-6, i.e. a crossed polarizer/analyzer pair oriented at 45 degrees to the liquid crystal axis, a read illumination of wavelength 632.8 nm, and a write illumination of wavelength 514.5 nm, then Fig. 4-7 shows the transmission characteristics of the cell as a function of applied bias voltage. The write illumination was set at its maximum value (approximately 2.8 mw/cm^2) in order to maximize the amount of bias voltage switched to the liquid crystal layer and thus obtain the largest possible phase retardation change over the range of bias used. At zero volts bias, the parallel aligned cell will exhibit its maximum phase retardation δ_0. Thus from Eq. (3.15) relating the intensity transmission to the phase retardation for a reflection mode device and the zero bias voltage data of Fig. 4-7, δ_0 is given by

$$\delta_0 = \sin^{-1}\left(\frac{I_R}{I_0}\right)^{\frac{1}{2}} = n\pi \pm 0.851 \text{ radians.} \qquad (4.7)$$

To determine the absolute magnitude of δ_0, Eq. (4.6) together with the known dimensional range of the liquid crystal thickness (2-3 microns) implies $4.96 \leq \delta_0 \leq 7.45$. Thus the factor n in Eq. (4.7) is determined to be 2. To

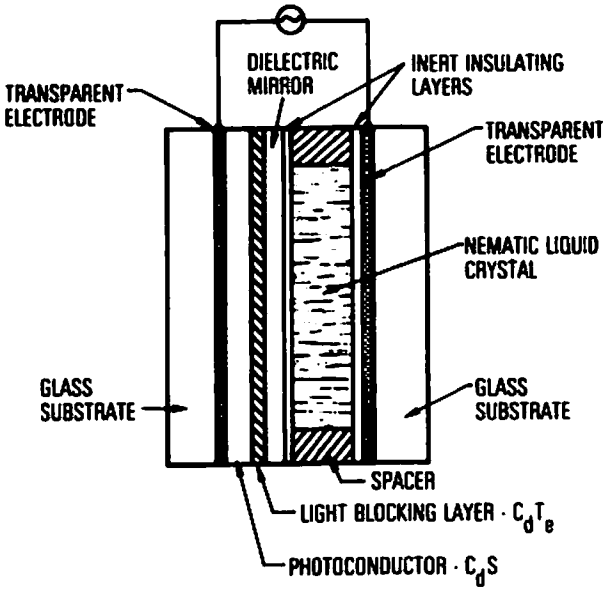

Figure 4-5 Cross section of photoactivated light valve

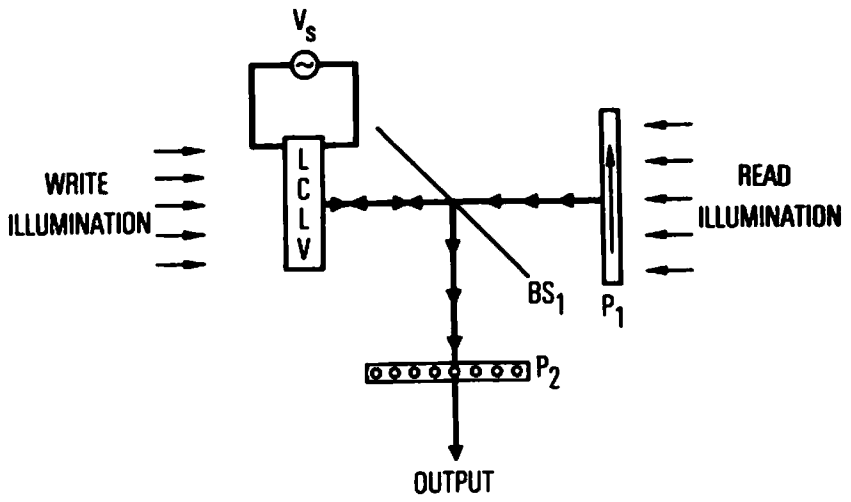

Figure 4-6 Test configuration for measuring response of photoactivated uniformly aligned light valve

determine the proper quadrant for δ_0, from Fig. 4-7 it is noted that as the bias voltage is increased from zero volts the device transmission increases reaching a maximum at approximately 6.7 volts bias. From Eq. (3.15), relative transmission maximas occur at integer multiples of $\pi/2$ radians of phase retardation. This observation together with the fact that the phase retardation decreases with increasing cell voltage for a parallel cell clearly necessitates the use of the negative sign in Eq. (4.7) giving a value for δ_0 of 5.4324 radians. Using this value in Eq. (3.15), the actual cell thickness is calculated to be 2.188 microns.

The phase retardation as a function of voltage for the parallel aligned cell was developed in section 2.3 with the final relationship given by Eq. (2.44). Using the value for δ_0 determined above and the data of Fig. 4-7, the normalized phase retardation vs. inverse normalized voltage is shown in Fig. 4-8 together with the theoretical curve of Fig. 2-7. A modified critical voltage of 8.5 volts was used to best fit the data with the theoretical curve. The critical voltage is modified in the sense that the data reflects the bias voltage on the overall device and not the actual cell voltage. To a first order, the actual cell voltage is related to the bias voltage by a fractional constant determined by the relative impedances of the various dielectric layers in the light valve

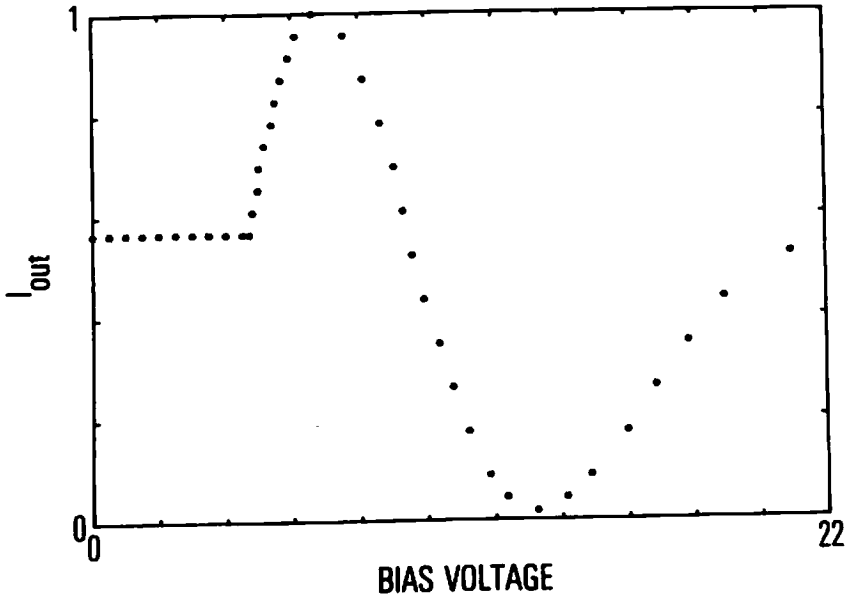

Figure 4-7 Measured transmission vs. bias voltage for uniformly aligned photoactivated device

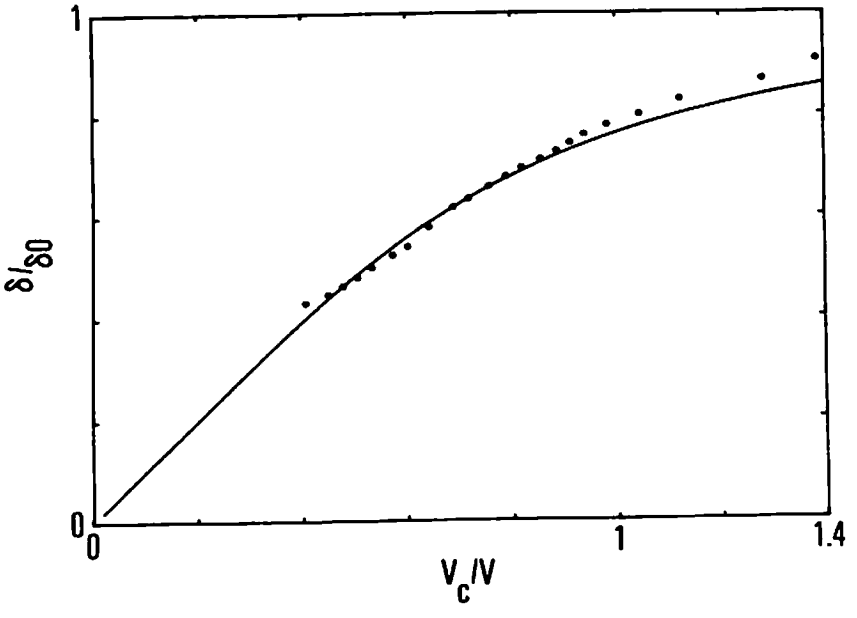

Figure 4-8 Measured phase retardation vs. inverse voltage for uniformly aligned photoactivated cell

structure. Thus the modified critical voltage of 8.5 volts incorporates this constant and the actual liquid crystal voltage is somewhat less. Agreement of the data with the theory in Fig. 4-8 is reasonable. The deviations may be attributed to a combination of measurement error, second order effects making the relationship of the bias voltage to the cell voltage nonlinear, and the deterioration of the theoretical model for voltages near the critical voltage threshold.

To determine the theoretical response of the device to changes in input intensity under fixed bias conditions, it is first necessary to determine the impedance of the internal dielectric mirror. The mirror impedance is in series with the impedance represented by the liquid crystal layer and the light-dependent impedance of the CdS/CdTe photosensor. Thus for a given photosensor current, a fraction of the bias voltage will be present across the photoconductor, a second fraction across the mirror, and the remainder will be present across the liquid crystal layer. The mirror was designed to be broadband and consists alternately of 8 layers of MgF and 7 layers of ZnS with dielectric constants of 5.5 and 10 respectively. The thickness of each MgF layer is 0.1867 microns giving an overall MgF thickness of 1.49 microns. Each ZnS layer is 0.112 microns thick. Thus for 7 layers the total ZnS thickness is 0.784 microns. Therefore, for the given

dielectric constants and layer thicknesses, the capacitance/cm^2 of the total MgF layer is calculated to be 3266 pf/cm^2 and that of the ZnS is 0.0113 $\mu f/cm^2$. The total mirror capacitance is simply the series combination of the above individual layer capacitances and is calculated to be 2534 pf/cm^2.

For a photosensor thickness of 11 microns, $\varepsilon = 4.4275 \times 10^{-11}$, $\delta = 2.6667$ microns, a mirror capacitance of 2534 pf/cm^2, a liquid crystal capacitance of 2024 pf/cm^2 as calculated for a thickness of 2.188 microns, and a bias voltage of 12.37 volts, then using the photosensor theory of section 2.6, Fig. 4-9 shows the calculated liquid crystal voltage as a function of input intensity in db. If this data is then applied to the theoretical retardation vs. cell voltage given by Eq. (3.15), then for a maximum retardation of 5.4324 radians and a critical voltage of 2.47 volts, the solid line in Fig. 4-10 shows the calculated device transmission as a function of db input intensity. Plotted together with the theoretical curve is actual data taken from the experimental device for a bias voltage of 12.37 volts. The data is seen to be in very good agreement with theory thus demonstrating the validity of the theoretical models developed in Chapter 2.

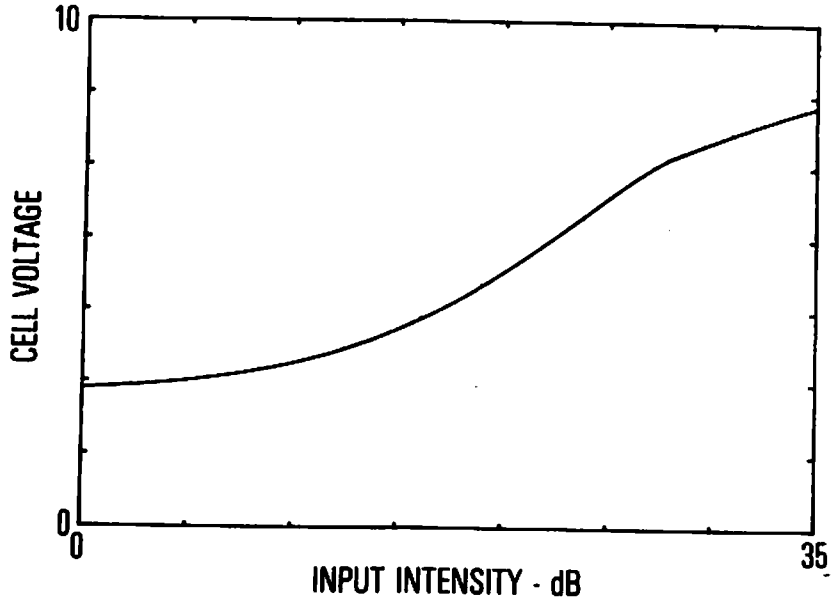

Figure 4-9 Calculated cell voltage vs. input intensity for uniformly aligned test cell

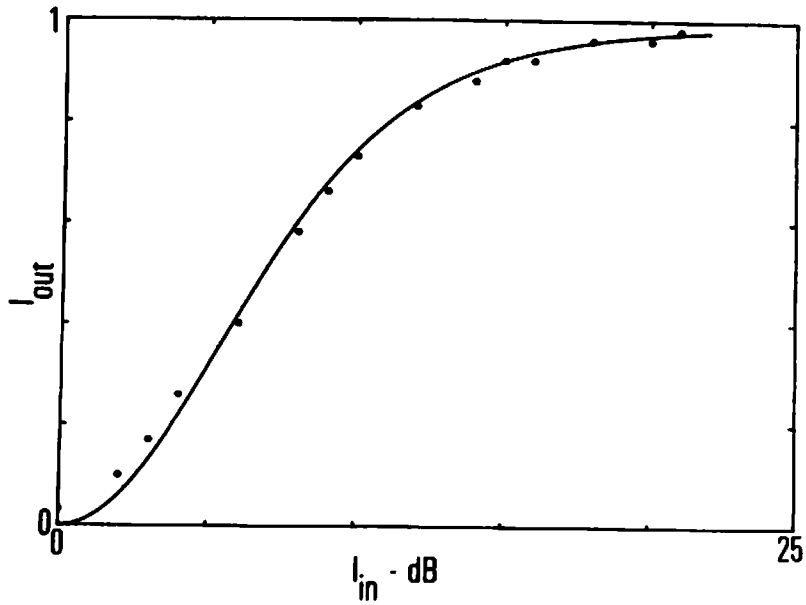

Figure 4-10 Measured and calculated response of uniformly aligned device for a bias voltage of 12.37 volts

4.3 Twisted Nematic Light Valve

The construction of the twisted nematic light valve is nearly identical to that of the uniformly aligned cell shown in Fig. 4-5. The major difference is that the liquid crystal molecules undergo a uniform twist of 45 degrees through the cell. The transmission characteristics for such a cell configuration were developed in section 2.4. To verify the theory, the cell was placed in the test configuration of Fig. 4-6. Again the polarizer/analyzer combination were oriented orthogonal to each other, the read illumination was at a wavelength of 632.8 nm, and the write illumination was at 514.5 nm.

The physical properties of the light valve were reasonably well documented during its manufacture. The thickness of the liquid crystal layer was set at 4 microns and the mixture used was a commercially available material designated E_7 whose properties are well documented [33]. Those properties of particular interest for the present purposes are a threshold voltage of 1.05 volts, dielectric constants ε_{11} and ε_{1} of 16 and 5 respectively, and a refractive index difference Δn of 0.24. The photoconductor used in the device was identical to that used in the uniform parallel device of section 4.2, i.e. 11 micron thick CdS/CdTe. The dielectric mirror was also the same being of broadband design and thus as previously calculated

represented a pure capacitance of 2534 pf/cm^2. As seen by the substantial difference in dielectric constants for the E_7 material, as the voltage on the cell is increased and the molecules tilt toward normal alignment with respect to the cell electrodes, the capacitance of the cell will change dramatically. In the limit the change will be from 1107 pf/cm^2 in the zero field state to 3542 pf/cm^2 under very high field conditions. Thus the load that the liquid crystal cell presents to the photosensor will be a nonlinear function of the voltage across the cell. The nonlinear relationship was calculated in section 2.5 and is shown in Fig. 2-15.

To demonstrate the effects of the twisted cell on device orientation with respect to the polarization of the read illumination, transmission data as a function of bias voltage was obtained for the device when the input polarization was oriented at 0, 22.5, and 45 degrees with respect to the axis of the liquid crystal molecules at the input face of the device. The results are shown in Fig. 4-11a. Using the theory of Chapter 2, comparable curves were generated using the physical device parameters outlined in this section. The results of these calculations are shown in Fig. 4-11b. Due to the nonlinear loading effects effects of the liquid crystal cell described above, the voltage scales in Figs. 4-11a and 4-11b are related in a nonlinear manner making absolute

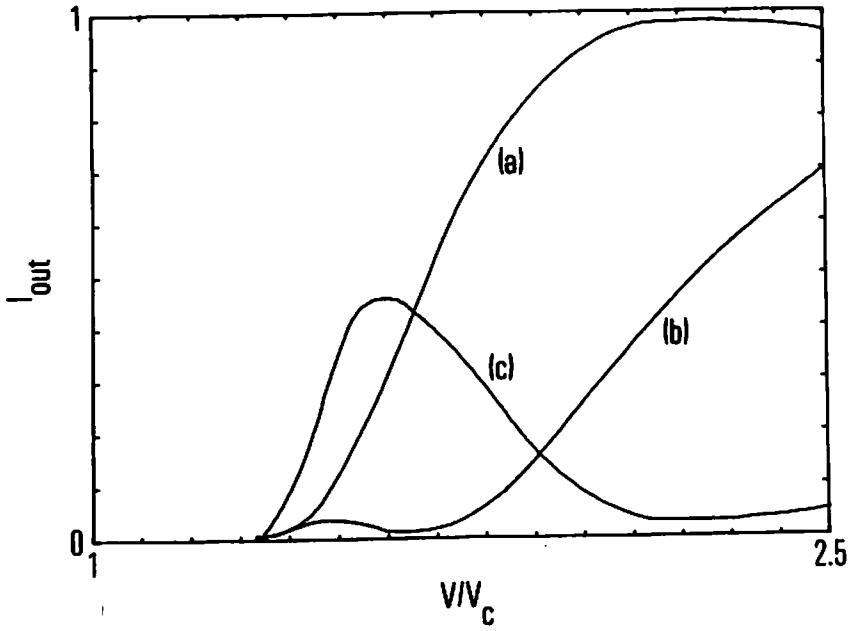

(a)

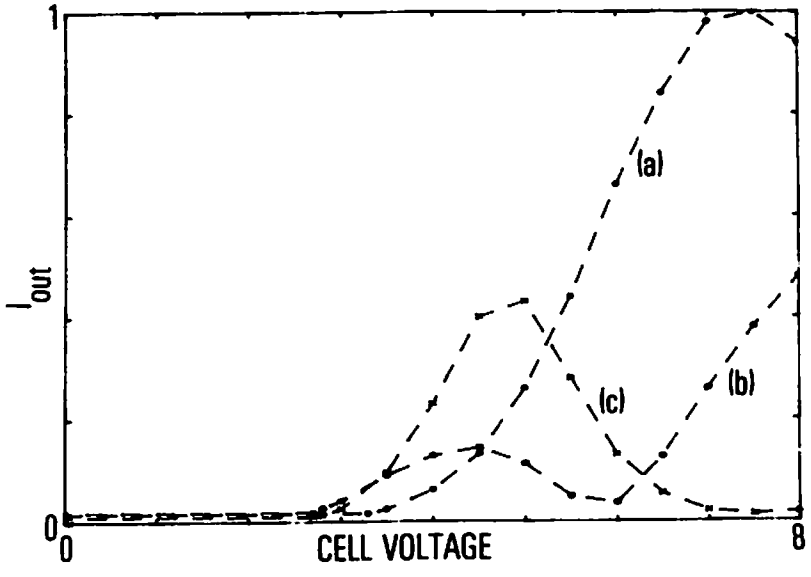

(b)

Figure 4-11 Effect of orientation of twisted nematic cell on device response
(a) Measured response
(b) Calculated response

comparisons difficult. The important thing to note in comparing the two figures is the shape of the responses for the three orientations and in particular the relative positions of the maxima and minima with respect to each other. As noted in the figures, agreement of data and theory is reasonably good demonstrating the validity of the twist model given in section 2.4.

To test the theoretical interaction of the photosensor with the twist cell, transmission data was collected on the test device for zero degree orientation and a bias voltage of 9.45 volts. The input illumination was varied from 0 to 2.8 mw/cm^2. The data is shown in Fig. 4-12 as a function of db input intensity. The solid line in the figure is the calculated response using the theory developed in chapter 2. As can be noted, reasonable agreement is obtained for the lower input light levels. The deviation at high input light levels is attributable primarily to the sensitivity factor K in Eq. (2.110). Near photoconductor saturation this factor is no longer constant but rather becomes related in a nonlinear manner to the input intensity I [29-30]. As a result, the quadratic relationship of n with incident intensity in Eq. (2.110) is no longer valid leading to erroneous predictions of light valve performance. As used in the nonlinear processing system, the twisted nematic light valve is never operated near saturation. Thus for the purposes of this experiment the

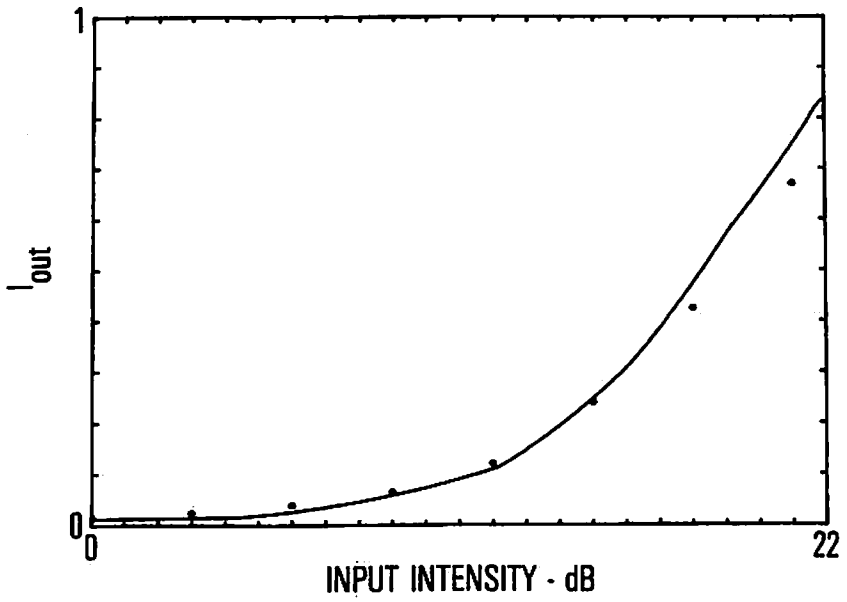

Figure 4-12 Measured transmission vs. input intensity of twisted nematic light valve

simplified model of the photosensor given in section 2.6 is seen to be adequate for use in predicting light valve and system performance because of the agreement of the low light level data of Fig. 4-12.

CHAPTER 5

EXPERIMENTAL PROCEDURES AND RESULTS

In Chapter 3, a theoretical nonlinear processing system was presented which utilized four distinct liquid crystal devices together with a temporal integrator. As discussed in that chapter the actual experimental system was slightly less elegant in that only three devices were available. These devices were a perpendicularly aligned transmission cell, a twisted nematic photoactivated reflection mode cell, and a parallel aligned photoactivated reflection mode cell. Due to the lack of four devices, in particular two twisted nematic light valves, the tasks of contrast inversion and thresholding were implemented with a single twisted nematic device. As shown in section 3.2.2 when such a cell is used for contrast inversion it also produces the secondary effect of thresholding due to the limiting characteristic of the device's transfer function. In the experimental system, the illumination derived from the intensity notch generator and used as input to the contrast inverter was increased thus moving the operating point on the contrast inverter transfer curve of Fig. 3-7

nearer the "toe" of the curve. This effectively provides more of a thresholding characteristic from the contrast inverter. The overall experimental nonlinear processing system is shown schematically in Fig. 5-1. The absence of a distinct thresholding element limits the performance of the system in the form of reduced intensity resolution. However, as will be shown the abbreviated system provides sufficient resolution to perform nonlinear operations on selected input images and provide a basis for demonstrating system feasibility.

As shown in Fig. 5-1, the operation of the processing system was governed by a microprocessor-based controller. The controller performed the task of simultaneously providing the swept bias source for the intensity notch generator and the nonlinearly shaped bias source for the temporal weighter. When the vidicon camera system was employed for the final integration task, the microprocessor controller also supplied appropriately timed signals to inhibit or start the vidicon raster scan as described in Chapter 3. The digitally based control system derived the two bias voltages through the use of D/A converters and a pair of four quadrant analog multipliers operating on a constant voltage AC source. The controller system is shown in Fig. 5-2.

The transfer function of the intensity notch generator

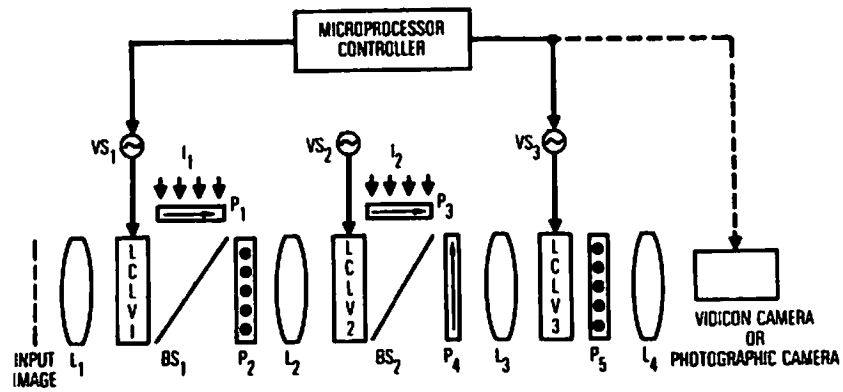

Figure 5-1 Experimental nonlinear image processing system

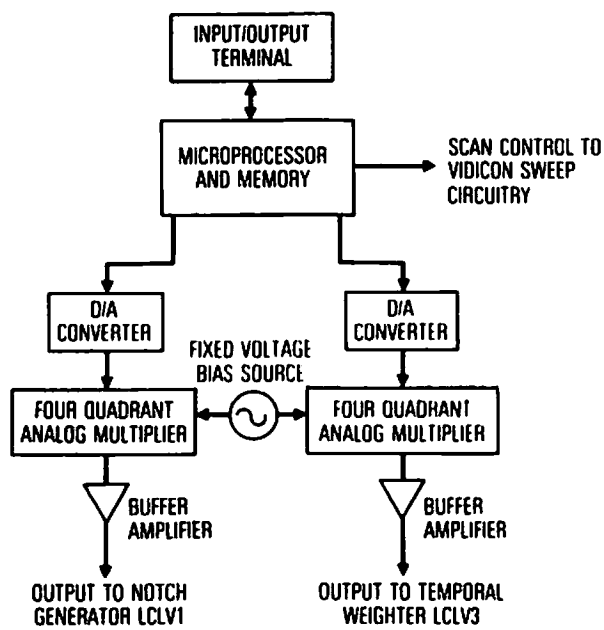

Figure 5-2 Block diagram of microprocessor control system

was carefully measured and the data reflecting the voltages at which intensity nulls occurred over an input intensity range of 26 db was stored in the microprocessor memory. Similarly, the voltage vs. attenuation characteristic of the temporal weighter was measured and the results stored in memory. Using this data base, the microprocessor was then programmed to perform four nonlinear operations upon command, i.e. level slice, logarithm, exponentiation, and A/D conversion.

Figures 5-3 and 5-4 show the preintegration responses of the processing system during a single sweep period of a level slice operation. A known constant intensity was input to the system during the sweep period. Figure 5-3a shows the response of the intensity notch generator as a function of sweep time. In Fig. 5-3b, the intensity out of the contrast inverter/thresholder is shown for the same sweep interval. Figure 5-4a shows the voltage out of the D/A converter used to control the bias supply for the temporal weighter for the level slice operation. For the simple case of a level slice, the voltage limits correspond to the voltages necessary to switch the temporal weighter from maximum attenuation to maximum transmission. The final preintegration output intensity from the system is shown in Fig. 5-4b.

Similar discrete intensity response measurements were

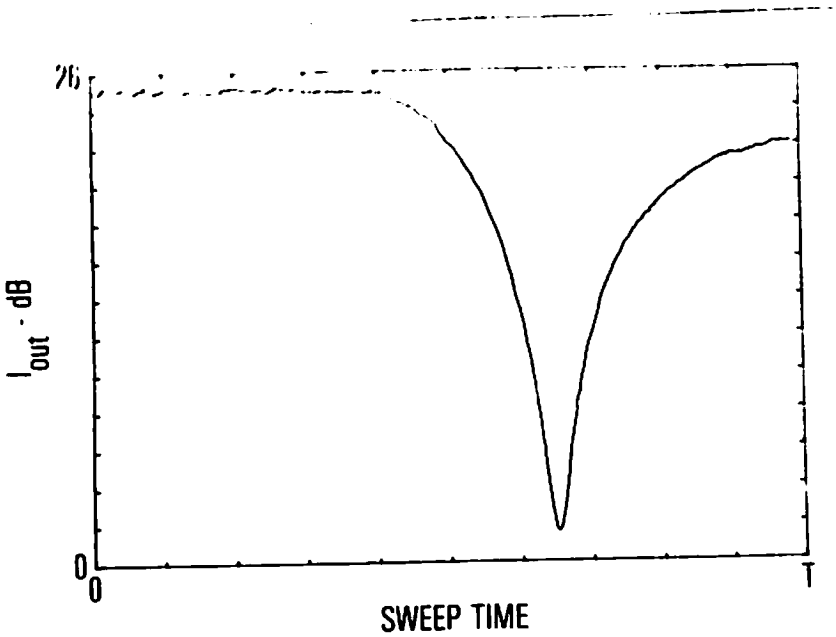

(a)

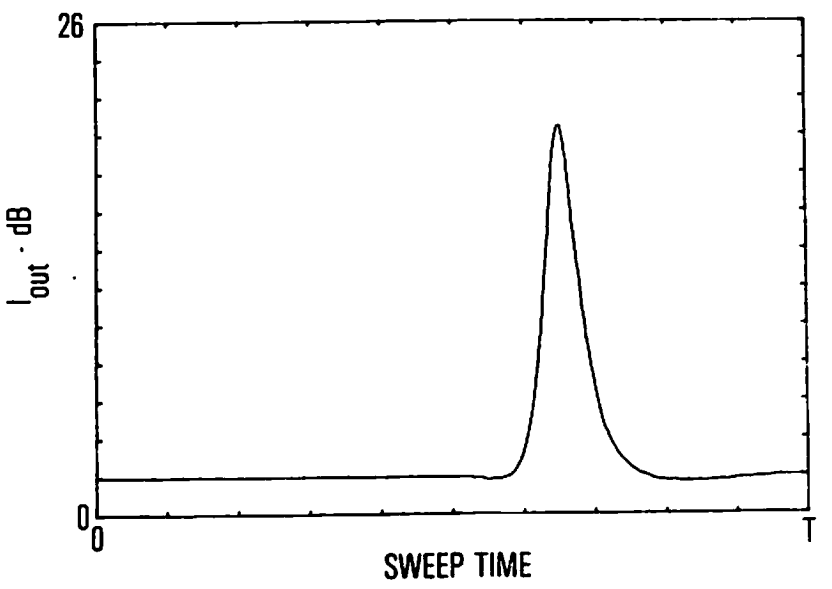

(b)

Figure 5-3 System response vs. sweep time for single input intensity
(a) Notch generator response
(b) Contrast inverter/thresholder response

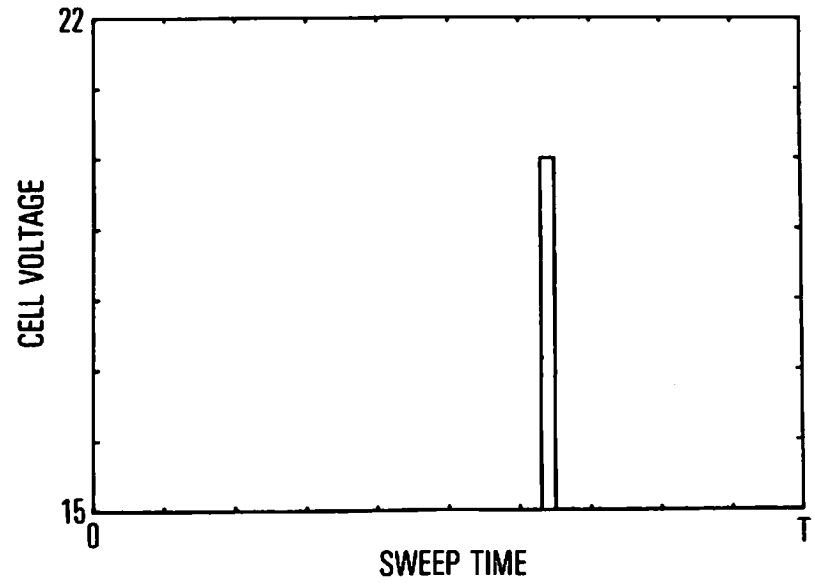

(a)

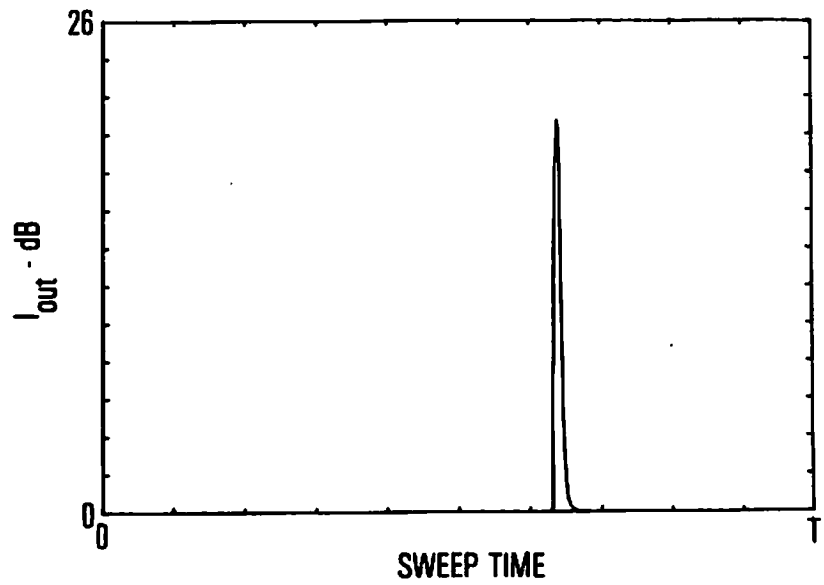

(b)

Figure 5-4 System response vs. sweep time for single input intensity
(a) Temporal weighter control voltage for level slice operation
(b) Preintegrated overall response for level slice operation

made with the microprocessor placed in the logarithm and exponentiation modes. Repeated measurements of the output intensity were made in each mode as the input intensity was varied in 2 db steps over a total range of 20 db. The results for the logarithm and exponentiation operations are shown in Figs. 5-5 and 5-6 together with the appropriate calculated responses. The slight deviations of the measured values from the calculated curves are attributable not only to measurement error but also to the tendency of the light valves' transfer functions to change slightly with temperature.

The response of the system to operations on variable intensity, two dimensional input images is shown in Figs. 5-7 through 5-18. Figure 5-7 shows the original discrete intensity test image used as input to the system. The test pattern cells spanned a range of 23 db of input intensity with each cell being repeated a minimum of 3 times throughout the pattern. Figures 5-8 through 5-11 show the integrated system response for four different level slice operations on the test pattern. Included in each figure is the corresponding computed bias voltage applied to the temporal weighter to implement the operation. The effects of limited system intensity resolution both as a consequence of the lack of a unique thresholding operation and light valve nonuniformities can be observed in the photographs in the form of incomplete

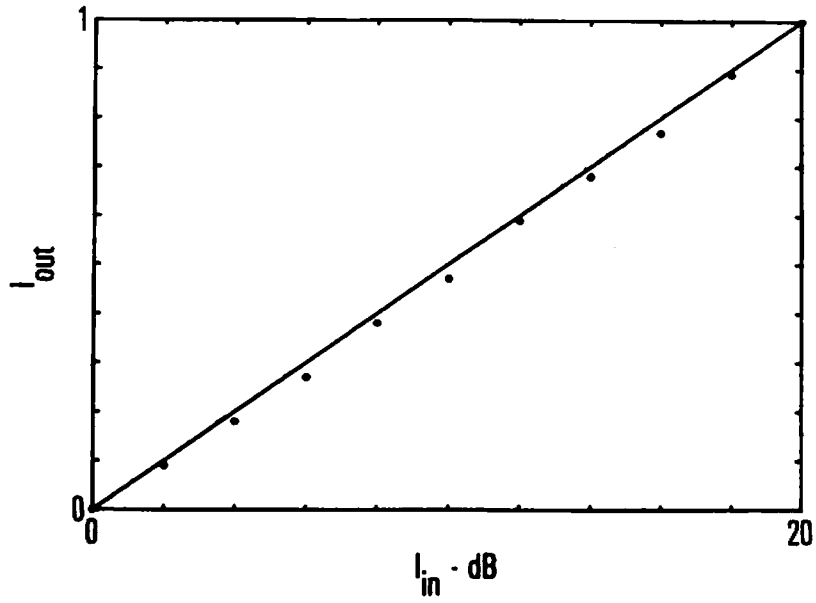

(a)

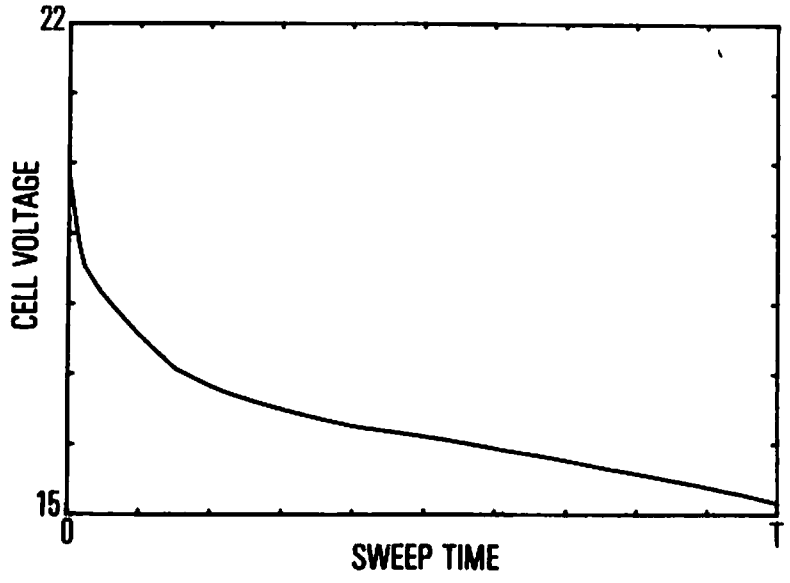

(b)

Figure 5-5 Logarithm operation
(a) System output response
(b) Temporal weighter control voltage

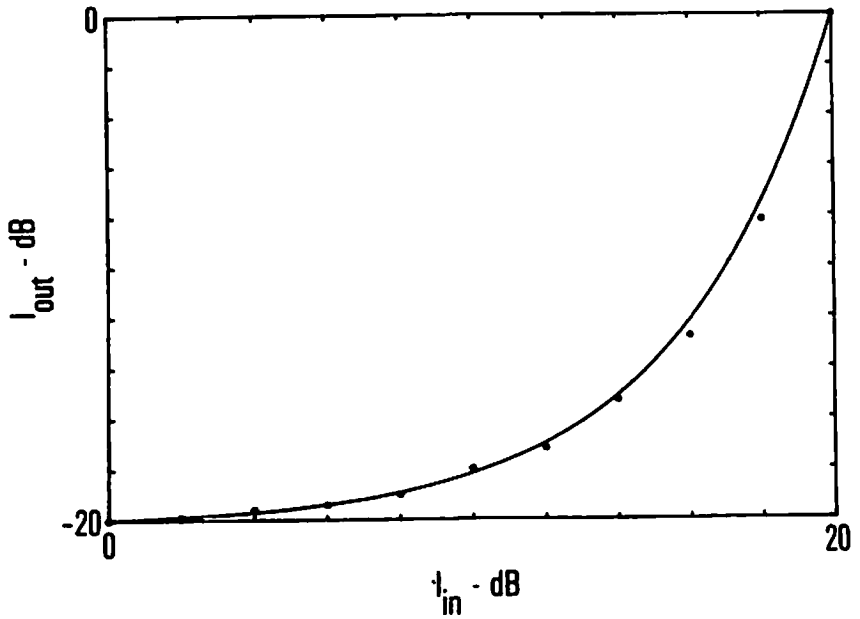

(a)

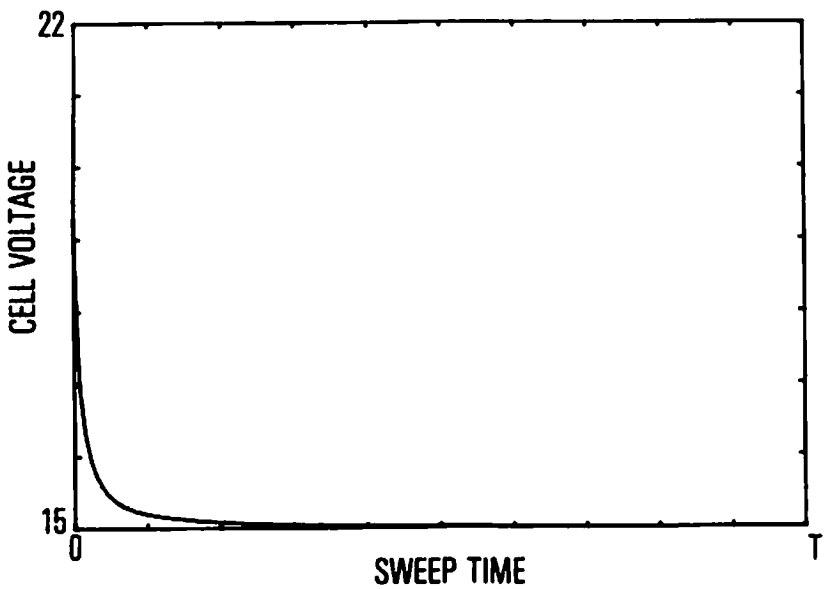

(b)

Figure 5-6 Exponentiation operation
(a) System output response
(b) Temporal weighter control voltage

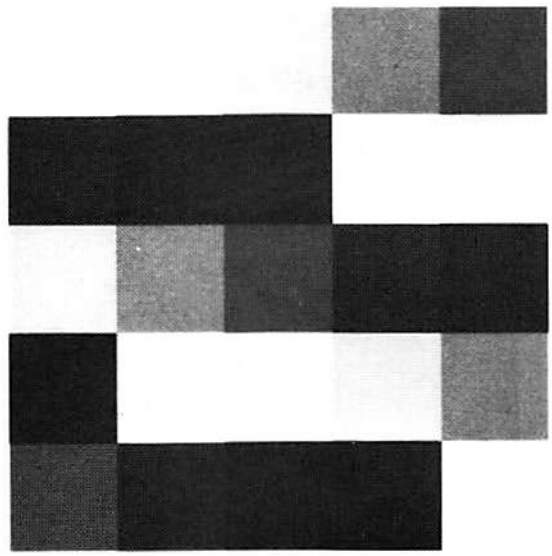

Figure 5-7 Two dimensional discrete density input image test pattern

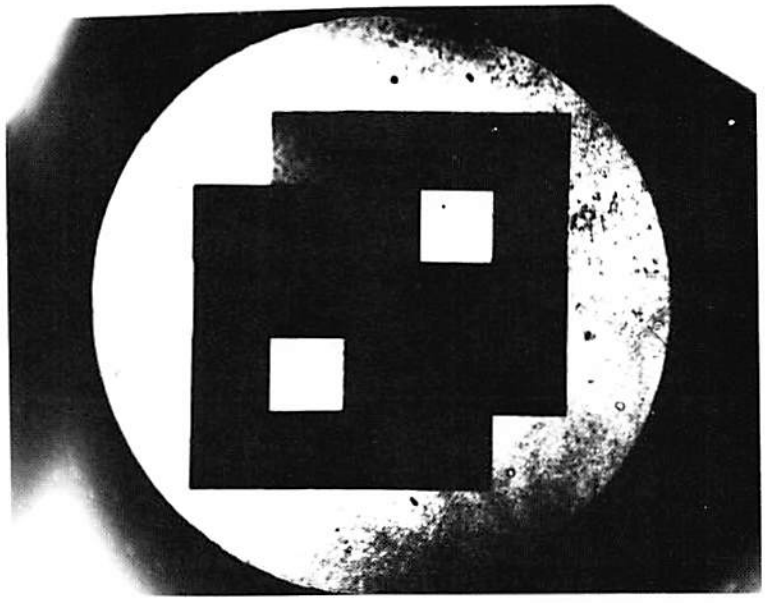

(a)

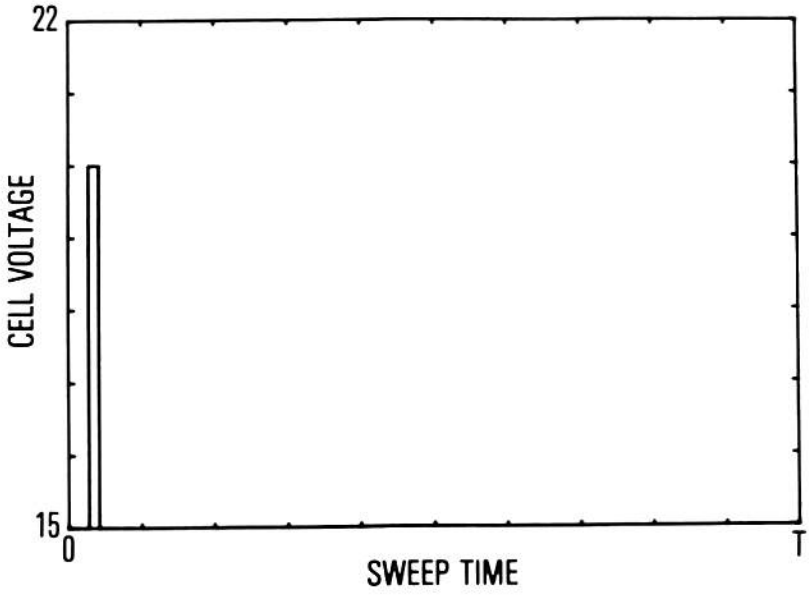

(b)

Figure 5-8 Level slice operation to select density 0.13
(a) System response
(b) Temporal weighter control voltage

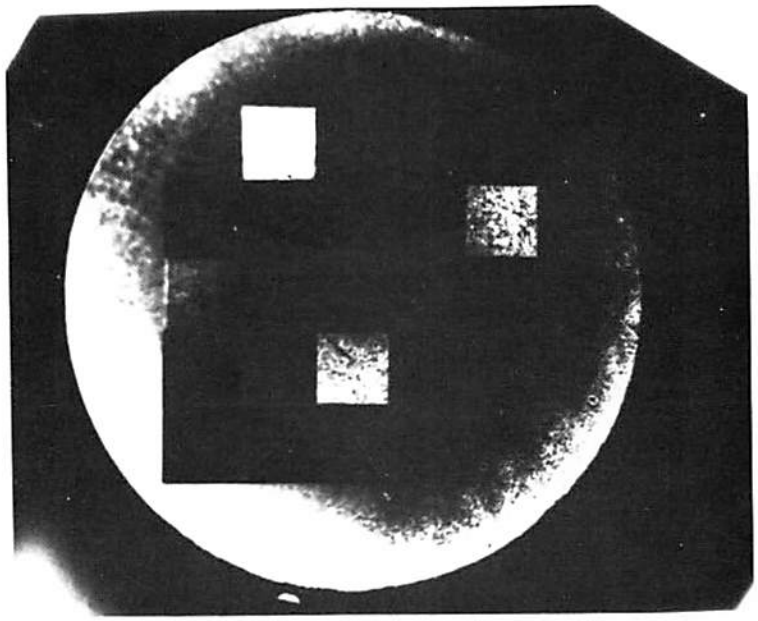

(a)

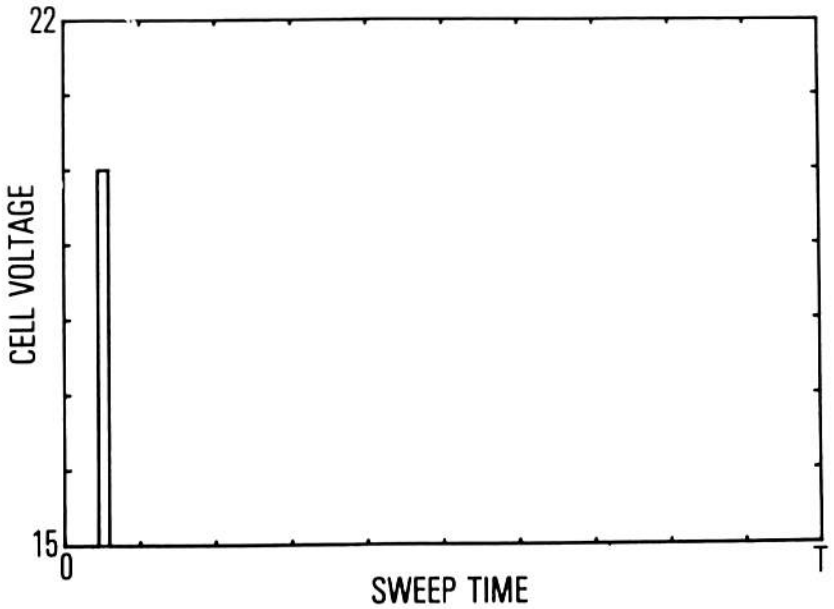

(b)

Figure 5-9 Level slice operation to select density 0.55
(a) System response
(b) Temporal weighter control voltage

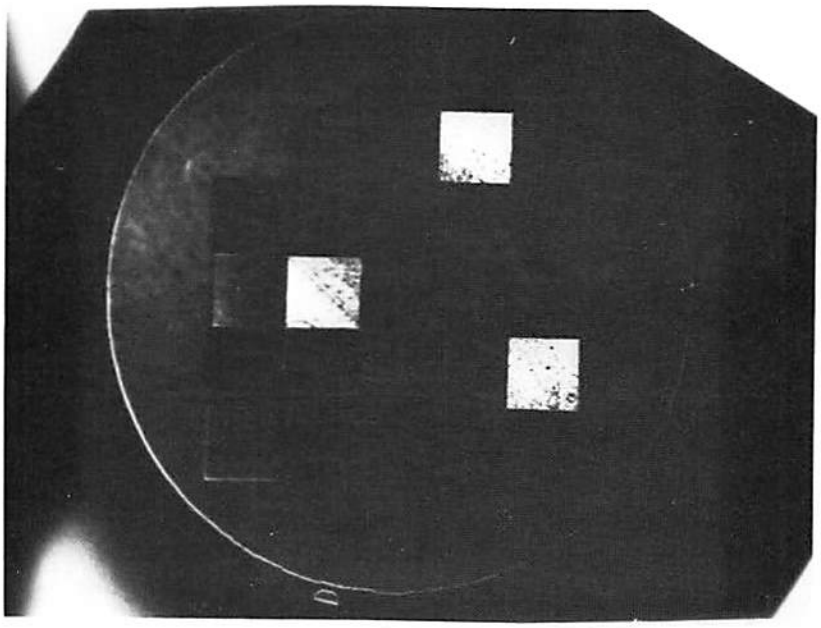

(a)

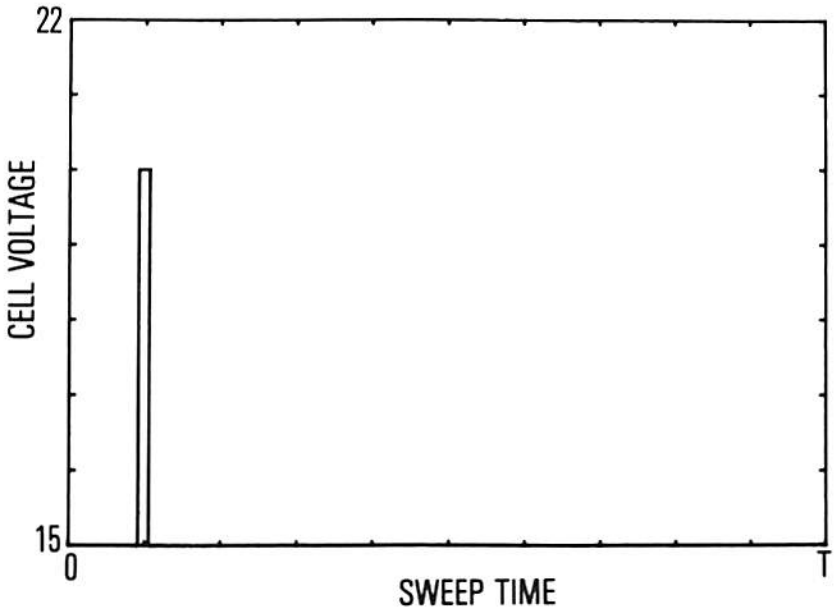

(b)

Figure 5-10 Level slice operation to select density 0.97
(a) System response
(b) Temporal weighter control voltage

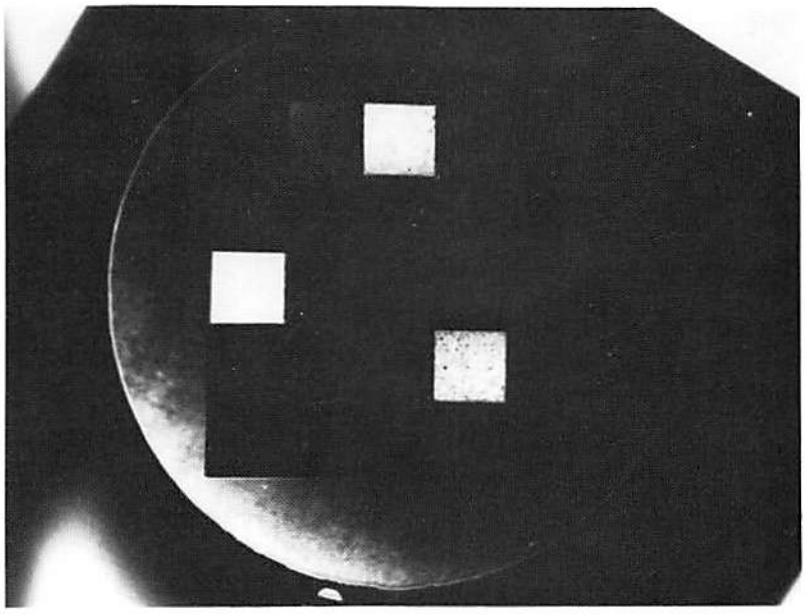

(a)

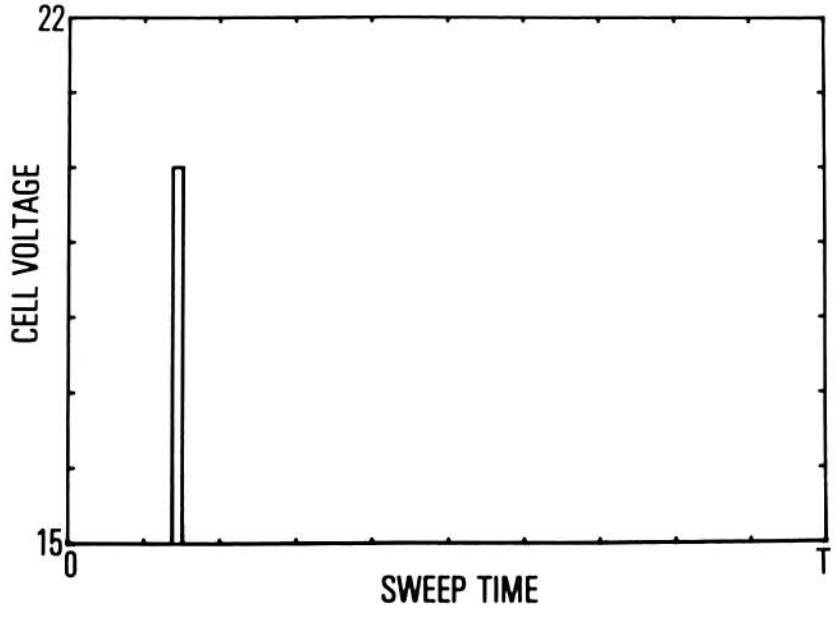

(b)

Figure 5-11 Level slice operation to select density 1.3
(a) System response
(b) Temporal weighter control voltage

extinction of adjacent intensity cells.

The results of the slightly more complex operation of A/D conversion are shown in Figs. 5-12 through 5-14. The third row of the input intensity test pattern of Fig. 5-7 was digitized to 3 bits, each output image bit plane requiring a separate processor operation. The microprocessor was programmed to perform the digitization over db input intensity, i.e. eight distinct 3 db intensity bands spanning 24 db. The choice was somewhat arbitrary and through simple reprogramming of the microprocessor controller the digitization could be performed on the basis of absolute intensity.

Figures 5-15 through 5-18 show the system response to continuous tone input images. Again the basic operation of level slicing is shown. The effects of the limited intensity resolution of the abbreviated test system and the nonuniformities present in the experimental light valves become most apparent for operations on continuous tone images.

The preceding results all were obtained using photographic film for the final integration process. As mentioned previously, the vidicon camera system was used extensively throughout the experimentation primarily to demonstrate the real time operating characteristics of the processing system. Using the vidicon system, real time

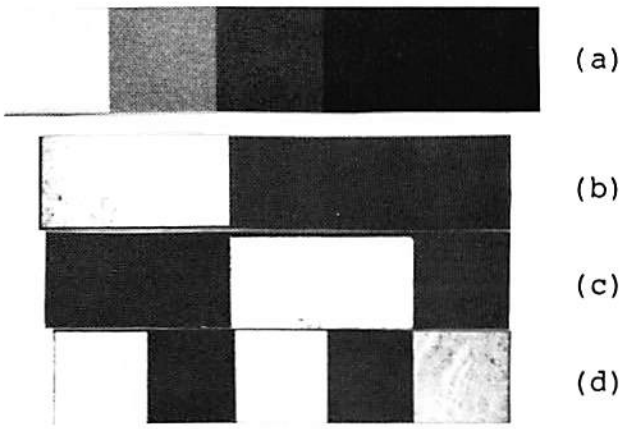

Figure 5-12 A/D conversion operation
(a) Input image
(b) Most significant bit plane
(c) Second most significant bit plane
(d) Least significant bit plane

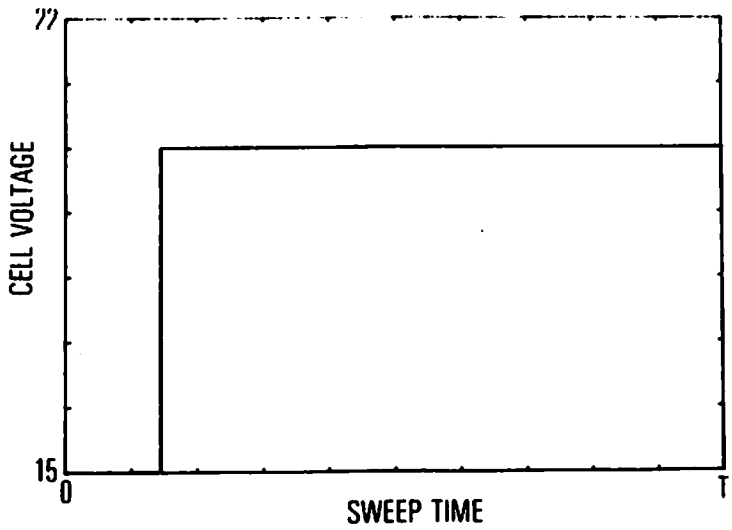

(a)

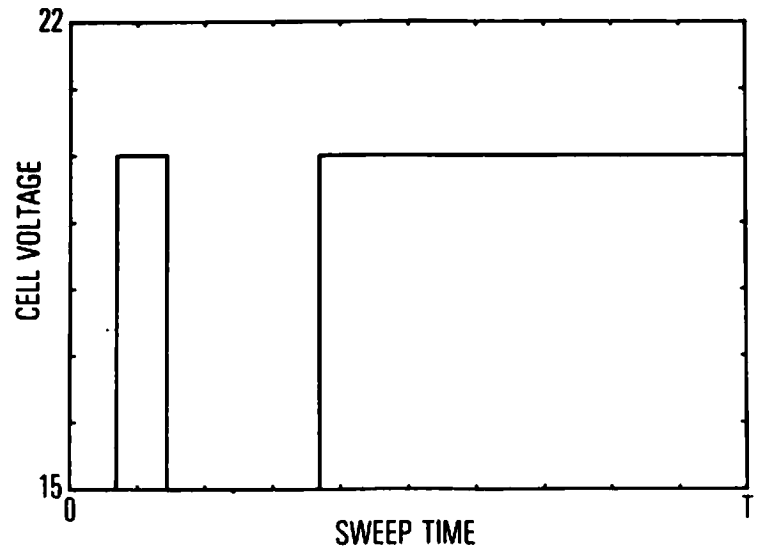

(b)

Figure 5-13 Temporal weighter control voltage for A/D operation
(a) Most significant bit plane
(b) Second most significant bit plane

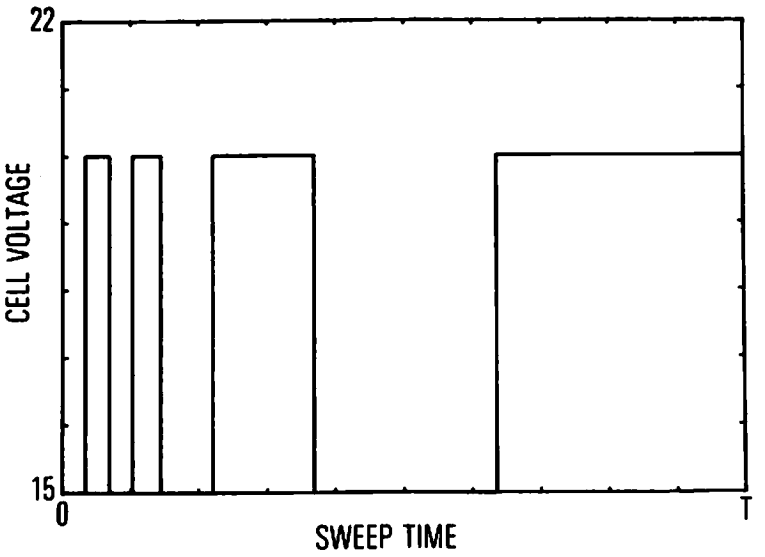

Figure 5-14 Temporal weighter control voltage for A/D operation least significant bit plane

Figure 5-15 Continuous tone input test image

Figure 5-16 Level slice operation on Fig. 5-15 with control voltage of Fig. 5-11b

Figure 5-17 Level slice operation on Fig. 5-15 with control voltage of Fig. 5-10b

Figure 5-18 Level slice operation on Fig. 5-15 with control voltage of Fig. 5-9b

operation could be demonstrated by translating the input image and observing the corresponding movement of the processed image on the camera monitor. The results obtained for stationary images using the vidicon system were nearly identical to those presented in this thesis using photographic film. This is clearly demonstrated in the photograph of the display monitor during a level slice operation shown in Fig. 5-19.

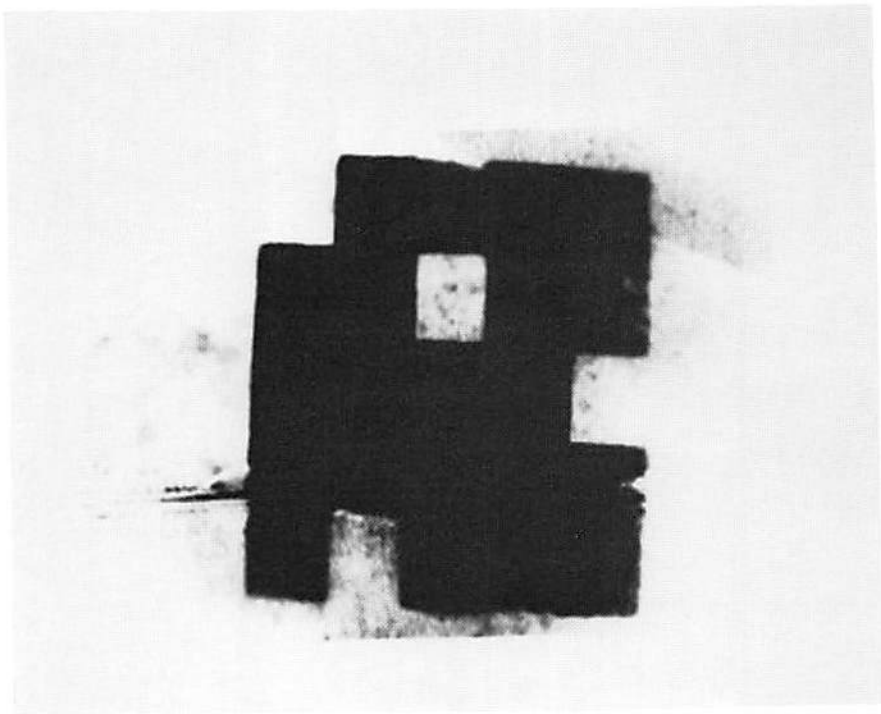

Figure 5-19 Photograph of display monitor during a level slice operation using a vidicon integrator

CHAPTER 6

THRESHOLD AND GAMMA IMPROVEMENT USING OPTICAL FEEDBACK

In Chapters 3 and 5, the resolution of the processing system was clearly related to the presence and effectiveness of the thresholding operation. While the light valve theory developed in Chapter 2 and applied to the processing system in Chapter 3 predicts sharp threshold characteristics for the light valves, the actual light valve transfer curves shown in Fig. 4-8 (for example) do not reflect this characteristic. In reality the devices begin to respond at voltage levels below the critical voltage and thus exhibit a relatively soft threshold characteristic. During this study, means of improving the threshold characteristics of the devices were investigated using optical feedback. This was motivated not only by the requirement for a sharp thresholding operation in the nonlinear processor, but also by the requirement for a threshold element in other processing schemes such as the halftone process briefly described in Chapter 1. In this process, not only is a sharp threshold required but also ideally an infinite gamma to achieve optimum results.

Typical liquid crystal light valves have an effective gamma of less than 2 clearly making them suboptimal for use in the halftone process.

To improve both the finite gamma and the soft threshold characteristics of the light valve, the feedback arrangement shown in Fig. 6-1 was used. As shown in the figure, a portion of the output light is directed back to the input of the light valve via a combination of beamsplitters and lenses. The light is summed with the input illumination at the surface of the light valve forming a positive feedback arrangement. Both the read and the write illumination were derived from an argon ion laser operating at 514.5 nm. It should be noted that although coherent light was used in the experimental procedure, the feedback arrangement and characteristics of the light valve are such that incoherent illumination would have worked as well. To avoid unwanted interference between the coherent input light and the feedback light, the input illumination was configured with its polarization orthogonal to the feedback component. In this manner, the incident light on the light valve was simply the sum of the intensities of the two components. In the initial state, with no input illumination and the feedback component set to zero by momentarily blocking the feedback path, the device remains in the off state resulting in zero output intensity. As the input illumination is increased, the device remains off

until the threshold level of the light valve is reached. At this point, the device begins to turn on and as a result of the optical gain characteristic of the light valve and the positive feedback, regeneration occurs. The device is switched on with no further increase in input illumination. The regenerative process continues until a point is reached on the light valve transfer curve where the loop gain (device gain less the feedback losses) drops to unity. In practice this point is reached before the saturation level of the light valve is reached. As a result, the desired binary transfer function is not entirely achieved but rather a soft shoulder is obtained with further increase in input illumination. Experimental results are shown in Fig. 6-2 together with the light valve transfer function for comparison. As seen in the figure, the feedback system provides a very sharp threshold characteristic as well as a marked improvement in overall gamma.

The light valve used to obtain the data in Fig. 6-2 did not exhibit a particularly high gamma. Thus the output range over which regeneration occurred was somewhat limited. Further, device nonuniformities over the aperture precluded the possibility of testing the feedback arrangement with two dimensional input images. To be effective, the device would have to be sufficiently uniform to maintain the input threshold point within a reasonably narrow band over the area of the input image. Improved

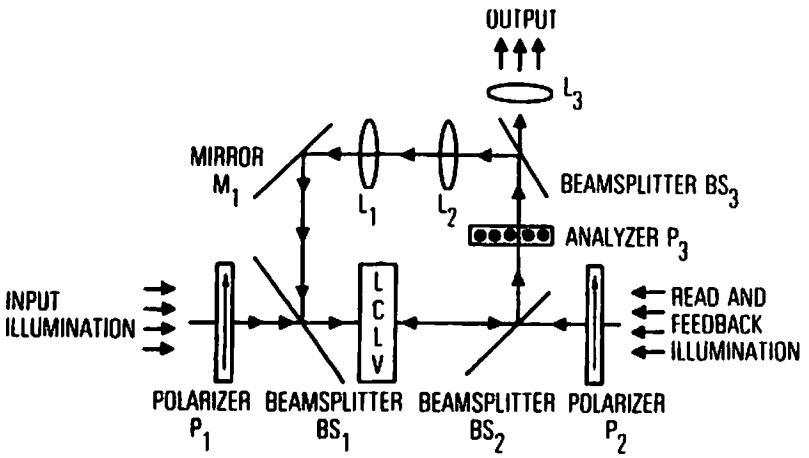

Figure 6-1 Experimental optical feedback system

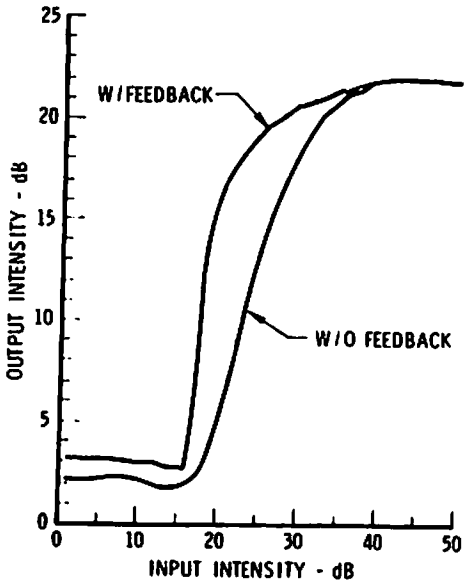

Figure 6-2 Feedback system response

devices exhibiting both the necessary uniformity and increased initial gamma could render the feedback system as a viable means of obtaining real time sharp thresholding operation from the light valves.

CHAPTER 7

CONCLUSIONS AND TOPICS FOR FUTURE RESEARCH

In this dissertation a method has been presented to achieve real time nonlinear optical image processing using liquid crystal light valves. A theory was developed to show how the polarization properties of the light valves could be controlled and used to implement the processing system. It was shown that not only could input images be processed in real time but also that the types of operations performed were varied and could in themselves be altered in real time.

While demonstrating the feasibility of the processing system, the results presented in Chapter 5 point out some obvious deficiencies in the experimental processing system. The lack of complete extinction of adjacent cells in Fig. 5-11 shows the limited intensity resolution of the experimental system. The effect is even further accentuated in the continuous tone level slices of Figs. 5-16 through 5-18. The primary source of degradation in the results is the light valves themselves. As mentioned in a previous chapter, the light valves were constructed primarily for test purposes unrelated to this

research. All of the light valves used in the experimental system exhibited nonuniformities across the aperture. The nonuniformities were apparent not only in the form of curvature of the substrates on which the various films were deposited but also as irregularities in the films themselves. Both types of nonuniformities led to degradation of device performance particularly in the processing of two dimensional images. The use of coherent laser light in the experimental system further accentuated the effect of the irregularities on performance. Diffraction effects from internal device defects as well as first surface reflections both contributed to degradation in performance.

High quality light valves with few irregularities have been produced for other applications [36]. The use of such devices in the nonlinear processing system would clearly improve performance and any future investigations of the system concepts presented in this paper should include the use of such devices. Further, extension of the dynamic range of the processing system could be achieved by tailoring the liquid crystal light valves to each specific processing function. For example in Fig. 3-4 it was noted that the presence of multiple nulls in the output response as a function of cell voltage restricted the system dynamic range. By producing a device with a cell thickness sufficiently thin to ensure only a single null, increased

dynamic range would result.

In Chapter 5 results were shown for the basic processes of level slice, logarithm, exponentiation, and A/D conversion. A logical extension of the results suitable for future research would be to cascade the operations to form a multiple function processor. For example homomorphic filtering could be implemented by combining the nonlinear processor capability with a standard coherent optical processing system. The scenario would be to use the signal or image corrupted by multiplicative noise as the input to the nonlinear processing system and perform a logarithmic transformation. The spatially separated noise term could then be removed by standard coherent processing techniques and the resultant logarithmically compressed image redirected back through the nonlinear processor. By configuring the processor to perform exponentiation during the second pass through the system, the original undegraded image could be retrieved at the output of the system.

In conclusion, the nonlinear processing system using multiple liquid crystal light valves has been shown to be a practicable method of producing real time nonlinear transformations on two dimensional input images. The experimental results are sufficiently encouraging to warrant further effort in refining the system and extending

the concept to include more complex multiprocessor applications.

REFERENCES

[1] K.T. Stalker and S.H. Lee, "Use of Nonlinear Optical Elements in Optical Information Processing," J. Opt. Soc. Am., Vol. 64, page 545,1974.

[2] S.H. Lee, "Optical Processing with Nonlinearity and Feedback," Proceedings Electro-Optics/International Laser Conference 1975, Anaheim, California, pp. 22-30, 1975.

[3] G. Hausler and A. Lohmann, "Hybrid Image Processing with Feedback," Optics Communications, Vol. 21, pp. 365-368, 1977.

[4] A. Lohmann, "Suggestions for Hybrid Image Processing," Optics Communications, Vol. 22, pp. 165-168, 1977.

[5] M. Marquet and J. Tsujiuchi, "Implementation of Particular Aspects of Dehalftoned Images," Optica Acta, Vol. 8, pp. 267-277, 1961.

[6] H. Kato and J.W. Goodman, "Nonlinear Filtering in Coherent Optical Systems Through Halftone Screen Processes," Applied Optics, Vol. 14, pp.1813-1824, 1975.

[7] S.R. Dashiell and A.A. Sawchuk, "Optical Synthesis of Nonlinear Nonmonotonic Functions," Optics Communications, Vol. 15, pp. 66-70, 1975.

[8] T.C. Strand, "Techniques and Applications of Nonlinear Processing with Halftones," Proc. SPIE, 20th Annual Technical Symposium, San Diego, California, August 1976.

[9] A. Armand, A.A. Sawchuk, and T.C. Strand, "Approaches to Nonlinear Optical Processing in Real Time," Proc. International Commission for Optics Congress, Madrid, Spain, September, 1978.

[10] C. Oseen, Transactions Faraday Society, Vol. 29, page 883, 1933.

[11] H. Zocher, Transactions Faraday Society, Vol. 29, page 945, 1933.

[12] F. Frank, Discussions Faraday Society, Vol. 25, pp. 19-28, 1958.

[13] P. Pincus, "Magnetic Properties of Liquid Crystals," Journal of Applied Physics, Vol. 41, No. 3, pp. 974-979, March 1970.

[14] R. Williams, "Liquid-Crystal Domains in a Longitudinal Electric Field," The Journal of Chemical Physics, Vol. 56, No. 1, pp. 147-148, January 1972.

[15] E. Jakeman and E.P. Raynes, "Electro-Optic Response Times in Liquid Crystals," Physics Letters, Vol. 39A, No. 1, pp. 69-70, April 1972.

[16] F. Brochard, P. Pieranski, and E. Guyon, "Dynamics of the Orientation of a Nematic-Liquid-Crystal Film in a Variable Magnetic Field," Physical Review Letters, Vol. 28, No. 26, pp. 1681-1683, June 1972.

[17] C.J. Gerritsma, W.H. DeJeu, and P. VanZanten, "Distortion of a Twisted Nematic Liquid Crystal by a Magnetic Field," Physics Letters, Vol. 36A, No. 5, pp. 389-390, September 1971.

[18] C.Z. Van Doorn, "On the Magnetic Threshold for the Alignment of a Twisted Nematic Crystal," Physics Letters, Vol. 42A, No. 7, pp. 537-539, January 1973.

[19] F.J. Kahn, "Electric Field Induced Orientational Deformation of Nematic Liquid Crystals: Tuneable Birefringence," Applied Physics Letters, Vol. 20, No. 5, pp. 199-201, March 1972.

[20] M. Schadt and W. Helfrich, "Voltage Dependent Optical Activity of a Twisted Nematic Liquid Crystal," Applied Physics Letters, Vol. 18, No. 4, pp.127-128, February 1971.

[21] R.A. Soref and M.J. Rafuse, "Electrically Controlled Birefringence of Thin Nematic Films," Journal of Applied Physics, Vol. 43, No. 5, pp. 2029-2037, May 1972.

[22] M.F. Schiekel and K. Fahrenschon, "Deformation of Nematic Liquid Crystals with Vertical Orientation in Electric Fields," Applied Physics Letters, Vol. 19, No. 10, pp. 391-393, November 1971.

[23] R.A. Kashnow and H.S. Cole, "Electric Effects in MBBA/PEBAB Mixtures," Molecular Crystals and Liquid Crystals, Vol. 23, pp. 329-342, 1973.

[24] D.W. Berreman, "Optics in Smoothly Varying Anisotropic Planar Structures: Application to Liquid-Crystal Twist Cells," Journal of the Optical Society of America, Vol. 63, No. 11, pp. 1374-1380, November 1973.

[25] D.W. Berreman, "Alignment of Liquid Crystals by Grooved Surfaces," Molecular Crystals and Liquid Crystals, Vol. 23, pp. 215-231, 1973.

[26] U. Wolff, W. Greubel, and H. Kruger, "The Homogeneous Alignment of Liquid Crystal Layers," Molecular Crystals and Liquid Crystals, Vol. 23, pp. 187-196, 1973.

[27] T.D. Beard, W.P. Bleha, and S.Y. Wong, "AC Liquid Crystal Light Valve," Applied Physics Letters, Vol. 22, No. 3, pp. 90-92, February 1973.

[28] J. Grinberg, et al., "A New Real-Time Non-Coherent to Coherent Light Image Converter," Optical Engineering, Vol. 14, No. 3, pp. 217-225, 1975.

[29] L.M. Fraas, et al., "Novel Charge-Storage-Diode Structure for use with Light Activated Displays," Journal of Applied Physics, Vol. 47, No. 2, pp. 576-583, February 1976.

[30] L.M. Fraas, et al., "AC Photoresponse of a Large Area Imaging CdS/CdTe Heterojunction," Journal of Applied Physics, Vol. 47, No. 2, pp. 584-590, February 1976.

[31] F. Leslie, "Distortion of Twisted Orientation Patterns in Liquid Crystals by Magnetic Fields," Molecular Crystals and Liquid Crystals, Vol. 12, pp. 57-72, 1970.

[32] J.W. Goodman, "Statistical Optics Notes," to be published by Wiley, New York.

[33] EM Laboratories, Inc., Elmsford, New York.

[34] S. Iwasa and J. Feinleib, "The PROM Device in Optical Processing Systems," Optical Engineering, Vol. 13, pp. 235-242, 1974.

[35] W.P. Bleha, et al., "Application of the Liquid Crystal Light Valve to Real-Time Optical Data Processing," Optical Engineering, Vol. 17, No. 4, pp. 371-384, 1978.

[36] A. Gara, "Real-Time Optical Correlation of 3-D Scenes," Applied Optics, Vol. 16, pp. 149-153, January 1977.